REDOX-ACTIVE LIGAND-INDUCED RADICAL REACTIVITY AT HIGH-VALENT OXORHENIUM AND OXOVANADIUM COMPLEXES

A Dissertation
Presented to
The Academic Faculty

by

Jennifer A. Hill-Lumm

In Partial Fulfillment
of the Requirements for the Degree
Doctor of Philosophy in the
School of Chemistry and Biochemistry

Georgia Institute of Technology
May, 2021

COPYRIGHT © 2021 BY JENNIFER A. HILL-LUMM

Redox-active ligand-induced radical reactivity at high-valent oxorhenium and oxovanadium complexes

Approved by:

Dr. Jake D. Soper, Advisor
School of Chemistry and Biochemistry
Georgia Institute of Technology

Dr. Angus P. Wilkinson
School of Chemistry and Biochemistry
Georgia Institute of Technology

Dr. Joseph P. Sadighi
School of Chemistry and Biochemistry
Georgia Institute of Technology

Dr. Krista S. Walton
School of Chemical and Biomolecular Engineering
Georgia Institute of Technology

Dr. Stefan France
School of Chemistry and Biochemistry
Georgia Institute of Technology

Date Approved: [March 31, 2021]

For my mom, Mary B. Pierson

ACKNOWLEDGEMENTS

First and foremost, I would like to thank Professor Jake D. Soper for his support and guidance over the past years. I have been able to grow as a chemist and person through working in his lab. Other members of the Soper lab including Dr. Caleb F. Harris and Mr. Chris Kuehner were especially helpful for discussions and brain-storming sessions. I would also very much like to thank my husband, Mr. William Lumm, who has over the years patiently listened (or at least pretended to listen) to hours of my ramblings about chemistry, and was supportive of a move away from friends and family in Arkansas so I could pursue this passion. Without his support I would not have made it this far. I would like to thank the rest of my family and friends for their continued support and encouragement, it made the tough times a little easier. I also need to thank the members of my committee for their help, support, and understanding during this process

I am grateful for the financial support provided by the Georgia Institute of Technology Chemistry GAANN Fellowship.

TABLE OF CONTENTS

ACKNOWLEDGEMENTS **iv**

LIST OF TABLES **viii**

LIST OF FIGURES **ix**

LIST OF SCHEMES **xii**

LIST OF SYMBOLS AND ABBREVIATIONS **xiii**

SUMMARY **xvi**

CHAPTER 1. Introduction **1**
1.1 Transition Metal-oxo Complexes for Small Molecule Oxidations **1**
  1.1.1 Importance of metal-oxos 1
  1.1.2 Oxidations catalyzed by metal-oxos 1
  1.1.3 Metal-oxo structure 3
1.2 Metal-oxo vs. Metal-oxyl Electronic Structures **5**
  1.2.1 Electronic structure of metal-oxyl 5
  1.2.2 Reported examples of oxyl radicals 7
  1.2.3 Previous work from the Soper Lab 9
1.3 Redox-active Ligands **11**
1.4 One- and two-electron oxidation reactivity **13**
1.5 Lignin Degradation **15**
  1.5.1 Valorization of lignocellulosic biomass 15
  1.5.2 Oxidative degradation of lignin 16
  1.5.3 Deoxydehydrogenation 17
1.6 Goals of Thesis Work **18**
1.7 References **19**

CHAPTER 2. Radical control in O-atom transfer from very high-valent oxorhenium complexes **24**
2.1 Note on collaboration **24**
2.2 Introduction **24**
2.3 Results **28**
  2.3.1 Oxidation of $[Re(O)_2(ap)_2]^-$ 28
  2.3.2 Structure of $[Re(O)_2(ap)(isq)]$ 29
  2.3.3 $[Re(O)_2(ap)(isq\bullet)]$ O-atom transfer 36
2.4 Discussion **50**
  2.4.1 Are $[Re(O)_2(ap)(isq\bullet)]$ and $[Re_2(\mu\text{-}O)(O)_2(ap)_2(isq\bullet)_2]$ oxyl radicals? 50
  2.4.2 C–O bond formation and Ph_3COH production 52
  2.4.3 Thermodynamic vs. kinetic effects on oxyl O-atom transfer 56
2.5 Conclusions **59**

2.6 Experimental details 60
  2.6.1 General considerations 60
  2.6.2 Methods and materials 62
  2.6.3 Synthesis of (Et$_4$N)[Re($^{16/18}$O)$_2$(ap)$_2$] 63
  2.6.4 Synthesis of [Re(O)$_2$(ap)(isq)] 63
  2.6.5 Synthesis of [Re$_2$(μ-O)(O)$_2$(ap)$_2$(isq•)$_2$] 64
  2.6.6 Reactions with triphenylmethyl radical 65
  2.6.7 Computational studies 65
2.7 X-ray crystallography 66
  2.7.1 [Re(O)(ap)(isq)] 66
  2.7.2 [Re$_2$(μ-O)(O)$_2$(ap)$_2$(isq)$_2$] 67
2.8 References 67

CHAPTER 3. Oxovanadium complexes for aerobic alcohol oxidation 70
3.1 Introduction 70
3.2 Results 72
  3.2.1 Synthesis 72
  3.2.2 Synthesis of [V(O)(OCO)OMe] 73
  3.2.3 Electrochemistry of [V(O)(OCO)X] complexes 77
  3.2.4 Preparation of [V$_2$(O)$_2$(OCO)$_2$(μ-O)] 78
  3.2.5 Synthesis of Alkoxide complexes 81
  3.2.6 Reactivity with alcohols 84
  3.2.7 Reactivity with O$_2$ 85
  3.2.8 Oxidation of [V(O)(OCO)Cl] 88
  3.2.9 Attempted OAT and HAT with [V(O)(OCO)Cl] 89
3.3 Discussion 89
  3.3.1 Solid state structures and electrochemistry 89
  3.3.2 Reactivity with alkoxides 90
  3.3.3 Reactivity with alcohols 93
  3.3.4 Reactivity with O$_2$ 95
3.4 Conclusion 96
3.5 Experimental 97
  3.5.1 General considerations 97
  3.5.2 Materials and methods 98
  3.5.3 Synthesis of [V(O)(OCO)OMe] 98
  3.5.4 Synthesis of [V$_2$O$_2$(OCO)$_2$(μ-O] 99
  3.5.5 General procedure for attempted alkoxide formation 99
3.6 X-ray Crystallography 99
  3.6.1 [V(O)(OCO)OMe] 99
  3.6.2 [V$_2$(O)$_2$(OCO)$_2$(μ-O)] 100
3.7 References 101

CHAPTER 4. Conclusions and future directions 103
4.1 Conclusions 103
4.2 Future directions 104

4.2.1 Continuing vanadium studies 104
4.2.2 MOFs for catalyst solid support 105
4.3 References 109

LIST OF TABLES

Table 2-1 Order determination for degradation of [Re(O)$_2$(ap)(isq•)] to [Re$_2$(μ-O)(O)$_2$(ap)$_2$(isq•)$_2$] in DCM 42

Table 3-1 Selected bond lengths comparing [V(O)(OCO)Cl] and [V(O)(OCO)OMe] 76

Table 3-2 Total $^{1\text{H}}$ signals of [V(O)(OCO)OMe] by integration against solvent over time 87

LIST OF FIGURES

Figure 1-2 d orbital splitting of metal-oxo with C4v symmetry 4

Figure 1-3 Square scheme for hydrogen atom transfer 5

Figure 1-4 Metal-oxo vs metal-oxyl 6

Figure 1-5 Options for creating metal-oxyl. Blue arrows indicate adding electrons to populate anti-bonding orbital. Red arrow indicates removing an electron from pi bonding orbital. 7

Figure 1-6 The use of redox-active catechol ligand to introduce a low-lying hole in ligand-centered orbitals 9

Figure 1-7 Reactivity of [Re(O)(ap)(isq)Cl] showing OAT to trityl radical but no OAT to triphenylphosphine 10

Figure 1-8 Formation of superoxo adduct of oxorhenium(V) complex with ligand oxidation 11

Figure 1-9 a) Possible oxidation states of amidophenolate ligand (ap) used in Chapter 2. b) Possible oxidation states of bis-phenoxide NHC ligand (OCO) used in Chapter 3. 13

Figure 1-10 Vanadium-salen from the Toste lab for C–O bond cleavage and bis(quinolinate)vanadium from Hanson and Baker for C–C bond cleavage 15

Figure 1-11 Alcohol monomers that constitute lignin 16

Figure 1-12 Model of the β–O–4 linkage in lignin a) C–O bond cleavage by bis(quinolinate)vanadium(V), b) C–C bond cleavage by vanadium-salen 17

Figure 1-13 Dehydration (top) and deoxydehydrogenation (bottom) of diol. 18

Figure 1-14 Oxidative-reductive couple of alcohol by dioxovanadium where R=aryl, vinyl, and R'=H, aryl, vinyl 18

Figure 2-1 Qualitative MO diagrams illustrating potential routes to metal–oxyl radicals in a tetragonal ligand field. (a) Open gray arrows show where the M–O bond order in a d^2 metal oxo is reduced from 3.0 to 2.5 by addition of 1e– to a M–O π^* orbital or removal 27

Figure 2-2 Cyclic voltammograms of $[Re(O)_2(ap)_2]^-$ (blue) and $[Re(O)_2(ap)(isq\bullet)]$ (green) in CH_2Cl_2 containing 0.1 M $[nBu_4N][PF_6]$, 10 mm Pt electrode, 100 mV s^{-1} scan rate, 25 °C. 29

Figure 2-3 Solid-state structure of $[Re(O)_2(ap)(isq\bullet)]$ shown with 50% probability ellipsoids. Hydrogen atoms omitted for clarity 31

Figure 2-4 Schematic of selected bond lengths (Å) for complexes (a) $[Re(O)_2(ap)_2]^-$ and its 1e– oxidation product (b) $[Re(O)_2(ap)(isq\bullet)]$. Red text are the computed metrical oxidation states (MOS) for each ligand. 31

Figure 2-5 Full ATR–FTIR spectra of (a) $[Re(O)_2(ap)_2]^-$ (blue) and $[Re(^{18O})(^{16O})(ap)_2]^-$ (red), (b) $[Re(O)_2(ap)_2]^-$ (blue) and $[Re(O)_2(ap)(isq\bullet)]$ (green) 34

Figure 2-6 ATR–FTIR spectra of (a) $[Re(O)_2(ap)_2]^-$ (blue) and $[Re(^{18O})(^{16O})(ap)_2]^-$ (red), with arrows indicating shifts of the ReO2 stretching bands upon labeling, and (b) $[Re(O)_2(ap)_2]^-$ (blue) and $[Re(O)_2(ap)(isq\bullet)]$ (green), with arrows indicating shifts the ReO2 35

Figure 2-8 (a) UV–vis absorption spectra of $[Re(O)_2(ap)(isq\bullet)]$ (green line) and $[Re2(\mu\text{-}O)(O)_2(ap)_2(isq\bullet)_2]$ (purple line) in C6H6. (b) THF solution of 9.3 × 10–5 M [Re(O)2(ap)(isq•)] t = 0 (green line) and t = 24 h (purple line) under N2 at 25 °C showing 12.8% con conversion to $[Re2(\mu\text{-}O)(O)_2(ap)_2(isq\bullet)_2]$. (c) C6H6 solution of 1.6 × 10–4 M $[Re(O)_2(ap)(isq\bullet)]$ at t = 0 (green line) and t = 14 d (purple line) under N2 at 25 °C showing 15.6% conversion to $[Re2(\mu\text{-}O)(O)_2(ap)_2(isq\bullet)_2]$. % conversion determined by iterative fits of the UV–vis data to linear combinations of the isolated spectra for $[Re(O)_2(ap)(isq\bullet)]$ and $[Re2(\mu\text{-}O)(O)_2(ap)_2(isq\bullet)_2]$. 38

Figure 2-9 (a) Solid-state structure of $[Re_2(\mu\text{-}O)(O)_2(ap)_2(isq\bullet)_2]$ shown with 50% probability ellipsoids. Hydrogen atoms omitted for clarity. A second, crystallographically unique dimer is not shown. (b) Schematic of selected bond lengths (Å) and computed MOS values (red) for each ligand in one dimer molecule. 40

Figure 2-11 Estimated Re–Ooxo bond strengths in (a) $[Re(O)_2(ap)_2]^-$ and (b) $[Re(O)_2(ap)(isq\bullet)]$ from thermodynamic oxo transfer reactivity with substrates containing known X/XO bond dissociation energies (DX/XO). 50

Figure 3-1 Structure of oxovanadium(V) complexes 71

Figure 3-2 Oxorhenium(V) and its vanadium analog 72

Figure 3-3 Synthesis of tris-homoleptic amidophenolate vanadium(V) 73

Figure 3-4 Synthesis of [V(O)(OCO)Cl] 73

Figure 3-5 ^{1}H NMR of a) [V(O)(OCO)Cl] in $CDCl_3$, b) [V(O)(OCO)Cl] in C_6D_6, c) [V(O)(OCO)OMe] in C_6D_6. * denotes NHC backbone resonances. 74

Figure 3-6 Crystal structure of [V(O)(OCO)OMe]. ORTEP ellipsoids at 50% probability with hydrogens omitted for clarity. 75

Figure 3-7 Cyclic voltammogram of [V(O)(OCO)Cl] (red) and [V(O)(OCO)OMe] (green) in MeCN solutions containing 0.1 M tetra-n-butylammonium hexfluorophosphate ($[nBu_4N][PF_6]$) using a platinum disk working electrode, platinum wire auxiliary electrode, and silver quasi-reference electrode with ferrocene as internal reference. 78

Figure 3-8 ^{1}H NMR, 300 MHz, C_6D_6 of a) dimer b) methoxide c) chloride 79

Figure 3-9 Crystal structure of $[V_2(O)_2(OCO)_2(\mu\text{-}O)]$, ORTEP ellipsoids at 50% probability, hydrogens and 4 benzene solvent molecules omitted for clarity. 80

Figure 3-10 ^{1}H NMR, 300MHz, C_6D_6, product from reaction of [V(O)(OCO)Cl] and NaOR. a) [V(O)(OCO)Cl], b) R=OMe, c) R=OiPr, d) R=OBn, e) R=OtBu 83

Figure 3-11 a) red trace: VO(OCO)Cl in MeCN purple to blue traces: increasing BnOH concentration, b) red trace: VO(OCO)Cl in benzene with BnOH 24 hr after exposure to air. Blue and purple traces: VO(OCO)Cl in benzene with BnOH 24 and 48 hr air-free. 85

Figure 3-12 ^{1}H NMR of [V(O)(OCO)OMe] a) initially under N_2, b) after introduction of O_2, c) after O_2 replaced with N_2, d) after reintroduction of O_2. 86

Figure 3-13 Proposed catalytic cycle for aerobic alcohol oxidation by [V(O)(OCO)Cl] 95

Figure 4-1 Post-synthetic exchange of catechol linker 107

Figure 4-2 Options for oxidation of $[Re^V(cat)]$ incorporated into MOF 108

LIST OF SCHEMES

Scheme 1-1 Epoxidation of alkene by vanadium oxo 2

Scheme 1-2 Arene oxidation by vanadium oxo 2

Scheme 2-1 Generation of $[Re2(\mu{-}O)_2(ap)_2(isq)_2]$ from reaction of $[Re(O)_2(ap)(isq\bullet)]$ with DHA 43

Scheme 2-2 Reaction stoichiometry for OAT from $[Re(O)_2(ap)(isq\bullet)]$ to PPh_3 or $Ph_3C\bullet$ 44

Scheme 2-3 Addition of Gomberg dimer to $[Re(O)(OCPh_3)(ap)(isq)]$ 54

Scheme 2-4 Electron transfer and radical couple mechanisms for reaction of $[Re(O)_2(ap)(isq\bullet)]$ and trityl 54

Scheme 3-1 Synthesis of [V(O)(OCO)OMe] from [V(O)(OCO)Cl]. 77

Scheme 3-2 Synthesis of [V(O)(OCO)OR] complexes 81

Scheme 3-3 Proposed route to dimer from reaction of [V(O)(OCO)Cl] with alkoxide salt 82

Scheme 3-5 Oxidation of [V(O)(OCO)Cl] by "magic green' 88

Scheme 3-6 Proposed steps for the reaction with alkoxides. Black V(V), red V(IV), blue V(III) 91

Scheme 3-7 Possible two-electron pathways for alcohol oxidation by [V(O)(OCO)Cl] 93

Scheme 3-8 Possible one-electron pathway for alcohol oxidation by [V(O)(OCO)Cl] 93

Scheme 3-8 Possible one-electron pathway for alcohol oxidation by [V(O)(OCO)Cl] 93

Scheme 4-4 Dimerization of $[Re^{V}O(ap)(isq)]$ 106

LIST OF SYMBOLS AND ABBREVIATIONS

~	About/Approximately
Å	Angstrom
α	Alpha
β	Beta
δ	Chemical Shift
ε	Molar absorptivity
˚	Degree(s)
˚C	Degree(s) Celsius
λ	Wavelength
ATR	Attenuated Total Reflection
approx.	Approximately
CFL	Compact Fluorescent Lamp
CH_2Cl_2	Dichloromethane
$CHCl_3$	Chloroform
CV	Cyclic Voltammogram
D	Deuterium
EPR	Electron Paramagnetic Resonance
ESI	Electrospray Ionization
FTIR	Fourier Transform Infrared
g	Grams
h	Hour(s)
HAT	Hydrogen atom transfer
HOMO	Highest Occupied Molecular Orbital

IR	Infrared
LMCT	Ligand-to-Metal Charge Transfer
LUMO	Lowest Unoccupied Molecular Orbital
MALDI-TOF	Matrix-assisted laser desorption/ionization – Time of flight
MeCN	Acetonitrile
MeOH	Methanol
mg	Milligram(s)
MHz	Megahertz
min	Minute(s)
mmol	Millimole
mol	Mole
mg	Milligram
nm	Nanometers
NMR	Nuclear Magnetic Resonance
OAT	Oxygen atom transfer
ORTEP	Oak Ridge Thermal Ellipsoid Plot
ppm	Parts Per Million
r.t.	Room Temperature
s	Second(s)
SOMO	Singly Occupied Molecular Orbital
THF	Tetrahydrofuran
TOF	Turnover frequency
TMS	Tetramethylsilane
TON	Turnover number
UV	Ultraviolent

vis	Visible
VT	Variable Temperature

SUMMARY

Metal-oxyl radicals might be the active species in many important oxygen-atom transfer and H-atom abstraction processes, ranging from industrial petroleum processing to biological detoxification, to energy conversion and storage in natural and synthetic water oxidation catalysis. However, their highly reactive nature makes them extremely challenging to both prepare and isolate. My PhD thesis research presents an entirely new strategy for preparing stabilized metal-oxyl radicals, which relies on ancillary redox-active ligands to impart radical character to terminal oxo groups. This approach was applied to two new classes of complexes. First, the synthesis and reactivity of a new d^0 oxorhenium complex, one oxidation level above Re(VII), $[Re^{VII}(O)_2(ap^{Ph})(isq^{Ph})]$ ($[ap^{Ph}]^{2-}$ = 2,4-di-tert-butyl-6-(phenylamido) phenolate, $[isq^{Ph}]^{\bullet 1-}$ = 2,4-di-tert-butyl-6-(phenylimino)semiquinonate), are described. This S=1/2 rhenium complex shows both closed- and open-shell O-atom transfer reactivity with small molecule substrates, including stable carbon radicals. Radical C–O coupling is indicative of the amidophenolate ligand imparting radical-like character to the oxo ligand. Mechanistic experiments were performed, and electronic structure-property relationships were developed to rationalize the observed reactivity. Extensions to new d0 oxovanadium complexes $V^VO(OCO)X$ (OCO=di-*tert*-butylphenolate N,N′-disubstituted imidazoline) complexes (X- = Cl-, OMe-, OBn-) led to the discovery of catalytic, aerobic alcohol oxidations that apparently result from intramolecular H-atom transfer to coordinated O^{2-} derived ligands, as well as other oxidation reactions relevant to lignin degradation. Divergent reactivity based on ligand oxidation state is shown to impart selectivity in oxidation of C–O, C–C, or C–H bonds in lignin model compounds.

CHAPTER 1. INTRODUCTION

1.1 Transition Metal-oxo Complexes for Small Molecule Oxidations

1.1.1 Importance of metal-oxos

Metal-oxo complexes have been extensively studied due to their importance in oxidation reactions. Their utility in selective oxidations dates back to the 19th century and more than 50 years ago the electronic structure of metal-oxos was elaborated on in the first issue of Inorganic Chemistry.[1] More than 30 years ago, Mayer and Nugent's seminal text on metal-oxygen multiple bonds included over 600 reported structures and spawned decades of renewed focus on the preparation and reactivity of oxometal complexes.[2-3] Over the past few decades there has been extensive focus on the role of transition metal-oxos in C–H oxidations,[4-5] synthetic water oxidation catalysis,[6-8] and varying biological systems including cytochrome P450s[9] and the oxygen evolving complex (OEC) of photosystem II.[10] In particular, C–H oxidations are an important part of converting hydrocarbon feedstock into more useful chemicals and this still remains a challenge.[4] Elucidating the role of metal-oxos in these and other reactions will allow for the development of more active and selective catalysts for transformations relevant to energy conversion and storage.

1.1.2 Oxidations catalyzed by metal-oxos

The following are some examples of oxidation reactions that are catalyzed by metal-oxos. These range from organic C–H activation to inorganic synthetic water oxidation and oxidations by biological systems. Scheme 1-1 and Scheme 1-2 represent the alkene epoxidation mechanism elucidated by Sharpless[11] and arene oxidation reported by Mimoun and co-workers.[12] Both are catalyzed by an oxovanadium complex.

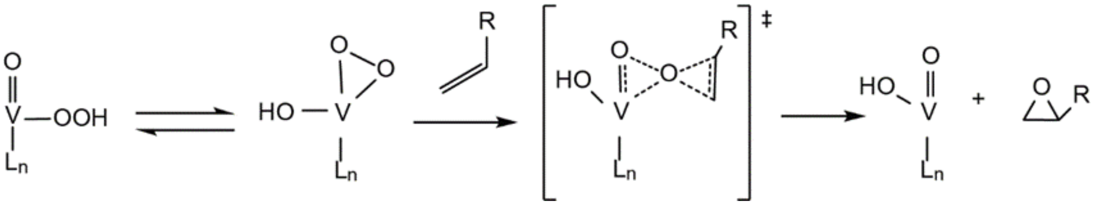

Scheme 1-1. Epoxidation of alkene by vanadium oxo

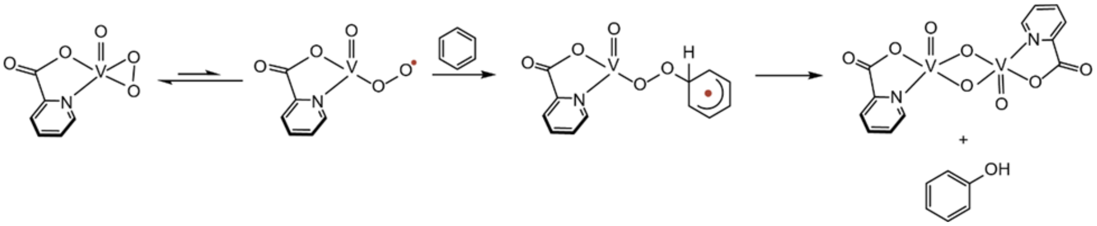

Scheme 1-2. Arene oxidation by vanadium oxo

Metal-oxos are also important features in biological systems. These include the iron(IV)oxo of Compound I in cytochrome P450, Figure 1-1 and the OEC of PSII. Figure 1-1 shows a couple steps of the catalytic cycle for cytochrome P450. Compound I is an Fe(IV) porphyrin and formation of it during the catalytic cycle is one of the places of divergence in the cycle. Either oxidation of the substrate (top path) occurs or there is oxidase uncoupling (bottom path) where the Fe(IV)=O is reduced to water completing the formal $4e^-$, $4H^+$ reduction of O_2 and forming 2 molecules of water.[13]

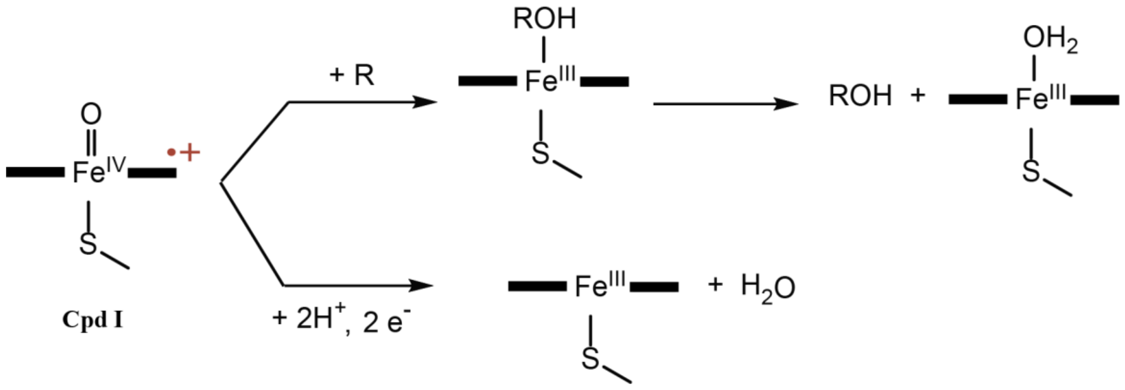

Figure 1-1. Divergent reactivity of Compound I of cyt P450

1.1.3 Metal-oxo structure

A wide range of metal-oxos exist in literature ranging from high-valent early 3d transition metal-oxos to 4d and 5d metal-oxos. Though the distribution of these complexes is not even across the transition metals. Oxo ligands are characterized by their capacity to form multiple bonds to metal centers. Gray and co-workers defined an "oxo-wall" between groups 8 and 9 of the periodic table for terminal oxos in tetragonal ligand fields.[14] To the left of the wall there is multiple bond character when there are five or less d electrons due to d-orbital splitting, Figure 1-2 is concerned only with the d orbital splitting of a metal-oxo. Adding more than two d electrons populates π^* (antibonding) orbitals and therefore reduces the bond order. Beyond four electrons this destabilizing effect becomes prohibitive. To the right of the oxo wall there cannot be multiple bond character to the metal-oxo bond due to the inaccessiblity of the high oxidation states required for the low d electron counts, unless the geometric constraints are relaxed by moving to three fold symmetry.

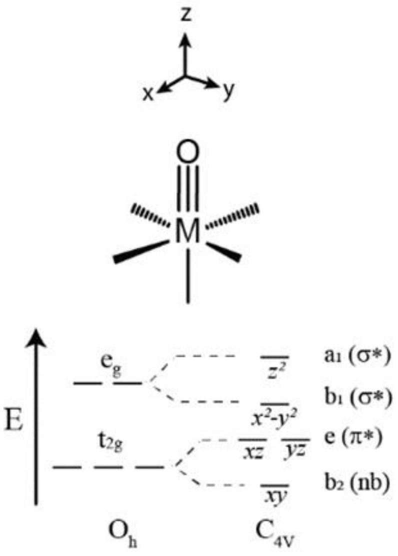

Figure 1-2. d orbital splitting of metal-oxo with C_{4v} symmetry

The reactivity of metal–oxo complexes is characterized by O-atom transfer. Thermodynamic oxo transfer reactivity scales popularized by Holm and co-workers rationalize the propensity of complexes to transfer an O-atom in a net 2e– redox process.[15-16]

In most cases, the net 2e– transfer of O to a substrate, such as PPh_3 or alkene, is proposed to occur without generation of odd electron intermediates. The cannonical hydroxyl rebound mechanism for C–H hydroxylation is a net O-atom trasnfer that occurs via a series of 1e– redox steps. The kinetic and thermodynamics of H• transfer to oxometal complexes has been extensively investigated by Mayer and co-workers.[17-18] It has been shown that radical character at the oxygen is not a prerequisite for HAT reactivity and reactivity is often well rationalized by thermodynamics, including the basicity and reduction potential of the oxo complex. Figure 1-3 shows a square scheme of HAT. The middle arrow denoting

HAT also represents the bond dissociation free-energy (BDFE) of the oxygen-hydrogen bond.

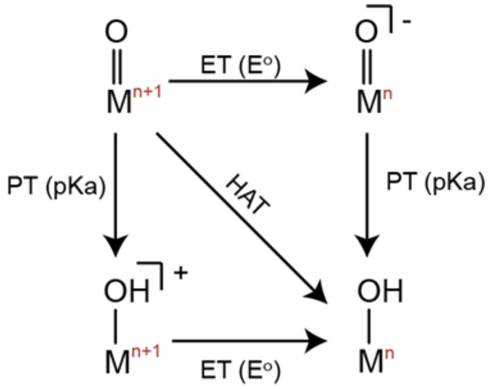

Figure 1-3. Square scheme for hydrogen atom transfer

However, there is evidence that the active species in some of these reactions is instead a metal-oxyl, a metal-oxo with radical character on the oxo ligand.[19-22] With these revelations suggesting inherently different reactivity not predicted by thermodynamics, focus has shifted to the study of metal-oxyls. This is complicated by the fleeting nature of these species due to their high rate of reactivity. This is explored more fully in Section 1.2.

1.2 Metal-oxo vs. Metal-oxyl Electronic Structures

1.2.1 Electronic structure of metal-oxyl

Metal-oxyls differ from metal-oxo complexes by only 1e–, but this has profound differences for the stability and reactivity of the M–O unit. By definition, an oxyl contains unpaired spin on the oxygen as shown in Figure 1-4. And as noted above, unpaired spin is not a necessity for radical-type reactions to occur at the oxo, but it is argued later in Chapter 2 of this work that this difference imparts some kinetic advantage to the reactivity.

Therefore, it is important to understand more about the structure and reactivity of metal-oxyls.

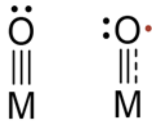

Figure 1-4. Metal-oxo vs metal-oxyl

Molecular orbital (MO) theory provides a starting place for understanding metal-oxyls. Figure 1-2 is an expanded orbital splitting diagram from the one previously described and defines metal-oxo in a tetragonal field from the Ballhausen and Gray model.[1] One can envision a radical can occur one of two ways, the first is by reduction of a d^2 metal to d^3 (blue arrows), thus populating a π^* antibonding orbital and reducing the bond order by half. The second is by removing an electron from the e symmetry π bonding orbital (red arrow). Both pathways are challenging synthetically. The first option has two problems. The first is that by adding an electron to the π^* orbital you create a strong reducing complex, not oxidizing. The second is that the π^* orbitals are mainly metal-centered, meaning the radical would be more localized there than on the oxo. The second option, removing an electron from the oxo ligand centered π bonding orbital, is complicated by being able to selectively remove an electron from a low-lying orbital.

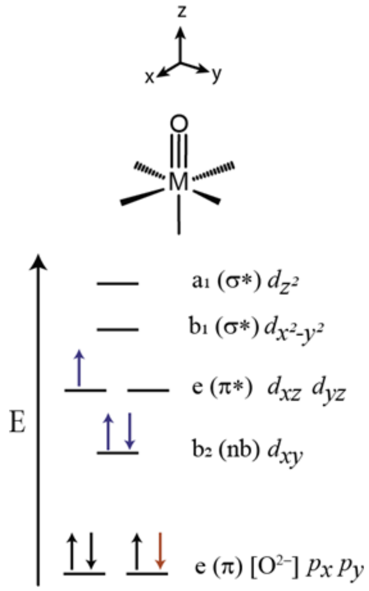

Figure 1-5. Options for creating metal-oxyl. Blue arrows indicate adding electrons to populate anti-bonding orbital. Red arrow indicates removing an electron from pi bonding orbital.

1.2.2 Reported examples of oxyl radicals

Due to the reactive nature of metal-oxyls there are very few examples in literature. In fact, there are only three published oxyls that are fully characterized, two ruthenium-oxyls and a zinc-oxyl. The first from Kobayashi and co-workers in 2003 was a ruthenium-oxyl supported by quinone ligands that was shown to be a competent catalyst for water oxidation.[23] This work was followed up on by Muckerman and co-workers.[24] A second ruthenium-oxyl bearing an NHC trans to the oxyl was described by Shimoyama and co-workers in 2016 and showed catalytic C-H oxidation.[25] The trans-effect of the NHC weakens the metal-oxo bond and is credited by the authors of helping to form the oxyl. Interestingly, similar ruthenium(IV)-oxos with polypyridyl ligands are unable to oxidize benzaldehyde while the one with the NHC ligand has no trouble with such oxidations. In

2017, Oda and co-workers reported a stable zinc-oxyl supported in a zeolite and later showed it was able to activate CH_4 at room temperature.[26-27]

While there are very few examples of fully characterized metal-oxyls, there are more examples of partially characterized oxyls in the literature. These cover a number of different metals including titanium, nickel, copper, and ruthenium.[28] By far the greatest number of proposed metal-oxyls in the literature are those that are based on DFT calculations and have little supporting experimental evidence.

More recently, in 2016 Herlihy and co-workers reported a titanium-oxyl during photocatalytic water oxidation.[29] They used *in situ* ultrafast infrared spectroscopy to detect the titanium-oxyl on the surface of an n-$SrTiO_3$/aqueous interface and show that it is stable on nanosecond timescales.

The last example is a rhenium-oxyl proposed by Lippert and co-workers in the Soper Lab.[30-31] It was proposed that symmetry-allowed mixing of molecular orbitals from redox-active ligands allow for oxyl-like character in the formally closed-shell Re(VI) oxo. The work in this thesis builds upon the ideas from Lippert and co-workers and is explored in more detail below.

1.2.3 Previous work from the Soper Lab

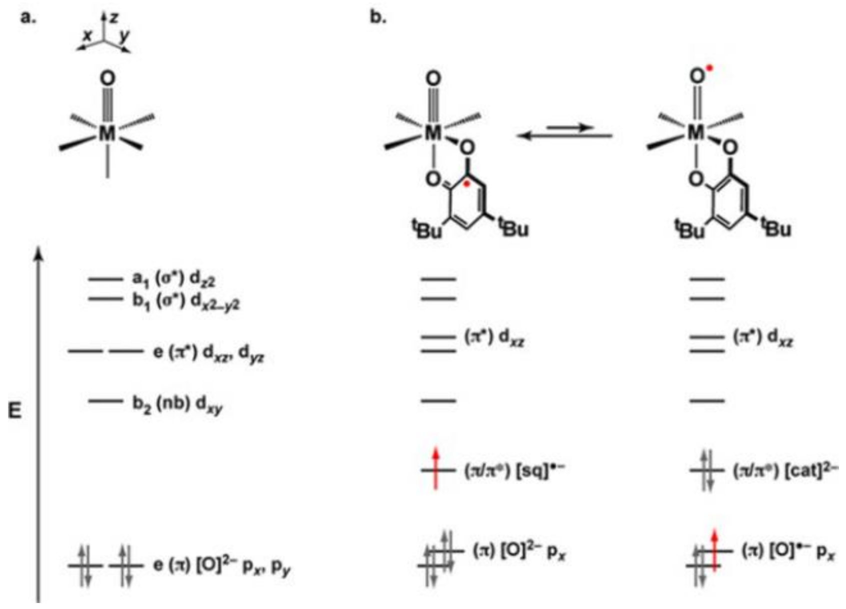
a.
z
x
y
O
M
E
a1 (σ*) dz2
b1 (σ*) dx2–y2
e (π*) dxz, dyz
b2 (nb) dxy
e (π) [O]2– px, py
b.
O
M
O
O
tBu
tBu
(π*) dxz
(π/π*) [sq]•–
(π) [O]2– px
O•
M
O
O
tBu
tBu
(π*) dxz
(π/π*) [cat]2–
(π) [O]•– px

Figure 1-6. The use of redox-active catechol ligand to introduce a low-lying hole in ligand-centered orbitals

Lippert and co-workers proposed that by introducing a redox-active ligand scaffold, as shown in part b of Figure 1-6, symmetry allowed mixing of the orbitals can delocalize the hole created by ligand oxidation into the metal-oxo π bond thus reducing the bond order by 0.5. This would then have the benefit of overcoming the problem of removing an electron from a low-lying orbital.

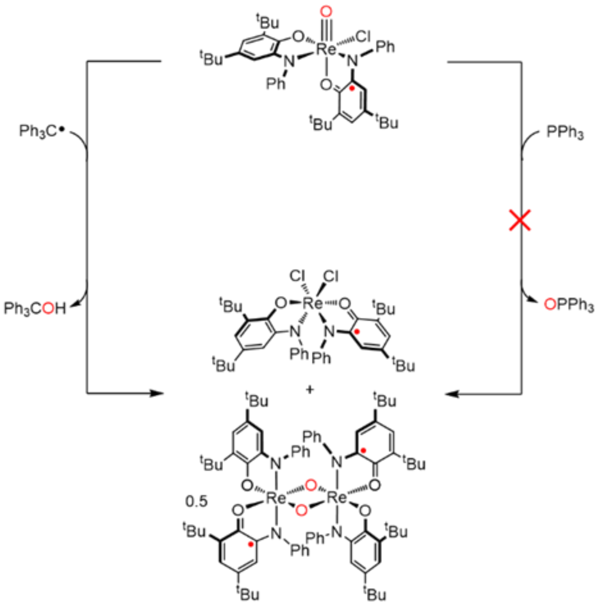

Figure 1-7. Reactivity of [Re(O)(ap)(isq)Cl] showing OAT to trityl radical but no OAT to triphenylphosphine

Figure 1-7 shows the use of redox-active aminophenol derived ligand to impart radical reactivity at the rhenium oxo bond. This complex exhibited reactivity atypical of most oxorhenium complexes, as it would transfer an oxygen atom to trityl, a stable carbon radical but did not show any OAT reactivity towards traditional, closed-shell acceptors like triphenylphosphine. It should be noted, however, that this Re(VI) complex is not truly an S=1/2 complex. The ligand centered radical couples antiferromagnetically with the lone electron of the rhenium creating an S=0, diamagnetic, complex.

Lippert also demonstrated that redox-active ligands can facilitate bimetallic homolysis of molecular oxygen at an oxorhenium(V) complex bearing two catechol ligands.[31] Ligand oxidation allows for the formation of a superoxo adduct, Figure 1-8. As redox-active ligands play an important role in the work that follows, a discussion of this unique class of ligands is described below.

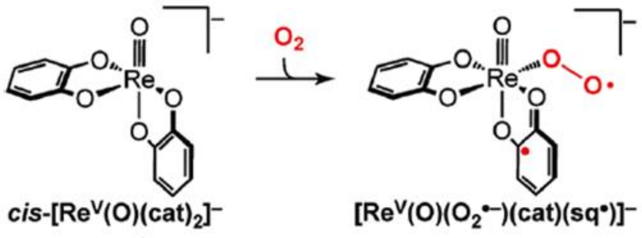

Figure 1-8. Formation of superoxo adduct of oxorhenium(V) complex with ligand oxidation

1.3 Redox-active Ligands

We proposed that ligand oxidation introduces a “hole” in lower-lying orbitals that can be delocalized to metal-oxo by spin-allowed orbital mixing. Most ligands are redox inert with oxidations or reductions of classic Werner complexes occuring at the metal center. But the preparation and electronic properties of a subclass of so-called redox-active ligands has been the subject of ongoing study for over 50 years.

A discussion of this unique class of ligands is required. Redox-active ligands are a type of chelating ligand capable of binding to a metal center in more than one discrete oxidation state. They are sometimes referred to as non-innocent as they can make formal determination of the metal oxidation state ambiguous. They can be oxidized or reduced at modest potentials and therefore can act as electron reservoirs and contribute one or two electrons to the metal.

Historically metals such as platinum, palladium, rhodium, and iridium were used for selective bond-breaking and bond-making reactions. These metals prefer to be in oxidation states of ±2, and this facilitates the 2e– redox process. As these metals are scarce and therefore expensive, a move to the more earth-abundant first row transition metals is needed for better sustainability. The challenge with using base metals like iron and cobalt is their propensity for 1e– chemistry. The use of redox-active ligands can allow these metals to catalyze reactions previously reserved only for precious metals.[32]

Examples of the successful use of a redox-active ligand include an iron pyridinebisimine out of the Brookhart lab for oligomerization of ethylene into linear α-olefins that is both highly selective and efficient.[33] Gibson and coworkers reported both iron and cobalt catalysts supported by 2,6-bis(imino)pyridyl ligands for similar olefin polymerization, where the iron catalysts performed even better than metallocenes under similar conditions.[34] More recently, Heyduk has reported a tantalum complex supported by an N,N-bis(phenoxide) amine that does four electron oxidative formation of aryl diazenes, a reaction that is unique for early transition metal imidos. This reactivity has relevance not only for N–N bond formation but other multi-electron processes like O–O bond formation.[35-36]

The ligands used in this work, and their possible oxidation states are shown in Figure 1-9. The amido phenolate ligand has been widely used by Weighardt and co-workers on a number of metals to study the determination of metal oxidation states when coordinated to redox-active ligands.[37-38]

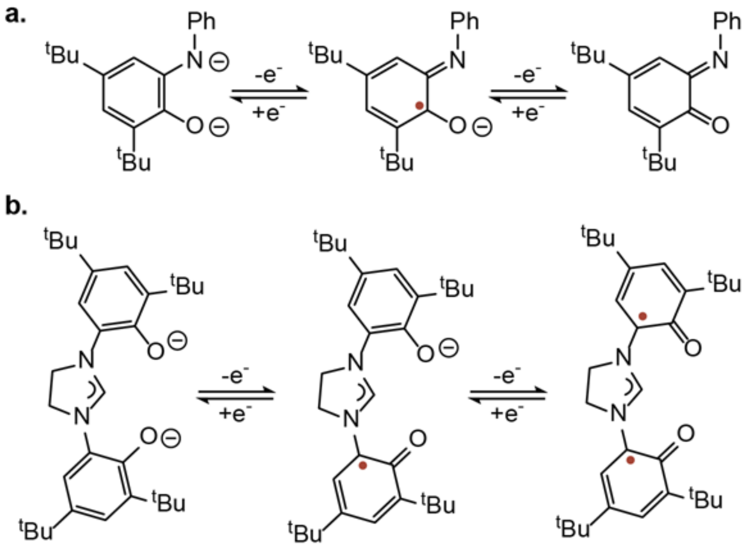

Figure 1-9. a) Possible oxidation states of amidophenolate ligand (ap) used in Chapter 2. b) Possible oxidation states of bis-phenoxide NHC ligand (OCO) used in Chapter 3.

These ligands have been shown to support high-valent oxometal complexes. The first report of the NHC, N,N′-bis(2-hydroxy-3,5-di-tert-butylphenyl)-4,5-dihydroimidazolinium chloride, OCO, ligand was an oxovanadium(V)[39] and the electrochemistry of this ligand, along with derivatives, was studied on cobalt.[40]

1.4 One- and two-electron oxidation reactivity

Aside from a difference in the reactivity of metal-oxos versus metal-oxyls discussed earlier, one- versus two-electron reactivity for the oxidative cleavage of C–O and C–C bonds is important. There is much debate in the oxovanadium literature as to the mechanism of alcohol oxidation, a one- or two- electron pathway, for these complexes. Unsurprisingly, these two possibilities give different products and therefore reactions can be tuned according to the need.

The first example is a cobalt-salen that oxidatively cleaves C–C bonds in phenolic compounds. This is thought to occur through a superoxo intermediate that abstracts an H-atom and creates an oxygen-centered radical.[41-42]

A copper(I) chloride/TEMPO/2,6-lutidine system was shown to directly cleave the C–C bond cleavage of the simple model lignin compound 1,2-diphenyl-2-methoxyethanol.[43] The exact mechanism of oxidations mediated by copper is still contested. The products of the oxidation by the CuCl/TEMPO system suggest an electron transfer pathway.[44] But work from the Stahl lab with a similar system suggested initial alcohol oxidation followed by a retro-aldol reaction.[45]

Son and Toste proposed a one electron mechanism for the non-oxidative cleavage of the C–O bond of the β–O–4 linkage in lignin (described further in Section 1.5.2) by an oxovanadium(V) complex. Their cycle starts with hydrogen atom abstraction by the terminal oxo and then proceeds through homolytic cleavage of the C–O bond.[46]

Work from Hanson and Baker showed an interesting base-dependence for aerobic alcohol oxidation by a dipicolinate vanadium(V) complex (discussed in Chapter 3).[47] The requirement of a base suggests a two-electron pathway. They also showed a vanadium(V) bis(quinolinate) was active for C–C bond cleavage of model lignin compounds, showing divergent reactivity with the vanadium catalyst developed by Toste.[48] These two vanadium catalysts are shown in Figure 1-10.

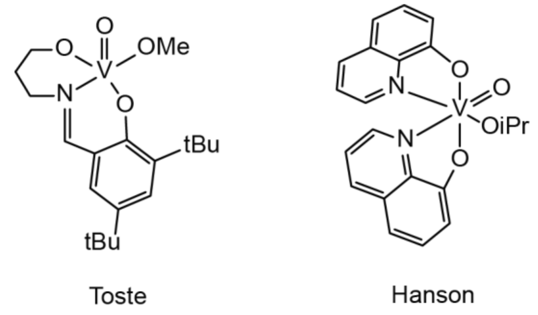

Toste Hanson

Figure 1-10. Vanadium-salen from the Toste lab for C–O bond cleave and bis(quinolinate) from Hanson and Baker for C–C bond cleavage

Overall, one- and two-electron pathways for oxidation are possible with a number of different first-row transition metals. Specifically, one- versus two- electron pathways for bond cleavage in lignin models change the product distribution, with ketone products produced by a 2e– pathway. As this reactivity has specific relevance for the degradation of lignin biomass into useful fuels and chemicals a discussion of that follows.

1.5 Lignin Degradation

1.5.1 Valorization of lignocellulosic biomass

According to a 2020 report by Global Market Insights, Inc., the global lignin market will exceed one billion USD by 2026.[49] This is due to a number of factors including a move away from fossil fuel based chemical feedstocks and towards more renewable sources. Lignocellulosic biomass represents a great source of more environmentally friendly raw materials. Lignocellulose is made up of three different polymers. Cellulose is composed of a linear polymer of glucose while hemicellulose is an amorphous polymer of xylose and other sugars. It is the third component, lignin, that this report will focus most on. On the whole, lignin makes up 15-30% by mass of lignocellulosic biomass but 40% by energy.[50]

Unfortunately, lignin is a more complex and irregular polymer than either cellulose or hemicellulose and this complicates efforts to transform it into other useful chemicals. It is made of different phenolic linkages with varying methoxy substitution. The wide range of bonds, C–H, C–O, alkyl C–C and aryl C–C, in this polymer makes utilizing this relatively abundant carbon feedstock difficult. There are three basic monomers in lignin, coniferyl alcohol, p-coumaryl alcohol, and sinapyl alcohol, as shown in Figure 1-11.

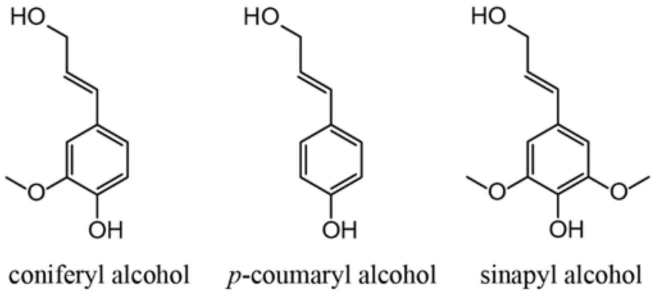

Figure 1-11. Alcohol monomers that constitute lignin

There are varying chemical process that have been employed for lignin degradation. These include, but are not limited to: cracking, hydrolysis, oxidation, and reduction. The focus of this work is on oxidative degradation processes.

1.5.2 Oxidative degradation of lignin

One of the most important aspects for the degradation of lignin is selective bond breaking. Lignin represents an excellent source of aryl containing building blocks like phenol, benzene, and xylene. This requires the breaking of specific bonds in the linkages of lignin. The linkage that has received the most attention is the β–O–4 linkage since those constitute roughly 50% of the linkages in lignin.[51] Figure 1-12Figure 1-12 demonstrates the difference in reactivities for the two different vanadium oxo complexes discussed above.

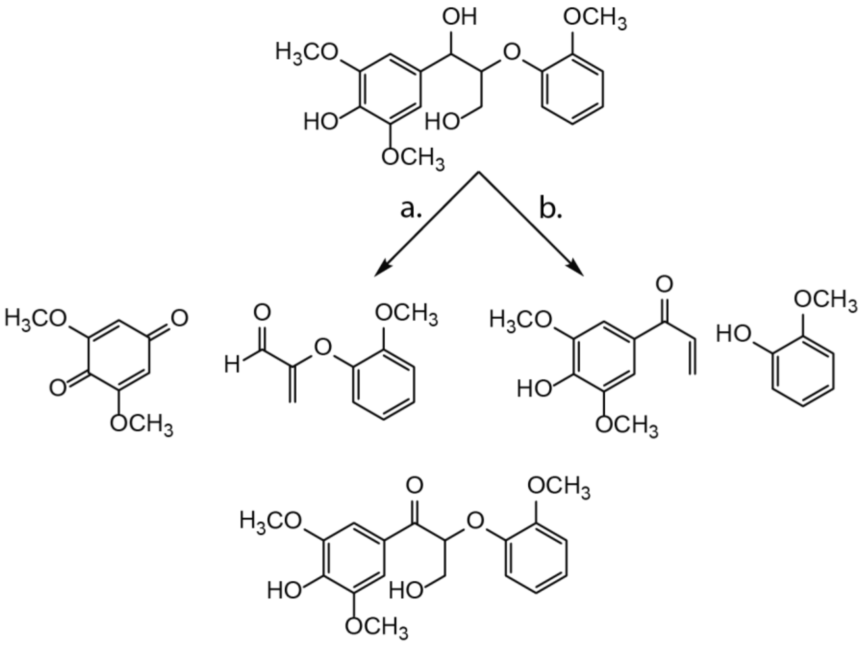

Figure 1-12. Model of the β–O–4 linkage in lignin. a) C–O bond cleavage by bis(quinolinate) vanadium(V) , b) C–C bond cleavage by vanadium-salen

1.5.3 Deoxydehydrogenation

As recently as 2019, a vanadium oxo complex has shown oxidative-reductive coupling of alcohols similar to previously reported active catalysts for the deoxydehydration (DODH) reaction.[52] These reactions are particularly useful for lignin degradation as they provide a way to deoxygenate the oxygen-rich lignin polymer. Formally, DODH removes the two -OH from diols to form olefins. DODH reactions differ from dehydration reactions by complete removal of both -OH groups instead of leaving one oxidized.[53] This is shown in Figure 1-13. By far, rhenium has been most studied for DODH reactions, particularly methyltrioxorhenium for the DODH of diols. Other metals are also used with molybdenum and tungsten being the most common after rhenium.[54-55]

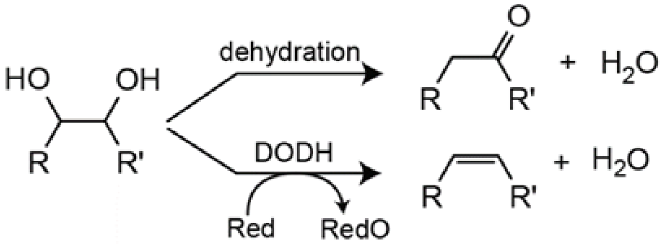

Figure 1-13. Dehydration (top) and deoxydehydrogenation (bottom) of diol.

As previously noted, vanadium has seen renewed interest for this type of reactivity. Specifically, Steffensmeier and coworkers showed that a vanadium oxo bearing salen-type ligands is active for what they term oxidative-reductive coupling. They saw both the product of alcohol oxidation, the ketone or aldehyde, as well as a reduced alkane, Figure 1-14.[52]

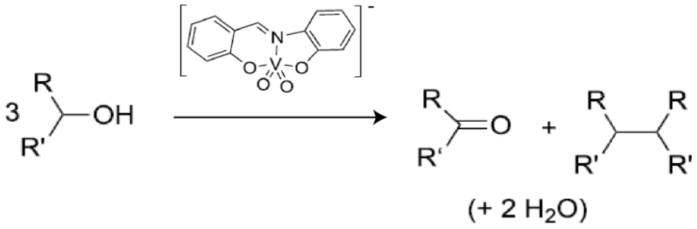

Figure 1-14. Oxidative-reductive coupling of alcohol by dioxovanadium. Adapted from ref[52] where R= aryl, vinyl and R'=H, aryl, vinyl.

1.6 Goals of Thesis Work

This thesis will describe the use of redox-active ligands to impart radical character on a metal-oxo thereby allowing for the characterization and study of oxyl-like reactivity. It will demonstrate that high-valent metal-oxos are capable of C–H and C–O bond making and breaking reactivity relevant to small molecule oxidation and transformation of renewable chemical feedstocks into commodity chemicals.

Specifically, this thesis aims to answers the following questions:

1. Do redox-active amidophenolate ligands facilitate the synthesis and characterization of an S=1/2 high-valent oxorhenium complex?

2. Does an S=1/2 oxorhenium complex react differently towards O-atom acceptors than its closed-shell counterparts?

3. Is divergent reactivity due to ancillary ligand radicals imparting radical character on an adjacent terminal metal-oxo?

4. Can redox-active ligands impart a bias for 1- or 2- electron chemistry?

1.7 References

1. Ballhausen, C. J.; Gray, H. B., The Electronic Structure of the Vanadyl Ion. *Inorganic Chemistry* **1962,** *1* (1), 111-122.

2. Nugent, W. A.; Mayer, J. M., *Metal-Ligand Multiple Bonds: The Chemistry of Transition Metal Complexes Containing Oxo, Nitrido, Imido, Alkylidene, Or Alkylidyne Ligands*. Wiley, 1988.

3. Mayer, J. M., Metal-oxygen multiple bond lengths: a statistical study. *Inorganic Chemistry* **1988,** *27* (22), 3899-3903.

4. Gunay, A.; Theopold, K. H., C−H Bond Activations by Metal Oxo Compounds. *Chemical Reviews* **2010,** *110* (2), 1060-1081.

5. Borovik, A. S., Role of metal–oxo complexes in the cleavage of C–H bonds. *Chem. Soc. Rev.* **2011,** *40* (4), 1870.

6. Binstead, R. A.; Chronister, C. W.; Ni, J.; Hartshorn, C. M.; Meyer, T. J., Mechanism of Water Oxidation by the μ-Oxo Dimer $[(bpy)_2(H_2O)Ru^{III}ORu^{III}(OH_2)(bpy)_2]^{4+}$. *Journal of the American Chemical Society* **2000,** *122* (35), 8464-8473.

7. Liu, F.; Concepcion, J. J.; Jurss, J. W.; Cardolaccia, T.; Templeton, J. L.; Meyer, T. J., Mechanisms of Water Oxidation from the Blue Dimer to Photosystem II. 26.

8. Surendranath, Y.; Kanan, M. W.; Nocera, D. G., Mechanistic Studies of the Oxygen Evolution Reaction by a Cobalt-Phosphate Catalyst at Neutral pH. *Journal of the American Chemical Society* **2010,** *132* (46), 16501-16509.

9. Rittle, J.; Younker, J. M.; Green, M. T., Cytochrome P450: The Active Oxidant and Its Spectrum. *Inorganic Chemistry* **2010,** *49* (8), 3610-3617.

10. Cady, C.; Crabtree, R.; Brudvig, G., Functional models for the oxygen-evolving complex of photosystem II. *Coordination Chemistry Reviews* **2008,** *252* (3-4), 444-455.

11. Chong, A. O.; Sharpless, K. B., Mechanism of the molybdenum and vanadium catalyzed epoxidation of olefins by alkyl hydroperoxides. *The Journal of Organic Chemistry* **1977,** *42* (9), 1587-1590.

12. Mimoun, H.; Saussine, L.; Daire, E.; Postel, M.; Fischer, J.; Weiss, R., Vanadium(V) peroxy complexes. New versatile biomimetic reagents for epoxidation of olefins and hydroxylation of alkanes and aromatic hydrocarbons. *Journal of the American Chemical Society* **1983,** *105* (10), 3101-3110.

13. Denisov, I. G.; Makris, T. M.; Sligar, S. G.; Schlichting, I., Structure and Chemistry of Cytochrome P450. *Chemical Reviews* **2005,** *105* (6), 2253-2278.

14. Winkler, J. R.; Gray, H. B., Electronic Structures of Oxo-Metal Ions. In *Molecular Electronic Structures of Transition Metal Complexes I*, Mingos, D. M. P.; Day, P.; Dahl, J. P., Eds. Springer Berlin Heidelberg: Berlin, Heidelberg, 2012; pp 17-28.

15. Lee, S. C.; Holm, R. H., Toward an expanded oxygen atom transfer reactivity scale: Computational investigation of the energetics of oxo transfer reaction couples. *Inorganica Chimica Acta* **2008,** *361* (4), 1166-1176.

16. Holm, R. H.; Donahue, J. P., A thermodynamic scale for oxygen atom transfer reactions. *Polyhedron* **1993,** *12* (6), 571-589.

17. Mayer, J. M., Understanding Hydrogen Atom Transfer: From Bond Strengths to Marcus Theory. *Accounts of Chemical Research* **2011,** *44* (1), 36-46.

18. Mayer, J. M., Hydrogen Atom Abstraction by Metal−Oxo Complexes: Understanding the Analogy with Organic Radical Reactions. *Accounts of Chemical Research* **1998,** *31* (8), 441-450.

19. Betley, T. A.; Wu, Q.; Van Voorhis, T.; Nocera, D. G., Electronic Design Criteria for O−O Bond Formation via Metal−Oxo Complexes. *Inorganic Chemistry* **2008,** *47* (6), 1849-1861.

20. Siegbahn, P. E. M.; Crabtree, R. H., Manganese Oxyl Radical Intermediates and O−O Bond Formation in Photosynthetic Oxygen Evolution and a Proposed Role for the Calcium Cofactor in Photosystem II. *Journal of the American Chemical Society* **1999,** *121* (1), 117-127.

21. Yang, X.; Baik, M.-H., cis,cis-[(bpy)2RuVO]2O4+ Catalyzes Water Oxidation Formally via in Situ Generation of Radicaloid RuIV−O•. *Journal of the American Chemical Society* **2006,** *128* (23), 7476-7485.

22. Lundberg, M.; Blomberg, M. R. A.; Siegbahn, P. E. M., Oxyl Radical Required for O−O Bond Formation in Synthetic Mn-Catalyst. *Inorganic Chemistry* **2004,** *43* (1), 264-274.

23. Kobayashi, K.; Ohtsu, H.; Wada, T.; Kato, T.; Tanaka, K., Characterization of a Stable Ruthenium Complex with an Oxyl Radical. *Journal of the American Chemical Society* **2003,** *125* (22), 6729-6739.

24. Muckerman, J. T.; Polyansky, D. E.; Wada, T.; Tanaka, K.; Fujita, E., Water Oxidation by a Ruthenium Complex with Noninnocent Quinone Ligands: Possible Formation of an O−O Bond at a Low Oxidation State of the Metal. *Inorganic Chemistry* **2008,** *47* (6), 1787-1802.

25. Shimoyama, Y.; Ishizuka, T.; Kotani, H.; Shiota, Y.; Yoshizawa, K.; Mieda, K.; Ogura, T.; Okajima, T.; Nozawa, S.; Kojima, T., A Ruthenium(III)-Oxyl Complex Bearing Strong Radical Character. *Angew. Chem.* **2016,** *128* (45), 14247-14251.

26. Oda, A.; Ohkubo, T.; Yumura, T.; Kobayashi, H.; Kuroda, Y., Identification of a Stable ZnII–Oxyl Species Produced in an MFI Zeolite and Its Reversible Reactivity with O2 at Room Temperature. *Angewandte Chemie International Edition* **2017,** *56* (33), 9715-9718.

27. Oda, A.; Ohkubo, T.; Yumura, T.; Kobayashi, H.; Kuroda, Y., Room-Temperature Activation of the C–H Bond in Methane over Terminal Zn <sup>II</sup> –Oxyl Species in an MFI Zeolite: A Combined Spectroscopic and Computational Study of the Reactive Frontier Molecular Orbitals and Their Origins. *Inorganic Chemistry* **2019,** *58* (1), 327-338.

28. Shimoyama, Y.; Kojima, T., Metal–Oxyl Species and Their Possible Roles in Chemical Oxidations. *Inorganic Chemistry* **2019,** *58* (15), 9517-9542.

29. Herlihy, D. M.; Waegele, M. M.; Chen, X.; Pemmaraju, C. D.; Prendergast, D.; Cuk, T., Detecting the oxyl radical of photocatalytic water oxidation at an n-SrTiO3/aqueous interface through its subsurface vibration. *Nat Chem* **2016,** *8* (6), 549-555.

30. Lippert, C. A.; Arnstein, S. A.; Sherrill, C. D.; Soper, J. D., Redox-Active Ligands Facilitate Bimetallic O2 Homolysis at Five-Coordinate Oxorhenium(V) Centers. *Journal of the American Chemical Society* **2010,** *132* (11), 3879-3892.

31. Lippert, C. A.; Hardcastle, K. I.; Soper, J. D., Harnessing Redox-Active Ligands for Low-Barrier Radical Addition at Oxorhenium Complexes. *Inorganic Chemistry* **2011,** *50* (20), 9864-9878.

32. Chirik, P. J.; Wieghardt, K., Radical Ligands Confer Nobility on Base-Metal Catalysts. *Science (New York, N.Y.)* **2010,** *327* (5967), 794-795.

33. Small, B. L.; Brookhart, M., Iron-Based Catalysts with Exceptionally High Activities and Selectivities for Oligomerization of Ethylene to Linear r-Olefins. *Journal of the American Chemical Society* **1998,** *120* (28), 7143-7144.

34. Britovsek, G. J. P.; Gibson, V. C.; McTavish, S. J.; Solan, G. A.; White, A. J. P.; Williams, D. J.; Britovsek, G. J. P.; Kimberley, B. S.; Maddox, P. J., Novel olefin polymerization catalysts based on iron and cobalt. *Chemical Communications* **1998,** (7), 849-850.

35. Zarkesh, R. A.; Ziller, J. W.; Heyduk, A. F., Four-Electron Oxidative Formation of Aryl Diazenes Using a Tantalum Redox-Active Ligand Complex. *Angewandte Chemie International Edition* **2008,** *47* (25), 4715-4718.

36. Munhá, R. F.; Zarkesh, R. A.; Heyduk, A. F., Group transfer reactions of d0 transition metal complexes: redox-active ligands provide a mechanism for expanded reactivity. *Dalton Transactions* **2013,** *42* (11), 3751.

37. Chun, H.; Verani, C. N.; Chaudhuri, P.; Bothe, E.; Bill, E.; Weyhermüller, T.; Wieghardt, K., Molecular and Electronic Structure of Octahedral <i>o</i> -Aminophenolato and <i>o</i> -Iminobenzosemiquinonato Complexes of V(V), Cr(III), Fe(III), and Co(III). Experimental Determination of Oxidation Levels of Ligands and Metal Ions. *Inorganic Chemistry* **2001,** *40* (17), 4157-4166.

38. Chaudhuri, P.; Verani, C. N.; Bill, E.; Bothe, E.; Weyhermüller, T.; Wieghardt, K., Electronic Structure of Bis(<i>o</i> -iminobenzosemiquinonato)metal Complexes (Cu, Ni, Pd). The Art of Establishing Physical Oxidation States in Transition-Metal Complexes Containing Radical Ligands. *Journal of the American Chemical Society* **2001,** *123* (10), 2213-2223.

39. Bellemin-Laponnaz, S.; Welter, R.; Brelot, L.; Dagorne, S., Synthesis and structure of V(V) and Mn(III) NHC complexes supported by a tridentate bis-aryloxide-N-heterocyclic carbene ligand. *Journal of Organometallic Chemistry* **2009,** *694* (5), 604-606.

40. Harris, C. F.; Bayless, M. B.; van Leest, N. P.; Bruch, Q. J.; Livesay, B. N.; Bacsa, J.; Hardcastle, K. I.; Shores, M. P.; de Bruin, B.; Soper, J. D., Redox-Active Bis(phenolate) N-Heterocyclic Carbene [OCO] Pincer Ligands Support Cobalt Electron Transfer Series Spanning Four Oxidation States. *Inorganic Chemistry* **2017,** *56* (20), 12421-12435.

41. Drago, R. S.; Corden, B. B.; Barnes, C. W., Novel cobalt(II)-catalyzed oxidative cleavage of a carbon-carbon double bond. *Journal of the American Chemical Society* **1986,** *108* (9), 2453-2454.

42. Zombeck, A.; Drago, R. S.; Corden, B. B.; Gaul, J. H., Activation of molecular oxygen. Kinetic studies of the oxidation of hindered phenols with cobalt-dioxygen complexes. *Journal of the American Chemical Society* **1981,** *103* (25), 7580-7585.

43. Sedai, B.; Díaz-Urrutia, C.; Baker, R. T.; Wu, R.; Silks, L. A. P.; Hanson, S. K., Comparison of Copper and Vanadium Homogeneous Catalysts for Aerobic Oxidation of Lignin Models. *ACS Catalysis* **2011,** *1* (7), 794-804.

44. Pardini, V. L.; Vargas, R. R.; Viertler, H.; Utley, J. H. P., Anodic cleavage of lignin model dimers in methanol. *Tetrahedron* **1992,** *48* (35), 7221-7228.

45. Rahimi, A.; Azarpira, A.; Kim, H.; Ralph, J.; Stahl, S. S., Chemoselective Metal-Free Aerobic Alcohol Oxidation in Lignin. *Journal of the American Chemical Society* **2013,** *135* (17), 6415-6418.

46. Son, S.; Toste, F. D., Non-Oxidative Vanadium-Catalyzed C□O Bond Cleavage: Application to Degradation of Lignin Model Compounds. *Angewandte Chemie International Edition* **2010,** *49* (22), 3791-3794.

47. Hanson, S. K.; Baker, R. T.; Gordon, J. C.; Scott, B. L.; Silks, L. A. P.; Thorn, D. L., Mechanism of Alcohol Oxidation by Dipicolinate Vanadium(V): Unexpected Role of Pyridine. *Journal of the American Chemical Society* **2010,** *132* (50), 17804-17816.

48. Hanson, S. K.; Baker, R. T., Knocking on Wood: Base Metal Complexes as Catalysts for Selective Oxidation of Lignin Models and Extracts. *Accounts of Chemical Research* **2015,** *48* (7), 2037-2048.

49. Lignin Market size to exceed $1 billion by 2026. *Global Market Insights, Inc.*

50. Li, C.; Zhao, X.; Wang, A.; Huber, G. W.; Zhang, T., Catalytic Transformation of Lignin for the Production of Chemicals and Fuels. *Chemical Reviews* **2015,** *115* (21), 11559-11624.

51. Zakzeski, J.; Bruijnincx, P. C. A.; Jongerius, A. L.; Weckhuysen, B. M., The Catalytic Valorization of Lignin for the Production of Renewable Chemicals. *Chemical Reviews* **2010,** *110* (6), 3552-3599.

52. Steffensmeier, E.; Swann, M. T.; Nicholas, K. M., Mechanistic Features of the Oxidation–Reductive Coupling of Alcohols Catalyzed by Oxo-Vanadium Complexes. *Inorganic Chemistry* **2019,** *58* (1), 844-854.

53. Shiramizu, M.; Toste, F. D., Deoxygenation of Biomass-Derived Feedstocks: Oxorhenium-Catalyzed Deoxydehydration of Sugars and Sugar Alcohols. *Angewandte Chemie International Edition* **2012,** *51* (32), 8082-8086.

54. Shiramizu, M.; Toste, F. D., Expanding the Scope of Biomass-Derived Chemicals through Tandem Reactions Based on Oxorhenium-Catalyzed Deoxydehydration. *Angewandte Chemie International Edition* **2013,** *52* (49), 12905-12909.

55. Tshibalonza, N. N.; Monbaliu, J.-C. M., The deoxydehydration (DODH) reaction: a versatile technology for accessing olefins from bio-based polyols. *Green Chem.* **2020,** *22* (15), 4801-4848.

CHAPTER 2. RADICAL CONTROL IN O-ATOM TRANSFER FROM VERY HIGH-VALENT OXORHENIUM COMPLEXES

2.1 Note on collaboration

All quantification of organics was done by Sulaiman Somani as an undergraduate. Dr. Ashley M. McDaniels is responsible for the electrochemistry and Dr. Cameron Lippert provided the crystal structure for $[Re_2(\mu\text{-}O)(O)_2(ap)_2(isq)_2]$. Computational chemistry was completed by Dr. Caleb F. Harris and Dr. John Berry at U of Wisc.

2.2 Introduction

High valent metal–oxo species are the oxidants in processes ranging from industrial petroleum processing to biological detoxification, energy conversion and storage, environmental remediation, and benchtop organic synthesis. Accordingly, the electronic structures and reactivity of complexes containing metal–oxido bonds have been a subject of ongoing study for over 50 years. Most isolable metal–oxo complexes are closed shell species, but recent theoretical literature has suggested metal–oxyl radials (M=O•) with unpaired spin density at the oxo ligand are the reactive intermediates in numerous low-barrier small molecule bond-making and -breaking redox reactions. These include, but are not limited to, O–O bond formation in natural and artificial photosynthetic systems, epoxidation, and C–H activation.[1-7] These are supported by recent ultrafast spectroscopy experiments which have observed Ti^{III}–O• transients upon photoexcitation of closed-shell titanosilicate Ti^{IV}=O photocatalysts that are active CO_2 reduction and H_2O water splitting.[8] And gas-phase metal–oxide cations of the formula $[MO]^{\bullet +}$ (M = Mg, Mn, Fe) have been extensively investigated for their capacity to undergo thermal H-atom abstraction from hydrocarbons including methane.[9-13] A recent review attributes this kinetically facile CH_4 activation to "the presence of unpaired, high spin density at the abstracting, preferentially terminal oxygen atom".[13]

Given the well-established reactivity of organic and small molecule free radicals, it seems intuitive that M=O• species should be similarly biased for radical-type bond making and breaking. Accordingly, several synthetic water oxidation catalysts have been suggested to operate via a so-called radical coupling (RC) mechanism, whereby radical character at oxygen lowers the kinetic barrier to O–O bond formation. Although there is theoretical and computational support for this proposal in some systems, the general utility of oxygen radical character for bond-making reactivity at oxo ligands remains an open question.

The kinetic effects of unpaired spin on metal–oxo reactivity have been examined most extensively in C–H hydroxylations. Unpaired spin at the oxo ligand was historically considered a prerequisite for radical H-atom abstraction at a terminal oxo ligand. This rationalized, for instance, the capacity of so-called Compound I ferryl (por•)Fe^{IV}=O species to abstract an H-atom in the first step of the canonical hydroxyl rebound mechanism for alkane hydroxylation. But beginning in the mid-1980s, Mayer began compiling evidence that suggested radical character at oxygen was not a prerequisite for H-atom abstraction by a terminal metal–oxo.[14-15] In this model, C–H activation rates by M=O species are a consequence of the thermodynamic oxidizing power and basicity of the complex.

Despite their apparent importance, efforts to generate, stabilize, or rationally incorporate M=O• species into functional catalysts have been mostly stymied. Isolated metal–oxyl complexes are exceedingly rare.[16] Terminal metal–oxyls should be both thermodynamically unstable and kinetically reactive; the properties that make them desirable also make them elusive and synthetically challenging. Moreover, metal–oxyl radicals are unlike organic oxyl radicals, particularly in their ability to delocalize the unpaired spin onto the metal center via the M–O π bonds. Accordingly, the electronic structure of a metal oxyl is described best by MO theory. The classic Ballhausen and Gray MO diagram for a terminal oxo complex in a tetragonal ligand field serves as a convenient starting point.[17] Generation of a metal–oxyl requires introduction of an unpaired spin into the metal-oxo π-bonding manifold. This can be accomplished in two ways as illustrated by the open arrows in Figure 1a: [1] addition of 1e– to an antibonding M–O π* orbital; [2] removal of one electron from a doubly occupied π-bonding MO. Both lower the M–O bond order by 0.5. The former approach is more experimentally accessible. Reduction of a d^2 oxo complex places a single electron into an e symmetry π* MO, but if oxidizing metal complexes are desired, approach 1 is potentially problematic. First, because reduction of a d^2 oxo complex results in occupation of a high energy orbital, the resulting metal complexes are outer-sphere reductants. Second, in cases where the metal center is more electropositive than oxygen—the typical situation for most Werner complexes—the primary contributors to the π* orbitals are the metal d_{xz} and d_{yz} atomic orbitals, so the unpaired spin is primarily localized on the metal. Approach 2 addresses both of these issues. Oxidation of a d^0 oxo complex will generate a strong oxidant. But because the e symmetry ($p_{x/y}$) π-bonding orbitals are typically low in energy and among other ligand-centered MOs, generation of this type of species is much more synthetically challenging and has not been conclusively demonstrated in condensed phases.

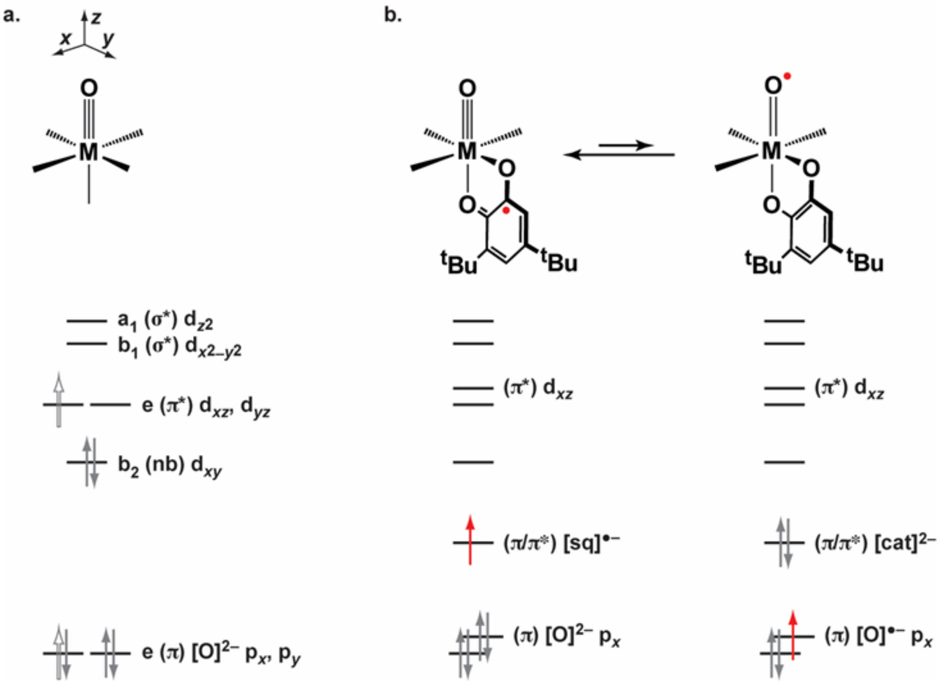

Figure 2-1. Qualitative MO diagrams illustrating potential routes to metal–oxyl radicals in a tetragonal ligand field. (a) Open gray arrows show where the M–O bond order in a d^2 metal oxo is reduced from 3.0 to 2.5 by addition of 1e– to a M–O π* orbital or removal

We proposed that redox-active ligands might provide a route to generate stabilized metal–oxo complexes that exhibit oxidizing oxyl radical-type reactivity. The key feature of this strategy is the introduction of a low-lying ligand-centered hole that is appropriately positioned to delocalize into the M–O_{oxo} π-bonding manifold. For example, the semiquinonate $[sq]^{•–}$ ligand trans to the oxo in Figure 2-1b has its unpaired electron in a π-symmetry MO that overlaps with d_{xy} as well as one of the two $d_{xz/yz}$ orbitals that are used to form the M≡O π bonds. Accordingly, symmetry allowed mixing of the $[sq]^{•–}$ ligand SOMO with a M≡O π bond delocalizes the $[sq]^{•–}$ hole into the M–O_{oxo} π system and imparts oxyl radical character to the oxo ligand. In the limit of full intraligand $[O]^{2-} \rightarrow [sq]^{\bullet-}$ charge transfer (CT), the M–O_{oxo} bond order decreases from 3.0 to 2.5, making the complex an oxyl radical.

Presented below is a demonstration of this "masked oxyl" strategy. We describe the preparation and characterization of a new S=1/2 d^0 dioxorhenium complex with a ligand centered radical, one oxidation state above Re(VII). Its capacity to oxidize the stable triphenylmethyl ($Ph_3C\bullet$) radical is reported. Computational data show an iminosemiquinonate radical ligand imparts radical character to the closed-shell metal–oxo group, and mechanistic data are presented to suggest the radical reactivity of these complexes reflects oxyl radical character in the ground electronic state. These design principles form a basis for generation of an entirely new class of stabilized metal–oxyls.

2.3 Results

2.3.1 *Oxidation of $[Re(O)_2(ap)_2]^-$*

Our search for a monomeric S=1/2 oxorhenium complex that satisfied the "masked oxyl" design criteria in Figure 2-1b began with the previously reported $[Re(O)_2(ap)_2]^-$ anion ($[ap]^{2-}$ = 2,4-di-tert-butyl-6-(phenylamido)phenolate). The cyclic voltammogram (CV) of $[Re(O)_2(ap)_2]^-$ in CH_2Cl_2 solutions containing 0.1 M tetra-n-butylammonium hexfluorophosphate ($[nBu_4N][PF_6]$) shows a single quasi-reversible 1e– oxidation at E_{pa} = –0.228 V vs $Fc^{+/0}$ (Figure 2, blue). Accordingly, treatment of the navy blue MeCN solutions of $[Re(O)_2(ap)_2]^-$ with 1 equiv of a suitably strong oxidant ($[Ag][PF_6]$, $[NO][BF_4]$, or $[Cp_2Fe][PF_6]$) affords an immediate color change to dark green followed by precipitation of a green powder over 5 to 10 min at ambient temperature, which was isolated by vacuum filtration under N_2. As discussed below, the choice of oxidant impacts the purity and stability of the inorganic product; the highest yields (87%) and cleanest product were obtained using $[Cp_2Fe][PF_6]$. The green species is paramagnetic, as evidenced by lack of any observable ^{1}H NMR resonances and a solution magnetic moment (μ_{eff}) of 1.99 in CD_2Cl_2, which is close to 1.73, the expected spin-only value for an S=1/2 center.

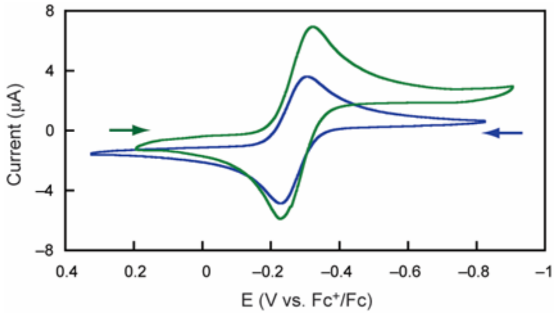

Figure 2-2. Cyclic voltammograms of $[Re(O)_2(ap)_2]^-$ (blue) and $[Re(O)_2(ap)(isq•)]$ (green) in CH_2Cl_2 containing 0.1 M $[nBu_4N][PF_6]$, 10 mm Pt electrode, 100 mV s^{-1} scan rate, 25 °C.

The cyclic voltammogram of the green oxidation product (Figure 2-2, green) is essentially identical to that of $[Re(O)_2(ap)_2]^-$, except the open circuit potential is shifted to the positive values so the first observable redox event is a cathodic wave at $E_{pc} = -0.323$ V vs $Fc^{+/0}$. The similarity of the spectra in Figure 2-2 imply that the isolated green product from chemical oxidation is the same one observed upon electrochemical $1e^-$ oxidation of $[Re(O)_2(ap)_2]^-$.

2.3.2 Structure of $[Re(O)_2(ap)(isq)]$

2.3.2.1 Solid state structure

Slow diffusion of pentane into a saturated toluene solution of the green oxidation product at 25 °C in the absence of light afford single crystals suitable for analysis by X-ray diffraction. A thermal ellipsoid plot is shown in Figure 2-3. It contains a charge neutral rhenium center with pseudo-octahedral geometry. The gross coordination geometry is unchanged from $[Re(O)_2(ap)_2]^-$. Two terminal oxo ligands occupy cis coordination sites, as expected for a d^0 metal center, with an O–Re–O bond angle of 101.2(2)°. The remaining four sites are filled by two bidentate aminophenol-derived ligands. The Re–N bonds are approximately trans disposed, so each oxo ligand is trans to a Re–O_{ap} bond. Selected bond distances for the $[Re(O)_2(ap)_2]^-$ anion and its 1e– oxidation product are collected in Figure 2-4. Charge balance confirms the complex is one redox level above $[Re(O)_2(ap)_2]^-$, suggesting the solid-state structure is the same as the S=1/2 species in solution (vide supra). The modest potential required for oxidation of $[Re(O)_2(ap)_2]^-$ are inconsistent with oxidation of the d^0 Re(VII) center, suggesting the electron is removed from one of the ligands. The Re–O_{oxo} bond lengths of 1.728(5) Å and 1.726(5) Å in the oxidized complex are contracted slightly from those in $[Re(O)_2(ap)_2]^-$ (1.742(2) Å and 1.732(2) Å), consistent with enhanced electrostatics and/or covalency in the Re–O bonding and inconsistent with oxidation of an oxido ligand $[O]^{2-}$ to an oxyl radical $[O\bullet]^-$. Amidophenolates, however, are well-known redox-active (sometimes "non-innocent") ligands, and the observed $E_{1/2}$ value is well within the range expected for generation of an iminosemiquinonate radical.

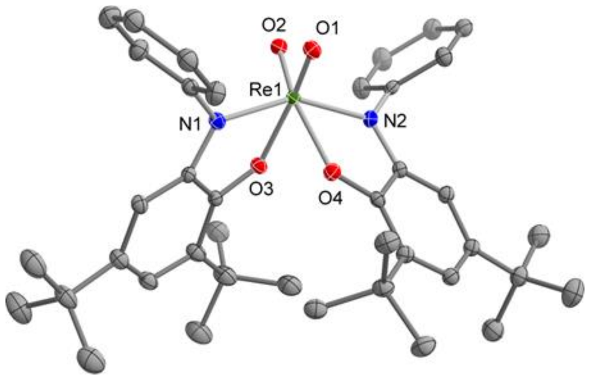
O2
O1
Re1
N1
N2
O3
O4

Figure 2-3. Solid-state structure of [Re(O)$_2$(ap)(isq•)] shown with 50% probability ellipsoids. Hydrogen atoms omitted for clarity

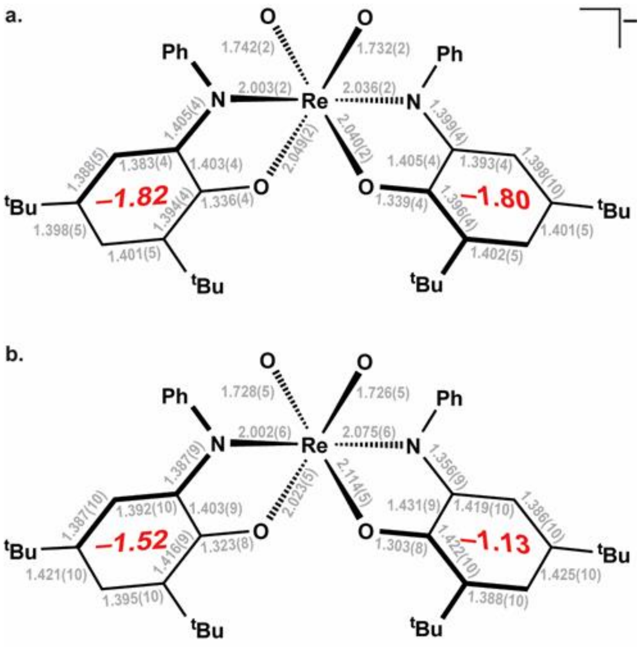
a.
O
O
1.742(2)
1.732(2)
Ph
Ph
2.003(2)
2.036(2)
N
Re
N
1.405(4)
2.049(2)
2.040(2)
1.399(4)
1.388(5)
1.383(4)
1.403(4)
1.405(4)
1.393(4)
1.398(10)
−1.82
−1.80
O
O
1.336(4)
1.339(4)
1.394(4)
1.396(4)
tBu
tBu
1.398(5)
1.401(5)
1.401(5)
1.402(5)
tBu
tBu
b.
O
O
1.728(5)
1.726(5)
Ph
Ph
2.002(6)
2.075(6)
N
Re
N
1.387(9)
2.023(5)
2.114(5)
1.356(9)
1.387(10)
1.392(10)
1.403(9)
1.431(9)
1.419(10)
1.386(10)
−1.52
−1.13
O
O
1.323(8)
1.303(8)
1.416(9)
1.422(10)
tBu
tBu
1.421(10)
1.425(10)
1.395(10)
1.388(10)
tBu
tBu

Figure 2-4. Schematic of selected bond lengths (Å) for complexes (a) [Re(O)$_2$(ap)$_2$]$^-$ and its 1e– oxidation product (b) [Re(O)$_2$(ap)(isq•)]. Red text are the computed metrical oxidation states (MOS) for each ligand.

The aminophenol ligands in the oxidized complex are crystallographically inequivalent, and the bond distances suggests they are also electronically inequivalent (Figure 4b). Both show a quinoid-type pattern of four long and two short C–C bonds in the amidophenoxide moieties that typically accompanies ligand oxidation. Brown and co-workers created a metrical oxidation state (MOS) calculator that uses the aggregate bond distances to compute the ligand charge by comparison to previously reported crystallographic data.[18] The computed MOS values for a idealized closed-shell $[ap]^{2–}$ ligand and an $[isq•]^{–}$ radical ($[isq•]^{–}$ = 2,3-di-tert-butyl-6-(phenylimino)semiquinonate) are –2.0 and –1.0, respectively. Accordingly, the combined MOS values for the two closed-shell ligands in $[Re(O)_2(ap)_2]^{–}$ are expected to be –4.0; removal of 1e– from the aminophenol ligand(s) should give a product with a combined MOS total of –3.0. The electronic structure of this oxidized complex could exist anywhere between two limiting extremes that parallel the classic Robin-Day classifications for mixed valency. Oxidation of a single $[ap]^{2–}$ ligand gives the molecule C_1 symmetry and makes the two aminophenol-derived ligands, as well as the oxo ligands, inequivalent. In this limit, the MOS calculator would be expected to return values of –2.0 for the $[ap]^{2–}$ ligand and –1.0 for the $[isq•]^{–}$ ligand. However, if the unpaired spin is fully delocalized across both of the aminophenol ligands, the complex is structurally and electronically symmetrical with C_2 symmetry. In this limit, the bond distances are intermediate between [ap]2– and $[isq•]^{–}$ and the MOS calculator would return values of –1.5 for each ligand.

The oxidation product MOS values of –1.52 ± 0.11 and –1.13 ± 0.07 (Figure 2-4) fall between the extremes described above, and the sum of the two MOS values is –2.63 ± 0.13, seemingly suggesting oxidation of the ligands by more than 1e–. However, the combined MOS values in $[Re(O)_2(ap)_2]^{–}$ (Figure 4a) are –3.62 ± 0.09. $[Re(O)_2(ap)_2]^{–}$ exhibits no spectroscopic evidence of a ligand-centered radical. Brown has previously suggested that non-integer MOS values often reflect metal–ligand π-bonding interactions. In this case, the Re(VIII) centers in both $[Re(O)_2(ap)_2]^{–}$ and its oxidized congener should be excellent π-acceptors and the $[ap]^{2-}$ ligands have filled π-symmetry MOs. Accordingly, the ca. +0.4 increase in the combined MOS values in both $[Re(O)_2(ap)_2]^-$ and the oxidized complex vs. their idealized values can be reasonably ascribed to $[ap]^{2-}\rightarrow Re$ π donation. In sum, the metrical data are consistent with 1e– oxidation of $[Re(O)_2(ap)_2]^-$ producing a product in which a total of 1.0 unit of charge is removed from the aminophenol ligands. For simplicity, the oxidized species is hereafter denoted $[Re(O)_2(ap)(isq\bullet)]$ to emphasize the aminophenol ligand-centered hole. However, the solid-state data are insufficient to distinguish a localized vs. delocalized charge distribution, and it is possible that the observed asymmetry in the ligands represents a crystal packing effect that is not representative of the solution structure.

Solid-state infrared spectroscopy (ATR–FTIR) data for $[Re(O)_2(ap)_2]^-$ and $[Re(O)_2(ap)(isq\bullet)]$ are shown in Figure 2-5. Two bands at 874 and 847 cm^{-1} in the spectrum of $[Re(O)_2(ap)_2]^-$ are within the range typical of Re=O bonds and consistent with the $\nu_s(ReO_2)$ and $\nu_{as}(ReO_2)$ pair expected for a cis-ReO_2 unit.[19] These assignments were confirmed using ^{18}O-labeled materials, which were prepared by aerobic oxidation of [Re(O)(ap)2]$^-$ in MeCN solutions containing an excess of $^{18}OH_2$. All three $[Re(^{18/16}O)_2(ap)_2]^-$ isotopologues were observed by electrospray ionization mass spectrometry (ESI–MS); the major product in all preparations was $[Re(^{18}O)(^{16}O)(ap)_2]^-$ as evidenced by a molecular ion at 811 m/z. Comparison of the FTIR spectrum of the ^{18}O-enriched material to unlabeled $[Re(O)_2(ap)_2]^-$ shows a shift of the ReO_2 bands to 828 and 800 cm^{-1} (Figure 5a), which matches closely the 43 cm^{-1} reduction in frequency computed using Hooke's Law. The ReO_2 stretches in $[Re(O)_2(ap)(isq\bullet)]$ appear at 910 and 875 cm^{-1} (Figure 2-5b). The shift to higher frequencies upon oxidation of $[Re(O)_2(ap)_2]^-$ is consistent with enhanced Re–O_{oxo} bonding in [Re(O)$_2$(ap)(isq•)], mirroring the contraction of the Re–O_{oxo} bonds observed in the X-ray structural data described above.

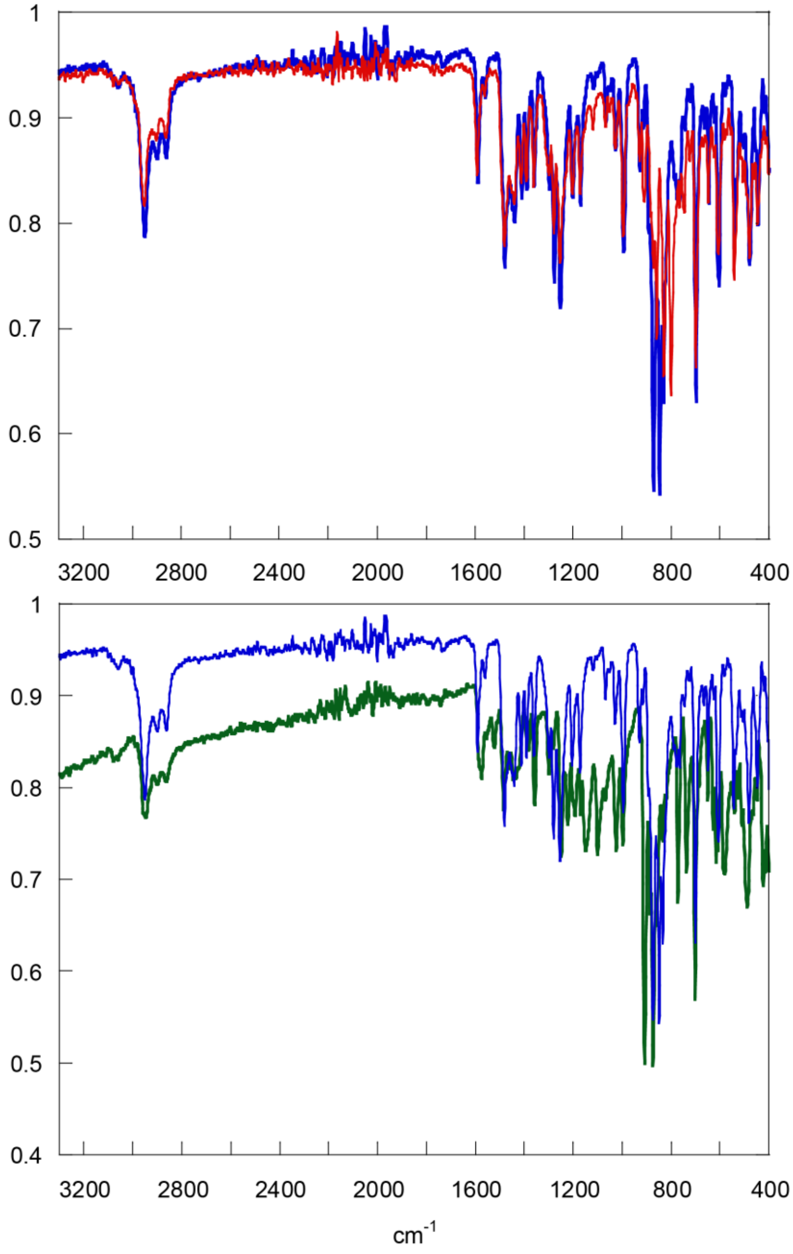

Figure 2-5. Full ATR–FTIR spectra of (a) [Re(O)$_2$(ap)$_2$]$^-$ (blue) and [Re(^{18}O)(^{16}O)(ap)$_2$]$^-$ (red), (b) [Re(O)$_2$(ap)$_2$]$^-$ (blue) and [Re(O)$_2$(ap)(isq•)] (green)

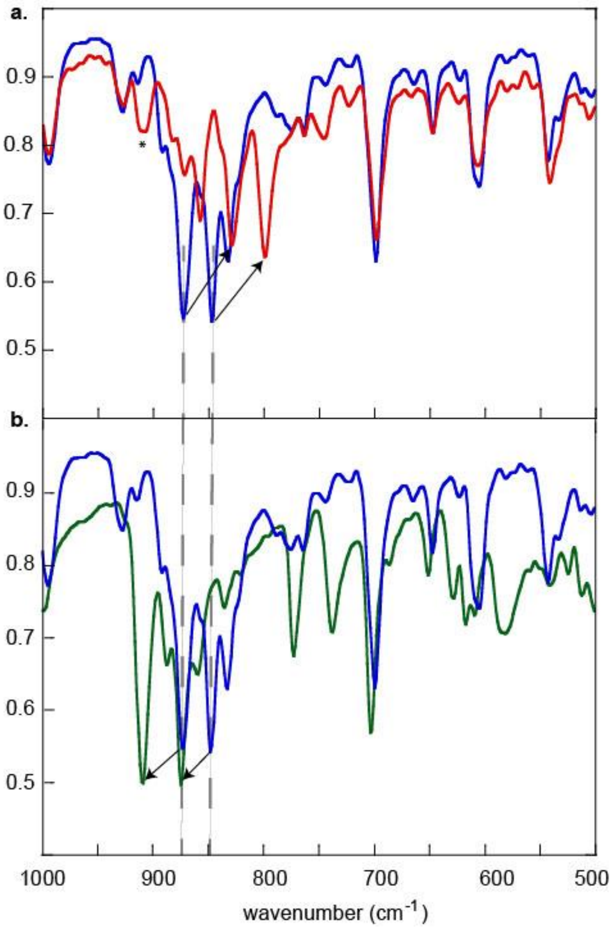

Figure 2-6. ATR–FTIR spectra of (a) $[Re(O)_2(ap)_2]^-$ (blue) and $[Re(^{18}O)(^{16}O)(ap)_2]^-$ (red), with arrows indicating shifts of the ReO_2 stretching bands upon labeling, and (b) $[Re(O)_2(ap)_2]^-$ (blue) and $[Re(O)_2(ap)(isq\bullet)]$ (green), with arrows indicating shifts the ReO_2

2.3.2.2 Computed electronic structure

Structure of $[Re(O)_2(ap)(isq\bullet)]$: 3. Computed electronic structure. Single-point and density functional theory (DFT) calculations were performed to gain insight into the electronic structure of $[Re(O)_2(ap)(isq^\bullet)]$. The lowest energy solution which emerged using the B3LYP density functional was a standard doublet (S=1/2) ground state and the geometry was found to be in good agreement with the metrical parameters observed in the crystallography data. In contrast to the solid-state structure, the computed minimum is

]

effectively symmetrical about the Re center, as manifested by the singly occupied molecular orbital (SOMO), which is distributed equally across both aminophenol ligands with the shape characteristic of an [isq•]$^-$ radical. Consistent with its formulation as [Re(O)$_2$(ap)(isq•)], 91% of the spin density is on the aminophenol-derived ligands, but the observation of 5% of the total spin on the terminal oxos is notable because it is consistent with significant oxyl character in the ground state, as discussed below.

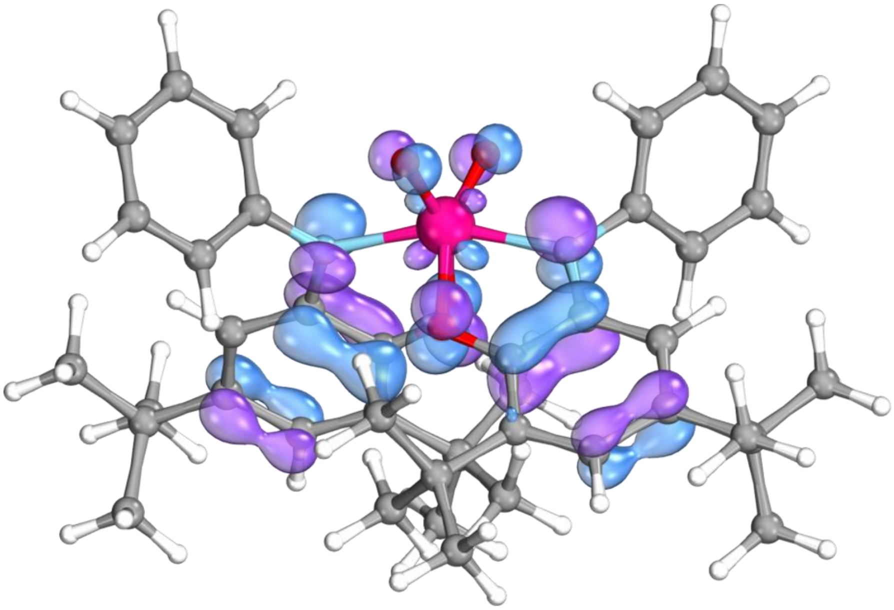

Figure 2-7. SOMO of [Re(O)$_2$(ap)(isq●)] generated with IboView

2.3.3 [Re(O)$_2$(ap)(isq•)] O-atom transfer

2.3.3.1 Via H-atom abstraction

Initial attempts to grow X-ray quality single crystals of [Re(O)$_2$(ap)(isq•)] were challenged by a degradation reaction. This was first observed in acetone solutions of green

[Re(O)$_2$(ap)(isq•)], which become an intense purple color after 1 day at ambient temperature under N$_2$ (Figure 2-8a) Removal of the solvent under vacuum afforded a purple powder, and MALDI–MS analysis of the of the isolated solids showed a molecular ion peak at 1602 m/z, corresponding to the molecular weight of two equivalents of [Re(O)$_2$(ap)(isq•)] less one O atom. The rate of this conversion varies with solvent. Whereas UV–vis spectra of [Re(O)$_2$(ap)(isq•)] in THF or CH$_2$Cl$_2$ show features characteristic of the degradation product in hours under N$_2$ (Figure 2-8b), the UV–vis spectrum [Re(O)$_2$(ap)(isq•)] in C$_6$H$_6$ is essentially unchanged over 24 h, and 14 d were required to observe a comparable (15%) yield of the purple product (Figure 2-8c). Formation of the purple material is accelerated slightly by exposure to air, but light significantly increases the rate of the degradation reaction. Exposure of a C$_6$H$_6$ solution of [Re(O)$_2$(ap)(isq•)] to a 16 W 2700K (soft white) compact fluorescent light (CFL) gave ca. 15% conversion to the purple product over 24 h. Conversely, the UV–vis spectrum of [Re(O)$_2$(ap)(isq•)] in CH$_2$Cl$_2$ was unchanged over 4 d in the dark at ambient temperature.

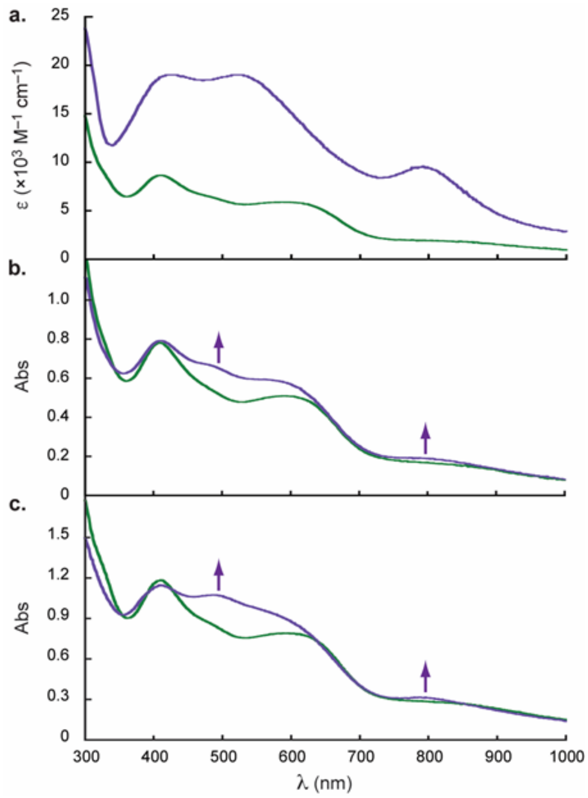

Figure 2-8. (a) UV–vis absorption spectra of [Re(O)$_2$(ap)(isq•)] (green line) and [Re$_2$(μ-O)(O)$_2$(ap)$_2$(isq•)$_2$] (purple line) in C$_6$H$_6$. (b) THF solution of 9.3 × 10–5 M [Re(O)$_2$(ap)(isq•)] t = 0 (green line) and t = 24 h (purple line) under N$_2$ at 25 °C showing 12.8% con conversion to [Re$_2$(μ-O)(O)$_2$(ap)$_2$(isq•)$_2$]. (c) C$_6$H$_6$ solution of 1.6 × 10–4 M [Re(O)$_2$(ap)(isq•)] at t = 0 (green line) and t = 14 d (purple line) under N$_2$ at 25 °C showing 15.6% conversion to [Re$_2$(μ-O)(O)$_2$(ap)2(isq•)$_2$]. % conversion determined by iterative fits of the UV–vis data to linear combinations of the isolated spectra for [Re(O)$_2$(ap)(isq•)] and [Re$_2$(μ-O)(O)$_2$(ap)$_2$(isq•)$_2$].

X-ray quality crystals of the purple degradation product were obtained by slow evaporation of a saturated MeCN solution at –20 °C. The solid-state structure (Figure 2-9a) contains a charge neutral oxo-bridged dirhenium complex with approximate C$_2$ symmetry. Each Re center has pseudo-octahedral geometry. Two terminal oxo ligands are cis to the μ-oxo linkage, and the Re–O$_{oxo}$ bonds are approximately eclipsed (γ = 6.6° and 10.6° in the two crystallographically independent dimer molecules). Two cis-oriented bidentate aminophenol-derived ligands take up the remaining four sites about each Re with Re–N bonds trans to the μ-oxo ligand and a Re–O trans to each of terminal oxos. Examination of the aminophenol ligand bond distances suggests the symmetry-inequivalent ligands are also electronically inequivalent (Figure 2-9b). In the ligand trans to the μ-oxo bridge, the C–C bond distances within the aminophenol ring are equidistant within 3σ (1.40 ± 0.02 Å) and the C–N and C–O bond distances are consistent with single bonds, suggesting the ligands are fully reduced, closed-shell $[ap]^{2-}$ dianions. In contrast, the aminophenol rings trans to the terminal oxo groups have contracted C–N and C–O bond distances and show quinoid-type deviations from aromaticity, typical of the radical $[isq\bullet]^{-}$ semiquinonate monoanion. These assignments are reflected in the mean computed MOS values of –1.86 ± 0.23 and –1.24 ± 0.22 for the ligands trans to $Re–O_{\mu\text{-oxo}}$ and $Re–O_{oxo}$, respectively (Figure 2-9b). The sum of these data suggest that the dimeric complex is best formulated as $[Re_2(\mu\text{-}O)(O)_2(ap)_2(isq\bullet)_2]$, with the radicals primarily localized on the ligands trans to the terminal oxos.

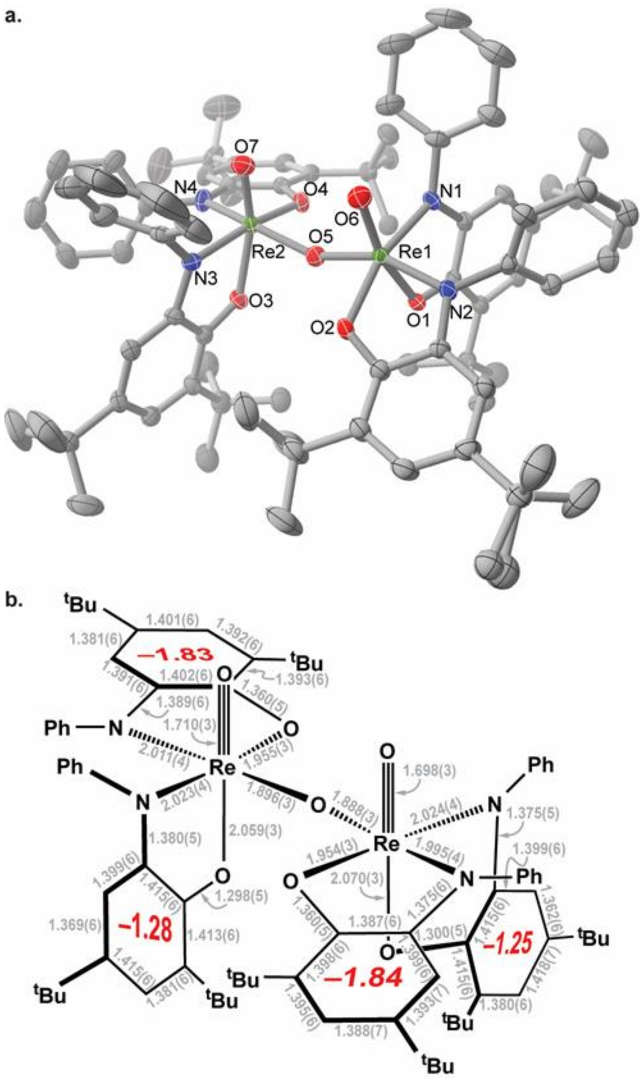
a.
O7
N4
O4
O6
N1
O5
Re2
Re1
N3
O3
O2
O1
N2
b.
tBu
1.401(6)
1.392(6)
1.381(6)
−1.83
tBu
1.391(6)
1.402(6)
1.393(6)
O
1.389(6)
1.360(5)
Ph
N
1.710(3)
O
2.011(4)
1.955(3)
O
Ph
Re
1.698(3)
Ph
1.896(3)
O
1.888(3)
2.024(4)
N
N
2.023(4)
1.375(5)
1.380(5)
2.059(3)
1.954(3)
Re
1.995(4)
1.399(6)
1.399(6)
O
O
2.070(3)
N
Ph
1.415(6)
1.298(5)
1.360(5)
1.375(6)
1.415(6)
1.362(6)
1.369(6)
−1.28
1.413(6)
1.387(6)
1.300(5)
−1.25
tBu
O
1.399(6)
1.415(6)
1.398(6)
−1.84
1.415(6)
1.418(7)
tBu
tBu
1.381(6)
tBu
1.395(6)
1.393(7)
tBu
1.380(6)
1.388(7)
tBu

Figure 2-9. (a) Solid-state structure of [Re_2(μ-O)$(O)_2(ap)_2$(isq•$)_2$] shown with 50% probability ellipsoids. Hydrogen atoms omitted for clarity. A second, crystallographically unique dimer is not shown. (b) Schematic of selected bond lengths (Å) and computed MOS values (red) for each ligand in one dimer molecule.

Formation of [Re_2(μ-O)$(O)_2(ap)_2$(isq•$)_2$] from 2 equiv [Re$(O)_2$(ap)(isq•)] is a net 2e– process, wherein each Re center is reduced from Re(VII) to Re(VI). The mean terminal Re–O_{oxo} bond distance of 1.708(8) Å in [Re_2(μ-O)$(O)_2(ap)_2$(isq•$)_2$] is within the range expected for monooxo Re≡O triple bonds and matches the Re–O_{oxo} bonds in previously reported monomeric [Re(O)(ap)(isq•)X] complexes (1.7090(16) when X– = OC_6Cl_5–;

1.7064(17) Å when X– = Cl–) Re(VI) that are structural homologs for the octahedral [Re(O)(ap)(isq•)(μ-O)] fragment. These data are consistent with the added electron occupying a π-nonbonding orbital (dxy when the terminal Re–O_{oxo} bond is coincident with the z axis). The long Re–Re distances of 3.705(6) and 3.673(6) Å preclude metal–metal bonding. Formulation as [Re_2(μ-O)$(O)_2$$(ap)_2$$(isq•)_2$] implies four total unpaired spins, with two d1 ions each coordinated to a free radical [isq•]– ligand, but the complex is diamagnetic, as evidenced by the observation of sharp ^{1}H NMR resonances (δ = +0.00 to 8.00 ppm; FWHM = 111-1518 Hz) in MeCN at 25 °C, suggesting the spins are antiferromagnetically coupled, as discussed below.

Conversion of 2 equiv [Re$(O)_2$(ap)(isq•)] to [Re_2(μ-O)$(O)_2$$(ap)_2$$(isq•)_2$] is balanced by loss of an oxygen atom. This is sometimes termed "incomplete" oxo transfer. Here the fate of the O atom in unknown. Kinetics of the degradation in CH_2Cl_2 were monitored by UV–vis spectroscopy at varying initial Re concentrations. The data exhibited a first order dependence on [Re$(O)_2$(ap)(isq•)] Table 2-1, arguing against bimetallic RC-type coupling to produce O_2. As described above, the rate of the dimerization reaction is qualitatively faster in solvents with weaker C–H bonds, suggesting a mechanism of initial hydrogen-atom transfer (HAT) might be operative.

Table 2-1. Order determination for degradation of [Re(O)$_2$(ap)(isq•)] to [Re$_2$(μ-O)(O)$_2$(ap)$_2$(isq•)$_2$] in DCM

	Initial [Re]	Rate([Re]/h)$_{3h}$	Rate([Re]/h)$_{19h}$	Rate([Re]/h)$_{26h}$
1	2.5×10^{-3}	1.1×10^{-3}	1.1×10^{-4}	7.4×10^{-5}
2	1.2×10^{-3}	5.6×10^{-4}	6.6×10^{-5}	3.9×10^{-5}
3	8.2×10^{-4}	3.6×10^{-4}	4.0×10^{-5}	3.0×10^{-5}
4	6.2×10^{-4}	3.3×10^{-4}	3.9×10^{-5}	2.9×10^{-5}

Water or solvent-derived oxidation products were not observed by mass spectrometry or NMR spectroscopy, but addition of 1 equiv 9,10-dihydroanthracene (DHA) to [Re(O)$_2$(ap)(isq•)] in C_6H_6 gave clean conversion to the bis(μ-oxo) dirhenium complex [Re$_2$(μ-O)$_2$(ap)$_2$(isq•)$_2$] over 24 h at ambient temperature, consistent with the reaction stoichiometry shown in eq 1. We have previously reported the formation of [Re$_2$(μ-O)$_2$(ap)$_2$(isq•)$_2$] from rapid dimerization of [Re(O)(ap)(isq•)], and data below show [Re$_2$(μ-O)$_2$(ap)$_2$(isq•)$_2$] is also generated by O-atom transfer from [Re$_2$(μ-O)(O)$_2$(ap)$_2$(isq•)$_2$] (Scheme 2-2c). Accordingly, the apparent intermediacy of [Re$_2$(μ-O)(O)$_2$(ap)$_2$(isq•)$_2$] or [Re(O)(ap)(isq•)] in the reaction with DHA (Scheme 2-1) suggests facile deoxygenation upon net transfer of 2 equiv H• to [Re(O)$_2$(ap)(isq•)].

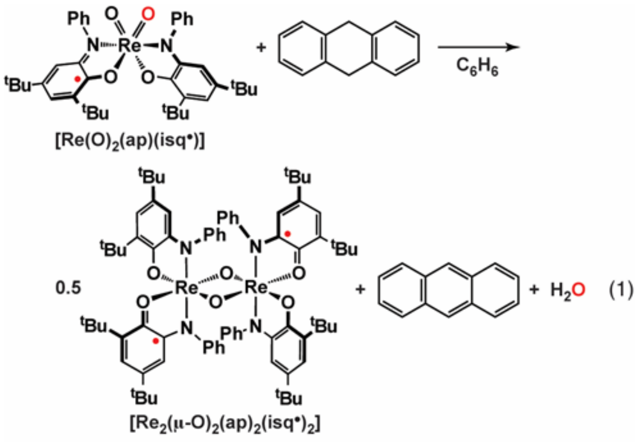

Scheme 2-1. Generation of [Re$_2$(μ-O)$_2$(ap)$_2$(isq)$_2$] from reaction of [Re(O)$_2$(ap)(isq•)] with DHA

2.3.3.2 PPh$_3$ Oxidation

Treating a green CH_2Cl_2 solution of [Re(O)$_2$(ap)(isq•)] with 0.5 equiv PPh$_3$ affords an immediate color change to dark purple with a UV–vis spectrum that is identical to isolated [Re$_2$(μ-O)(O)$_2$(ap)$_2$(isq•)$_2$]. Concomitant formation of OPPh$_3$ was confirmed by ^{1}H NMR spectroscopy. Accordingly, the conversion of 2 [Re(O)$_2$(ap)(isq•)] + PPh$_3$ → [Re$_2$(μ-O)(O)$_2$(ap)$_2$(isq•)$_2$] + OPPh$_3$ is a balanced reaction that can be envisioned to occur by O-atom transfer from [Re(O)(ap)(isq•)] to PPh$_3$ followed by trapping of the putative monooxo [Re(O)(ap)(isq•)] intermediate by a second equivalent of [Re(O)(ap)(isq•)], as shown in Scheme 2-2.

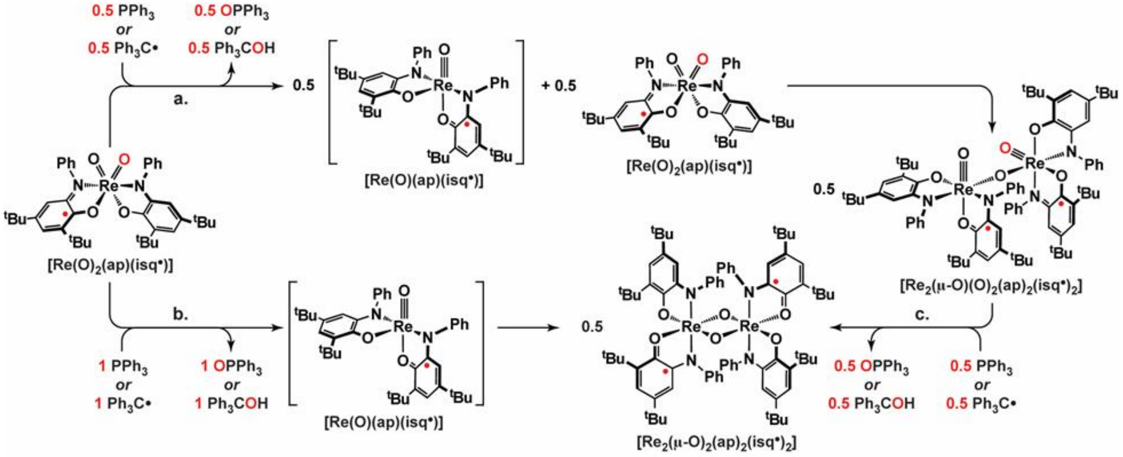
0.5 PPh₃
or
0.5 Ph₃C•
0.5 OPPh₃
or
0.5 Ph₃COH
a.
0.5
+ 0.5
[Re(O)(ap)(isq•)]
[Re(O)₂(ap)(isq•)]
[Re(O)₂(ap)(isq•)]
[Re₂(μ-O)(O)₂(ap)₂(isq•)₂]
b.
1 PPh₃
or
1 Ph₃C•
1 OPPh₃
or
1 Ph₃COH
[Re(O)(ap)(isq•)]
0.5
[Re₂(μ-O)₂(ap)₂(isq•)₂]
c.
0.5 OPPh₃
or
0.5 Ph₃COH
0.5 PPh₃
or
0.5 Ph₃C•

Scheme 2-2. Reaction stoichiometry for OAT from [Re(O)$_2$(ap)(isq•)] to PPh$_3$ or Ph$_3$C•

Addition of 10 equiv PPh$_3$ to CH$_2$Cl$_2$ solutions of [Re(O)$_2$(ap)(isq•)] produces a different purple solution, with a UV–vis absorption spectrum that matches exactly the bis(μ-oxo) dirhenium complex [Re$_2$(μ-O)$_2$(ap)$_2$(isq•)$_2$]. As noted above, formation of [Re$_2$(μ-O)$_2$(ap)$_2$(isq•)$_2$] has been previously shown to occur by rapid dimerization of the five-coordinate monooxo species [Re(O)(ap)(isq•)]. In this context, the reaction with excess PPh$_3$ might completely consume [Re(O)$_2$(ap)(isq•)], driving the reaction towards the bis(μ-oxo) (Scheme 2-2b). However, the same [Re$_2$(μ-O)$_2$(ap)$_2$(isq•)$_2$] dimer is quantitatively obtained upon treating [Re$_2$(μ-O)(O)$_2$(ap)$_2$(isq•)$_2$] with 1 equiv PPh$_3$ (Scheme 2-2c). The net reaction stoichiometry is the same following the a + c or b paths in Scheme 2-2: 2 [Re(O)$_2$(ap)(isq•)] + 2 PPh$_3$ → [Re$_2$(μ-O)$_2$(ap)$_2$(isq•)$_2$] + 2 OPPh$_3$. Accordingly, the potential intermediacy of [Re(O)(ap)(isq•)] or [Re$_2$(μ-O)(O)$_2$(ap)$_2$(isq•)$_2$] in the reaction with excess PPh$_3$ cannot be inferred from the observed product distribution.

2.3.3.3 Ph$_3$C trapping

Treating solutions of [Re(O)$_2$(ap)(isq•)] with triphenylmethyl radical Ph$_3$C• in C_6H_6 affords a color change from green to purple over hours at ambient temperature. The inorganic products of this reaction mirror those described above for O-atom transfer to PPh3. Accordingly, reaction with 0.5 equiv Ph$_3$C• followed by column chromatography on silica gel gave [Re$_2$(μ-O)(O)$_2$(ap)$_2$(isq•)$_2$] as the major Re-containing product, as evidenced by its characteristic UV–vis and MALDI–MS spectra. Reaction of [Re(O)$_2$(ap)(isq•)] with excess Ph$_3$C•, or addition of 1 equiv Ph$_3$C• to isolated [Re$_2$(μ-O)(O)$_2$(ap)$_2$(isq•)$_2$], in C_6H_6 gave [Re$_2$(μ-O)$_2$(ap)$_2$(isq•)$_2$]. Because the triphenylmethyl radical monomer–dimer equilibrium in C_6H_6 strongly favors the Gomberg dimer (ca. 2% Ph$_3$C•), the majority of the stoichiometric reactions occur with a large excess of dissolved [Re] relative to [Ph$_3$C•]. Gas chromatography–mass spectrometry (GC–MS) analysis of the reaction mixtures revealed that triphenylmethanol Ph$_3$COH was the major organic product under all conditions. Minor products included benzophenone and triphenylmethane. The Ph$_3$COH yields vary with different preparations of [Re(O)$_2$(ap)(isq•)]. For reactions of [Re(O)$_2$(ap)(isq•)] + 0.5 Ph$_3$C•, quantification by GC–FID gave Ph$_3$COH yields as high as 69% against a control reaction containing no Re; average Ph$_3$COH yields were 45% after 24 h. The sub-stoichiometric organic yields reflect competing side reactions, including consumption of the Gomberg dimer by the product of C–O bond formation, as detailed below. Exclusion of ambient light had no measurable impact on the Ph$_3$COH yield. Reaction of Ph$_3$C• + O_2 without Re gives no Ph$_3$COH under conditions analogous to those employed in Scheme 2-2, suggesting autoxidation is not the primary path to Ph$_3$COH.

In total, the observed Re and organic products are consistent with the oxo-transfer reaction stoichiometries shown in Scheme 2-2. However, the reactions with Ph_3C• are not balanced because each equivalent of Ph_3COH generated requires one additional H•. The immediate product of O-atom addition to Ph_3C• is a triphenylmethoxyl Ph_3CO• radical, which undergoes a rapid 1,2-phenyl shift to afford the α-phenoxyldiphenylmethyl radical. Accordingly, high yields of Ph_3COH are inconsistent with generation of a free Ph_3CO• radical intermediate, suggesting the "adventitious" H• is delivered to an intact Re–$OCPh_3$ bond.

2.3.3.4 Alkoxide intermediates and "adventitious" H

To probe the potential intermediacy of 1e– transfer products in the net O-atom transfer to Ph_3C•, a reaction of the putative products of initial outer-sphere electron transfer (ET) was independently performed. Adding 1 equiv $[Ph_3C][BF_4]$ to $[Re(O)_2(ap)_2]^-$ in C_6H_6 affords an immediate color change from navy blue to purple with a UV–vis spectrum that does not match either of the μ-oxo dimers but closely resembles the previously reported [Re(O)(ap)(isq•)(OC_6Cl_5)] alkoxide complex. Analysis of the solution by ESI–MS showed a molecular ion peak at 1052 m/z consistent with formulation of the purple species as the triphenylmethoxide complex [Re(O)(ap)(isq•)($OCPh_3$)]. C_6H_6 solutions containing [Re(O)(ap)(isq•)($OCPh_3$)] are stable for days; monitoring by UV–vis showed no conversion to [Re_2(μ-O)$(O)_2(ap)_2$(isq•$)_2$] over two days at ambient temperature. Observation of a long lived C–O coupling product in the $[Ph_3C]^+$ + $[Re(O)_2(ap)_2]$– reaction suggested that the H• required for Ph_3COH formation from Ph_3C• + [$Re(O)_2$(ap)(isq•)] did not derive from solvent, glass or a persistent impurity.

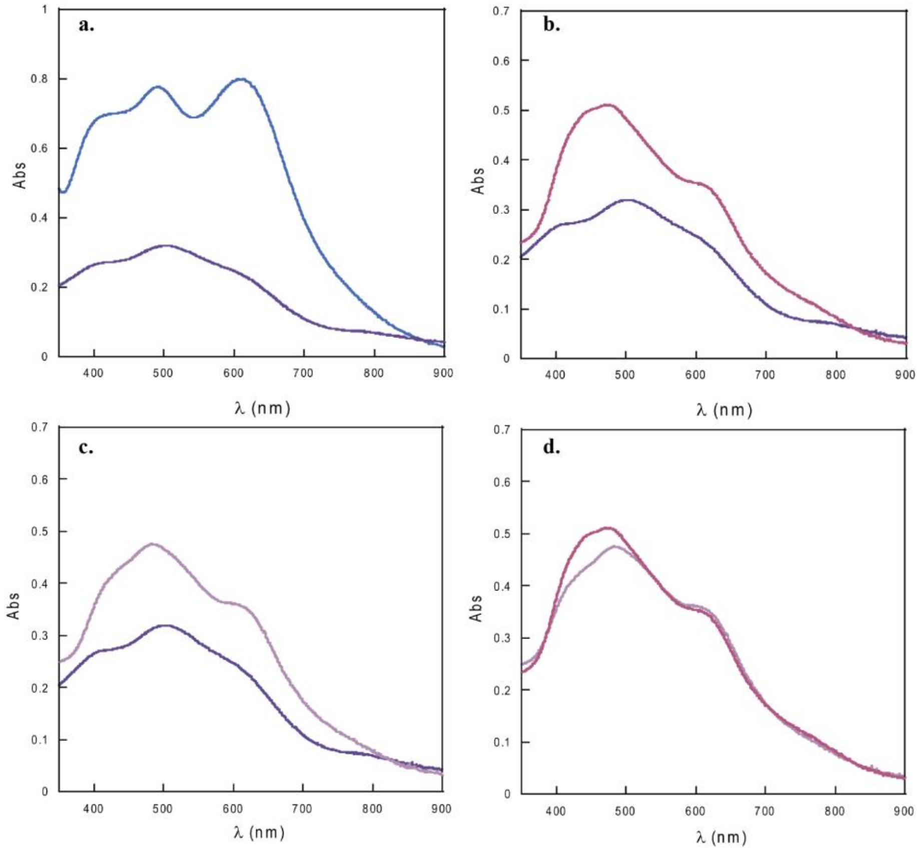

Figure 2-10. UV-vis in benzene of a)blue:[Re(O)(ap)$_2$]- and purple: [Re(O)(OCPh$_3$)(ap)(isq)]. b)magenta: [Re$_2$(μ-O)$_2$(ap)$_2$(isq)$_2$] and purple: [Re(O)(OCPh$_3$)(ap)(isq)]. c)light purple: [Re(O)(OCPh$_3$)(ap)(isq)] + Gomberg dimer and purple: [Re(O)(OCPh$_3$)(ap)(isq)] d) magenta: [Re$_2$(μ-O)$_2$(ap)$_2$(isq)$_2$] and light purple: [Re(O)(OCPh$_3$)(ap)(isq)] + Gomberg dimer

Addition of a weak H-atom donor, in the form of 0.5 equiv DHA or 1,4-cyclohexadiene (CHD), to *in situ* generated [Re(O)(ap)(isq•)(OCPh$_3$)] in C$_6$H$_6$ resulted in quantitative conversion to [Re$_2$(μ-O)$_2$(ap)$_2$(isq•)$_2$] by UV–vis spectroscopy. The observed products and reaction stoichiometry suggest [Re(O)(ap)(isq•)(OCPh$_3$)] is a viable intermediate in the Ph$_3$C• oxidations by [Re(O)$_2$(ap)(isq•)], but the long lifetime of [Re(O)(ap)(isq•)(OCPh$_3$)] in only the [Ph$_3$C]$^+$ + [Re(O)$_2$(ap)$_2$]$^–$ reaction prompted us to reexamine the role of the Ph$_3$C• in the O-atom transfer reaction. In particular, structural similarities in the quinoid Gomberg dimer to DHA and CHD led us to postulate that it might also supply the necessary

H• for generation of Ph_3COH. A literature search revealed that the Gomberg dimer is known to transfer H• to peroxy radicals during radical chain autoxidation.[20] Consistent with this hypothesis, treating [Re(O)(ap)(isq•)($OCPh_3$)] with 1 equiv Gomberg dimer gave clean conversion to [Re_2(μ-O)$_2$(ap)$_2$(isq•)$_2$] (Scheme 2-3) Figure 2-10, suggesting the Gomberg dimer generates Ph_3COH by net H• transfer. Accordingly, the dual roles of Gomberg dimer in its reaction with [Re(O)$_2$(ap)(isq•)]—a source of Ph_3C• and a reductant to supply H• to cleave the Re–$OCPh_3$ bond—provides a rationale for the observed sub-stoichiometric yields of Ph_3COH (vide supra).

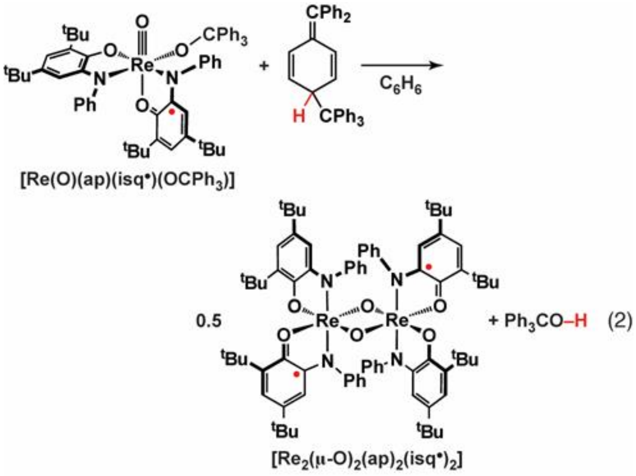

[Re(O)(ap)(isq•)(OCPh$_3$)]
C$_6$H$_6$
0.5
+ Ph$_3$CO–H
(2)
[Re$_2$(μ-O)$_2$(ap)$_2$(isq•)$_2$]

Scheme 2-3. Addition of Gomberg dimer to [Re(O)($OCPh_3$)(ap)(isq)]

2.3.3.5 Thermodynamics

The so-called "primary" oxo transfer reactivity collected in Figure 2-11 was previously used to bracket the Re–O_{oxo} bond dissociation enthalpy (BDE) in [Re(O)$_2$(ap)$_2$]– at 118 ± 15 kcal mol^{-1}. As shown in Figure 2-11b, [Re(O)$_2$(ap)(isq•)] is cleanly reduced by O-atom acceptors with X–O bond strengths greater than 87 kcal mol–1 (X = Me_2S), and reactions proceed in the reverse direction when the X–O bond strength is less than 72 kcal mol–1 (X

= C_5H_5N). However, formation of a μ-oxo bridge provides additional driving force in so-called "incomplete" oxo transfer reactions. Accordingly, the thermodynamics of O-atom removal from $[Re(O)_2(ap)(isq\bullet)]$ must account for the strength of the μ-oxo Re–ORe bond in $[Re_2(\mu\text{-}O)(O)_2(ap)_2(isq\bullet)_2]$. No spectroscopic evidence for dissociation of $[Re_2(\mu\text{-}O)(O)_2(ap)_2(isq\bullet)_2]$ was seen at temperatures up to 40 °C in CH_2Cl_2 or C_6H_6 solutions, suggesting this bond is relatively robust. Previously reported examples of incomplete oxo-transfer reactivity at $Cp^*Re(O)_2$ complexes reported μ-oxo Re–ORe bond strengths of 7-8 kcal mol^{-1}, and a geometrical model for the μ-oxo bridge in the binuclear $[Re_2(\mu\text{-}O)Cl_{10}]^{2-}$ ion estimates $\Delta H_{(Re–ORe)} \approx 40$ kcal mol^{-1} at a Re–O bond length of 1.9 Å. Accordingly, the range of $\Delta H_{(Re–ORe)}$ values introduces significant additional uncertainty into determination of the $Re–O_{oxo}$ BDE in $[Re(O)_2(ap)(isq\bullet)]$. A relatively strong μ-oxo Re–ORe bond of 40 kcal mol^{-1} gives 112 kcal $mol^{-1} < D_{(Re\equiv O)} < 127$ kcal mol^{-1}, or 120 ± 8 kcal mol^{-1}. A lower estimate for $\Delta H_{Re–ORe}$ returns a lower $D_{(Re\equiv O)}$. But unless the μ-oxo Re–ORe bond enthalpy is significantly less than 38 kcal mol^{-1}, no measurable thermodynamic weakening of the $Re–O_{oxo}$ bonds in $[Re(O)_2(ap)_2]^-$ is observed upon 1e– oxidation to $[Re(O)_2(ap)(isq\bullet)]$. Alongside the contracted $Re–O_{oxo}$ bond distance and increased $\nu_{(Re\equiv O)}$ frequency in the solid-state data (*vide supra*), it seems safest to assume that $D_{(Re\equiv O)}$ in $[Re(O)_2(ap)(isq\bullet)]$ is at least as strong, if not stronger, than in $[Re(O)_2(ap)_2]^-$.

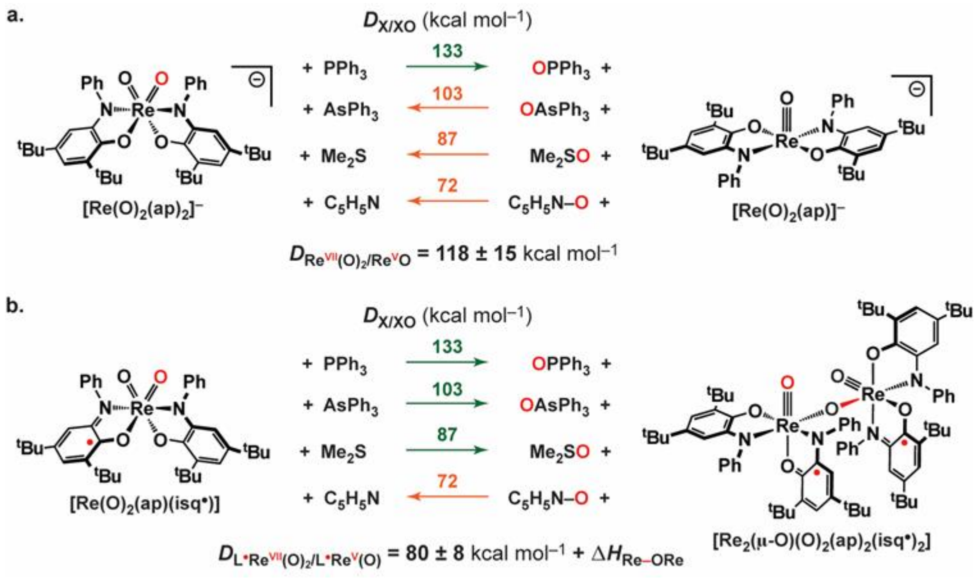
a.
$D_{X/XO}$ (kcal mol−1)
+ PPh3 133 OPPh3 +
+ AsPh3 103 OAsPh3 +
+ Me2S 87 Me2SO +
+ C5H5N 72 C5H5N–O +
[Re(O)2(ap)2]−
[Re(O)2(ap)]−
$D_{Re^{VII}(O)_2/Re^{V}O}$ = 118 ± 15 kcal mol−1
b.
$D_{X/XO}$ (kcal mol−1)
+ PPh3 133 OPPh3 +
+ AsPh3 103 OAsPh3 +
+ Me2S 87 Me2SO +
+ C5H5N 72 C5H5N–O +
[Re(O)2(ap)(isq•)]
[Re2(μ-O)(O)2(ap)2(isq•)2]
$D_{L^{\bullet}Re^{VII}(O)_2/L^{\bullet}Re^{V}(O)}$ = 80 ± 8 kcal mol−1 + ΔH_{Re-ORe}

Figure 2-11. Estimated Re–O$_{oxo}$ bond strengths in (a) [Re(O)$_2$(ap)$_2$]$^-$ and (b) [Re(O)$_2$(ap)(isq•)] from thermodynamic oxo transfer reactivity with substrates containing known X/XO bond dissociation energies (DX/XO).

2.4 Discussion

2.4.1 Are [Re(O)$_2$(ap)(isq•)] and [Re$_2$(μ-O)(O)$_2$(ap)$_2$(isq•)$_2$] oxyl radicals?

The two new Re complexes reported herein meet all the masked oxyl design criteria in Figure 2-1b. However, differences in the symmetries and oxidation states in [Re(O)$_2$(ap)(isq•)] and [Re2(μ-O)(O)$_2$(ap)$_2$(isq•)$_2$] lead to significantly altered ground state electronic structures and spin distributions, which in turn impact their oxidizing power and propensity to undergo RC-type bond formation at the terminal oxo ligands.

The quasi-octahedral [Re(O)(ap)(isq•)(μ-O)] fragments that make up the [Re$_2$(μ-O)(O)$_2$(ap)$_2$(isq•)$_2$] dimer are isoelectronic and isostructural with previously reported [Re(O)(ap)(isq•)(X)] species (X = Cl–, OAr–). In all, the C1 symmetry of the monomeric units makes the oxo and aminophenol ligands inequivalent, and the structural data suggest the unpaired spins localize on the ligands trans to the terminal oxo groups. This preference likely reflects the strong trans influence of the oxo and the weaker σ basicity of the monoanionic $[\text{isq}\bullet]^{-}$ as compared to $[\text{ap}]^{2-}$. This geometric preference also makes the $[\text{Re(O)(ap)(isq}\bullet\text{)(X)}]$ species diamagnetic. The $[\text{isq}\bullet]^{-}$ SOMO contains an in-phase combination of O and N p orbitals that are capable of mixing with π-symmetry metal d orbitals. Accordingly, a π interaction facilitates antiferromagnetic coupling between the $[\text{isq}\bullet]^{-}$ radical and the singly occupied d_{xy} orbital on Re, yielding an S=0 ground state. Formulation of the μ-oxo dimer as $[\text{Re}_2(\mu\text{-O})(\text{O})_2(\text{ap})2(\text{isq}\bullet)_2]$ implies four total spins: two d^1 Re(VI) centers and two $[\text{isq}\bullet]^{-}$ ligands, and the μ-oxo bridge introduces additional complexity. In particular, π-donation from the μ-oxo bridge can provide a pathway for electronic communication between $[\text{Re(O)(ap)(isq}\bullet)(\mu\text{-O})]$ fragments. Such cross-bridge dπ–pπ–dπ orbital mixing has been thoroughly examined in structurally similar "blue dimer" Ru water oxidation catalysts, where the strength of the electronic coupling is highly sensitive to structural deformations about the μ-oxo bridge. It is not readily apparent if, or to what extent, electronic coupling between the Re centers in $[\text{Re}_2(\mu\text{-O})(\text{O})_2(\text{ap})_2(\text{isq}\bullet)_2]$ is occurring. If each $[\text{Re(O)(ap)(isq}\bullet)(\mu\text{-O})]$ fragment is diamagnetic, coupling between Re centers is not a prerequisite for the observed S=0 ground state. A complete description of the magnetism in $[\text{Re}_2(\mu\text{-O})(\text{O})_2(\text{ap})_2(\text{isq}\bullet)_2]$ will require spectroscopic and magnetic measurements beyond the scope of this report.

1e– oxidation of $[\text{Re(O)}_2(\text{ap})_2]$– affords an S=1/2 monomer. Formulation as $[\text{Re(O)}_2(\text{ap})(\text{isq}\bullet)]$ emphasizes the aminophenol ligand-centered oxidation, but this is undoubtedly an oversimplification. First, in C_2 symmetry the aminophenol-derived ligands are equivalent, and strong through-bond coupling via the Re π orbitals should mediate ligand-to-ligand charge transfer (LLCT) that makes the aminophenol ligands electronically equivalent. Indeed, the computed structure suggests the majority of the spin is distributed equally across both aminophenol ligands, equivalent to a Robin-Day class IIII mixed valence compound. The masked oxyl strategy proposed in Figure 1b, invokes intramolecular charge transfer to introduce a low energy hole on a formally closed-shell oxo ligand. Accordingly, generation of a $[Re(O•)(O)(ap)_2]$ redox isomer occurs by an LLCT transition from $[O]^{2–}$ to $[isq•]^{–}$. Given the redox potentials of the ligands, this should be an electronically excited state, and indeed, there is no structural evidence to support formulation of the monomer as $[Re(O•)(O)(ap)_2]$. But the observation of significant spin density on the oxo ligands in the ground state of $[Re(O)_2(ap)(isq•)]$ in Figure 2-7 suggests that complete transfer of the hole to the oxido ligand may not be a prerequisite to accessing oxyl reactivity. In this respect, a more straightforward, and perhaps more relevant, description invokes significant covalency in the π bonding, wherein delocalization of the unpaired spin in the ground state is a natural consequence of partial occupancy of a single MO with significant contributions from the $[ap]^{2–}/[isq•]^{–}$, $[O]^{2–}$, and Re π-symmetry orbitals. Accordingly, the non-zero spin on the oxo ligand in $[Re(O)_2(ap)(isq•)]$ in the ground state, along with its steric accessibility, suggests that radical coupling at oxo might be viable, as demonstrated by its reactivity with $Ph_3C•$.

2.4.2 C-O bond formation and Ph_3COH production

Three plausible mechanisms for C–O bond formation from $Ph_3C•$ and $[Re(O)_2(ap)(isq•)]$ are illustrated in Scheme 2-2 (a-c). Mechanism a of initial ET to generate $[Ph_3C]^+$ and $[Re(O)_2(ap)_2]^–$ is uphill by only ~14 mV in CH_3CN, as estimated by the independently measured $E_{1/2}$ values for $[CPh_3]^{+/0}$ = –0.11 V and $[Re(O)_2(ap)(isq•)]/[Re(O)_2(ap)_2]^–$ = –

0.125 V vs. $Fc^{+/0}$ in MeCN. Facile C–O bond formation from these intermediates was independently demonstrated via reactions of isolated $[Ph_3C]^+$ with $[Re(O)_2(ap)_2]^-$ (vide supra). However, the observed reaction rates argue against this pathway being operative. In particular, for the comparatively slow reaction of Ph_3C• + $[Re(O)_2(ap)(isq•)]$ to occur by the two-step ET mechanism a in Scheme 2-2, the relatively rapid reaction of $[Ph_3C]^+$ + $[Re(O)_2(ap)_2]$– would necessarily be preceded by slow, rate-determining ET. It is unclear why outer-sphere ET would be slow under these conditions. As noted above, electrochemical measurements suggest the initial ET step in mechanism a is approximately thermoneutral, and combinations of $[Ph_3C]^+$ + $[Re(O)_2(ap)_2]^-$ do not give back ET to Ph_3C• + $[Re(O)_2(ap)(isq•)]$, which would be readily apparent by UV–vis spectroscopy. A large kinetic barrier for the ET step in mechanism a would require slow ET self-exchange from at least one of the $[Ph_3C]^+/Ph_3C$• or $[Re(O)_2(ap)(isq•)]/[Re(O)_2(ap)_2]^-$ redox pairs. These were not measured, but no experimental data collected to date suggest either redox interconversion is atypically slow or occurs with significant inner-sphere reorganization. An alternative mechanism c of initial ET to generate $[Ph_3C]^-$ and $[Re(O)_2(isq)_2]^+$ is thermodynamically prohibitive. The ET step is uphill by at least 1 V; $[Re(O)_2(ap)(isq•)]$ is not reducing—no evidence for $[Re(O)(isq•)_2]^+$ is observed up to potentials >1.50 V vs. $Fc^{+/0}$.

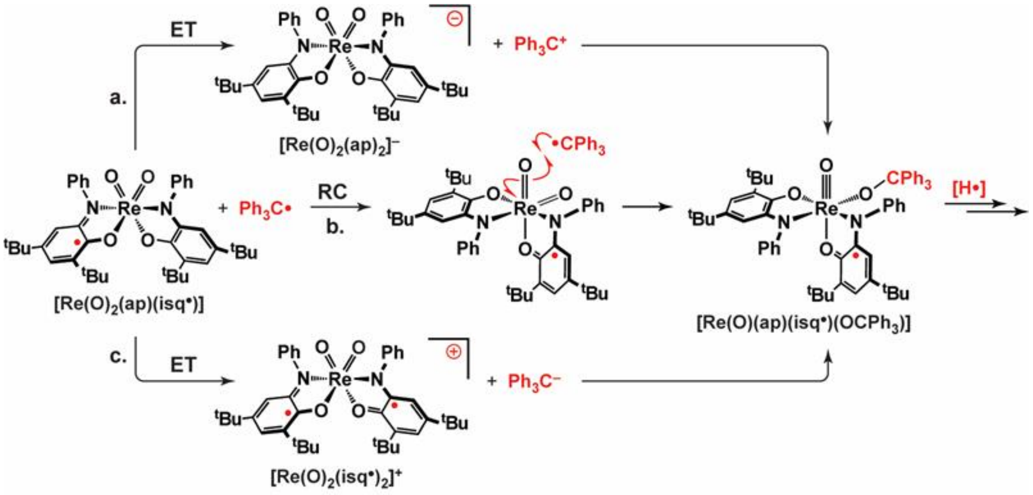

Scheme 2-4. Electron transfer and radical couple mechanisms for reaction of $[Re(O)_2(ap)(isq•)]$ and trityl

Eliminating both ET mechanisms leaves the RC-type direct attack mechanism b as the most likely mechanism for C–O bond formation from $Ph_3C•$ and $[Re(O)_2(ap)(isq•)]$. Although radical additions to an oxo ligand do not require unpaired spin at oxygen, radical trapping is a hallmark of $Ph_3C•$ reactivity, as exemplified by its well-known reactions with O_2 and I•. The extent to which RC-type C–O bond formation here reflects radical density at the oxo ligand is discussed below.

We previously attributed the apparent instability of the Re–$OCPh_3$ alkoxide linkage to unfavorable sterics and/or "adventitious H•". But the observation of long-lived $[Re(O)(ap)(isq•)(OCAr_3)]$ species implies the Re–$OCAr_3$ bond is not inherently unstable, and Re–$OCPh_3$ homolysis can be ruled out by the absence of rearrangement products deriving from triphenylmethoxyl Ph3CO• radical. Because free $Ph_3CO•$ is not an intermediate in Ph_3COH production from $[Re(O)_2(ap)(isq•)]$ + $Ph_3C•$, H• addition occurs prior to, or concomitant with, Re–O bond cleavage. In this respect, the absence of observable $[Re(O)(ap)(isq•)(OCPh_3)]$ in reactions with $Ph_3C•$ reflects the capacity of the

Gomberg dimer to rapidly deliver H• to an intact Re–OCPh$_3$ bond following rate-limiting radical C–O bond formation. Generation of Ph$_3$COH via treatment of independently prepared [Re(O)(ap)(isq•)(OCPh$_3$)] with other H• sources demonstrates that the proposed two-step mechanism is a viable route to Ph$_3$COH. How the H-atom is delivered, however, is unknown. Addition of H• to the oxo in [Re(O)(ap)(isq•)(OCPh$_3$)] to generate a [Re(OCPh$_3$)(OH)] complex followed by elimination via a four-center transition state is plausible, but the analogous reactivity of a previously reported [Re(OCPh$_3$)Cl] complex, and Ph$_3$C• hydroxylation by [Re$_2$(μ-O)(O)$_2$(ap)$_2$(isq•)$_2$], suggests an intramolecular pathway isn't a prerequisite for the observed reactivity.

The direct attack mechanism b resembles the canonical "hydroxyl rebound" mechanism for C–H hydroxylation, with two key differences: (i) the order of the bond forming steps is reversed, so radical O–C bond formation precedes formation of the O–H bond; (ii) the R• and H• for O–R and O–H bond formation derive from separate reagents rather than a single C–H bond. In this context, the capacity of [Re(O)$_2$(ap)(isq•)] to engage in classic rebound-type hydroxylations merits additional consideration. Initial H• transfer to form an unobserved [Re(O)(ap)(isq•)(OH)] transient cannot be ruled out, but independent experiments to probe H• transfer to [Re(O)$_2$(ap)(isq•)] gave significant quantities of H_2O without any observed intermediates, suggesting addition of a second H• to [Re(O)(ap)(isq•)(OH)] is fast. Accordingly, for Ph$_3$COH to form by initial H• addition at [Re(O)$_2$(ap)(isq•)] the putative [Re(O)(ap)(isq•)(OH)] intermediate would have to be rapidly intercepted by Ph$_3$C•, which is in low concentration relative to the Gomberg dimer that is the source of H•. Furthermore, [Re(O)$_2$(ap)(isq•)] shows little apparent propensity for O-atom transfer to weak benzylic C–H bonds. For instance, $[Re(O)_2(ap)(isq•)]$ is indefinitely stable in toluene up to 45 °C.

O-atom transfer from $[Re(O)_2(ap)(isq•)]$ or $[Re_2(\mu\text{-}O)(O)_2(ap)2(isq•)_2]$ to $Ph_3C•$ functionally mimics our prior report of Ph_3COH formation from $Ph_3C•$ + [Re(O)(ap)(isq•)Cl], suggesting that direct radical Ph3C• trapping is a general feature of this class of complexes. Observation of an alkoxide $[Re(O)(ap)(isq•)(OCPh_3)]$ intermediate here provides direct evidence for R• trapping at a formally closed-shell oxido ligand, a reaction with some precedent. The role of $[isq•]^–$ unpaired spin in bringing about this RC-type reactivity is discussed below.

2.4.3 Thermodynamic vs. kinetic effects on oxyl O-atom transfer

$[Re(O)_2(ap)(isq•)]$ hydroxylates trityl $Ph_3C•$; $[Re(O)_2(ap)_2]^–$ does not. Potential thermodynamic and kinetic contributors to this disparity are considered in turn.

$[Re(O)_2(ap)(isq•)]$ is necessarily a stronger 1e– oxidant than $[Re(O)_2(ap)2]^–$ —it is obtained by oxidation of d^0 metal complex—but neither is a strong outer-sphere oxidant. $[Re(O)_2(ap)(isq•)]$ is produced at a potential +125 mV above Fc^+. The stability of $[Re(O)_2(ap)(isq•)]$ in solvents with relatively weak benzylic C–H bonds (cf. toluene) suggests the H-atom accepting power of $[Re(O)_2(ap)(isq•)]$ is modest at best, implying $[Re(O)_2(ap)_2]^–$ is also a weak base. Because oxidation of an $[O]^{2–}$ ligand to an $[O•]^–$ radical formally reduces the net Re–O bond order by 0.5, significant weakening or lengthening of the $Re–O_{oxo}$ bonds in $[Re(O)_2(ap)(isq•)]$ could be evidence of oxyl character. Rather, the $Re–O_{oxo}$ bond distances are contracted by an average of 0.01 Å upon oxidation of $[Re(O)_2(ap)_2]^–$ to $[Re(O)_2(ap)(isq•)]$, and FTIR spectroscopy data suggest enhanced Re–O bonding in the oxidized congener. Neither are thermodynamically strong O-atom donors. Both are reduced by PPh_3. $[Re(O)_2(ap)(isq•)]$ transfers an O-atom to thermodynamically weaker oxo acceptors, including $AsPh_3$ and Me_2S, but this likely reflects formation of a μ-oxo bridge in $[Re_2(\mu\text{-}O)(O)_2(ap)2(isq•)_2]$, which provides additional driving force for the net O-atom transfer. Accordingly, it seems most likely that $[Re(O)_2(ap)(isq•)]$ is an intrinsically weaker thermodynamic O-atom donor than $[Re(O)_2(ap)_2]^-$.

The capacity of Gomberg's dimer to also supply the H• necessary for formation of Ph_3COH makes $Ph_3C•$ a reasonably strong O-atom acceptor. Yet O-atom transfer to $Ph_3C•$ has, to our knowledge, little precedent in the extensive literature for transition metal oxo transfer reactions. For comparison, $[Re(O)_2(ap)_2]^-$ is structurally homologous with $[Re(O)_2(ap)(isq•)]$, and seemingly an intrinsically stronger O-atom donor, but it cannot effect this transformation. We posit the paucity of metal-mediated interconversions of $Ph_3C•/Ph_3CO•$ reflects a kinetic rather than thermodynamic bias.

The well-established reactivity of $Ph_3C•$ with O_2 or I_2 is typically ascribed to facile bond formation between open-shell radicals, for instance via chain autoxidation. It is tempting to draw parallels between the RC-type C–O/I bond forming reactions and C–O bond formation at the oxo ligands in the $[Re(O)_2(ap)(isq•)]/[Re(O)(ap)(isq•)(X)]$ masked oxyl complexes. Our initial attempt to correlate the effects of radical distribution on the coupling reactivity were challenged by the fact that the [Re(O)(ap)(isq•)(X)] complexes are not free radicals. Although they are appropriately described as diradicals, with 1e– in a rhenium d orbital and 1e– on a redox-active $[isq^{Ph}]^{•-}$ ligand, the complexes are S=0 because the metal and ligand electrons are antiferromagnetically coupled. It has been argued that the experimental data are also consistent with a closed-shell $Re^{VII}(O)(ap)_2X$ formulation, wherein the observed bonding patterns arise from strong [ap^{Ph}]$^{2-}$ ligand-to-metal π-backdonation. We reasoned that oxidations of d^0 oxometal complexes would address this ambiguity.

The S=1/2 [Re(O)$_2$(ap)(isq•)] contains a single ligand-centered unpaired electron. It cleanly converts Ph$_3$C• to Ph$_3$COH, even at very low effective concentrations of Ph3C•. Qualitatively, [Re(O)$_2$(ap)(isq•)] is significantly more reactive than the S=0 masked oxyls. Stoichiometric reactions of Ph$_3$C• with [Re(O)$_2$(ap)(isq•)] are complete in hours at 25 °C vs. ~1 week for [Re(O)(ap)(isq•)Cl]. Treatment of [Re(O)$_2$(ap)(isq•)] with excess Ph$_3$C• gives clean conversion to the bis(μ-oxo) complex [Re$_2$(μ-O)$_2$(ap)$_2$(isq•)$_2$] without accumulation of [Re$_2$(μ-O)(O)$_2$(ap)$_2$(isq•)$_2$]. This is ascribed to rapid dimerization of [Re(O)(ap)(isq•)] that outcompetes deoxygenation of [Re$_2$(μ-O)(O)$_2$(ap)$_2$(isq•)$_2$] by Ph$_3$C•, implying the rate of Ph$_3$C• consumption by [Re(O)$_2$(ap)(isq•)] is significantly faster than [Re$_2$(μ-O)(O)$_2$(ap)2(isq•)$_2$]. In aggregate, RC-type C–O bond formation by Ph$_3$C• trapping is significantly accelerated in the oxorhenium complex with the most unpaired spin, and structural homologs without an [isq•]$^-$ radical are inert to Ph$_3$C•.

The accelerated degradation reactivity in ambient or low-energy light (*vide supra*), and enhanced stability in the dark, hints at enhanced reactivity from a low-energy excited-state. But the observation of dark reactivity with Ph$_3$C• implies the [Re(O)$_2$(ap)(isq•)] radical is kinetically reactive without the additional driving force afforded by photolysis or thermal access to an excited state. Rather, the observed RC-type C–O bond forming reactivity arises from unpaired spin in the ground state, which permits the net 2e– oxo transfer to Ph$_3$C• to occur via kinetically facile radical steps.

2.5 Conclusions

Prior efforts to correlate the effects of radical spin density on reactivity in monomeric [Re(O)(ap)(isq•)(X)] complexes were challenged by the absence of unpaired electrons in the S=0 ground states. And coordinatively unsaturated S=1/2 masked oxyl monomers, such as five-coordinate [Re(O)(ap)(isq•)], were compromised by radical additions at the Re centers. Isolation of [Re(O)$_2$(ap)(isq•)] from [Re(O)$_2$(ap)$_2$]$^-$ addresses both of those issues and provides an isostructural comparison of the effects of unpaired spin on RC-type reactivity at a terminal oxo ligand. Facile addition of Ph$_3$C• to [Re(O)(ap)(isq•)] is not rationalized by the type of thermodynamic analysis that often predicts metal-mediated oxo-transfer reactivity in closed-shell species, including [Re(O)$_2$(ap)$_2$]$^-$, and nothing in the solid state structural or spectroscopic data suggests that the Re–O$_{oxo}$ bonds in [Re(O)$_2$(ap)(isq•)] are thermodynamically activated for O-atom transfer. Rather, the propensity of [Re(O)(ap)(isq•)] to undergo direct RC-type C–O bond formation with Ph$_3$C• is apparently kinetic in origin.

This report adds two additional oxorhenium species that satisfy the masked oxyl design criteria. In aggregate, the data make a persuasive case that these design principles are transferrable and elicit reactivity that is atypical of traditional closed-shell oxo–metal complexes. All of the masked rhenium oxyls with [isq•]$^-$ ligand radicals are prone to radical C–O bond formation at a terminal oxo ligand. Close structural analogs without the ligand radical are inert.

It is now well established that unpaired spin at oxygen is not a prerequisite for radical addition to an oxido ligand, but a growing body of work suggests that radical density at a ligand gives access to kinetically facile bond-making steps that are inaccessible at closed-shell ligands. In this context, it is often difficult to parse the thermodynamic and kinetic contributions to the radical reactivity. For instance, excited state oxyl radicals such as the Ti^{III}–O• transients generated by photoexcitation titanosilicates have the thermodynamic bias baked-in vs. their closed-shell Ti^{IV}=O precursors. Notably, the radical additions described here occur in the dark. Accordingly, the masked rhenium oxyls demonstrate a kinetic bias for radical coupling without additional thermodynamic driving force. The sum of the data herein make a compelling case that this reactivity is a result of oxyl radical character in the ground electronic state, which arises from facile intraligand communication through the π-symmetry molecular orbitals. Accordingly, the masked oxyl design principles are transferrable to entirely different classes of redox-active ligand complexes, opening avenues to pursue thermodynamically stable oxidants that are kinetically activated for selective odd-electron bond-making and -breaking redox reactions. Successes in utilizing these principles for aerobic oxidation catalysis will be the subject of a future report.

2.6 Experimental details

2.6.1 General considerations

All manipulations were performed under anaerobic conditions using standard vacuum-line techniques or in an inert-atmosphere glovebox under purified nitrogen unless specified otherwise. Routine NMR spectra were acquired on a Varian Mercury 300 spectrometer (300.323 MHz for ^{1}H) at ambient temperature. All chemical shifts are reported in parts per million (ppm) relative to TMS, with the residual solvent peak serving as an internal reference.[21] Solution magnetic moments were obtained by Evan's NMR method,[22-23] and are reported as the average of three independent measurements, unless otherwise specified. UV–visible absorption spectra were acquired using a Varian Cary 50 spectrophotometer. Unless otherwise noted, all electronic absorption spectra were recorded at 25 ºC in 1 cm quartz cells. IR spectra were obtained by attenuated total reflectance (ATR) through a diamond plate on a Bruker Optics Alpha-P Fourier transform infrared (FTIR) spectrometer. All mass spectra were recorded in the Georgia Institute of Technology Bioanalytical Mass Spectrometry Facility. Matrix-assisted laser desorption/ionization mass spectra (MALDI–MS) were obtained using an Applied Biosystems 4700 proteomics analyzer. Electrospray ionization mass spectrometry (ESI–MS) was carried out with acetonitrile solutions using a Micromass Quattro LC spectrometer. Electron impact mass spectra (EI–MS) were obtained using a VG instruments model 70-SE spectrometer. Gas chromatography mass spectrometry (GC–MS) analyses used an Agilent 6890 gas chromatograph equipped with an autosampler and a Restek Rxi-5 ms column (30 m × 0.25 mm i.d., 0.25 μm film thickness). Injections of 1 μL were made at a 50:1 split ratio. The GC oven program consisted of a hold at 30 ºC for 1 min, followed by a 15 ºC/min ramp to 300 ºC, and then a hold at 300 ºC for 11 min. The mass spectrometer used in tandem was a Micromass AutoSpec electronionization (EI) detector. For GC–MS quantification of organics, n-decane (1 μL) was added to serve as an internal standard and product yields were determined by a comparison of the EI–MS detector responses against calibration curves derived from the pure materials, as well as by a comparison to the detector response for n-decane. Gas chromatography with flame ionization detection (GC–FID) analyses were performed using a Shimadzu GC-2010 Gas Chromatograph equipped with Restek SHRXI-

5MS column (15 m × 0.25 mm i.d., 0.25 μm film thickness). Injections of 1 μL were made at a 1:30 split ratio with the nitrogen carrier gas flow rate of 24.4 mL/min. Conditions of the GC are as follows: injector temperature, 350 ºC; column starting temperature, 40 ºC; column ramp, 250 ºC at 25 ºC/min; final column hold, 250 ºC for 2 min. Cyclic voltammetry experiments were performed inside an N2-filled glove box in MeCN or CH2Cl2 with 0.1 M $[nBu_4N][PF_6]$ as the supporting electrolyte, unless otherwise noted. The voltammograms were recorded with a CH Instruments 620C potentiostat, using a 2.5 mm (O.D) 1.0 mm (I.D.) Pt disk working electrode, Ag wire quasi-reference electrode, and a Pt wire auxiliary electrode, at a scan rate of 0.1 V s–1, unless reported otherwise. Reported potentials are referenced to the ferrocenium/ferrocene (Fc+/Fc) redox couple, added as an internal standard at the conclusion of each experiment. Elemental analyses were performed by Atlantic Microlab, Inc., Norcross, GA. All analyses were performed in duplicate, and the reported compositions are the average of the two runs.

2.6.2 Methods and materials

Anhydrous acetonitrile (MeCN), dichloromethane, tetrahydrofuran (THF), and pentane solvents for air- and moisture- sensitive manipulations were purchased from Sigma-Aldrich and further dried by passage through columns of activated alumina, degassed by at least three freeze–pump–thaw cycles, and stored under N_2 prior to use. Deuterated solvents and ^{18}O water were purchased from Cambridge Isotope Laboratories. Benzene (99.8%) was purchased from Alfa Aesar and stored under N2. $(Et_4N)[Re^{VII}(O)_2(ap^{Ph})2]$[24] and triphenylmethyl radical Ph_3C• dimer[25] in C_6H_6 were prepared by literature methods. All characterization data matched those referenced. All other reagents were purchased from Sigma-Aldrich or Alfa Aesar and used as received.

2.6.3 Synthesis of $(Et_4N)[Re(^{16/18}O)_2(ap)_2]$

A 100 mL round bottom flask was charged with $(Et_4N)[Re^{V}(O)(ap^{Ph})_2]$ (120 mg, 0.130 mmol) and 40 mL of dry, degassed MeCN. $^{18}OH_2$ (200 μL) was added and stirred vigorously for 2 days. The solution was exposed to air with continued stirring, and a color change from moss green to navy blue was observed over 24-48 h at ambient temperature. Concentration of the solution in vacuo afforded a dark blue precipitate, which was collected via filtration and dried to afford a mixture of $(Et_4N)[Re^{VII}(^{16}O)_2(apPh)_2]$, $(Et_4N)[Re^{VII}(^{18}O)(^{16}O)_2(ap^{Ph})_2]$ and $(Et_4N)[Re^{VII}(^{18}O)2(ap^{Ph})2]$ (0.029 mg, 0.031 mmol, 24%). ESI–MS (m/z): 811 [M]–.

2.6.4 Synthesis of $[Re(O)_2(ap)(isq)]$

A 20 mL scintillation vial was charged with $(Et_4N)[ReVII(O)_2(ap^{Ph})_2]$ (40 mg, 0.043 mmol) and 3 mL MeCN and stirred vigorously. Dropwise addition of 0.031 M ferrocenium hexafluorophosphate in MeCN (1.5 mL, 0.047 mmol) over 1 min gave a color change from navy blue to dark green, followed by precipitation of a dark solid over 1 hr. The solution was concentrated in vacuo and filtered to afford $Re^{VII}(O)_2(ap^{Ph})(isq^{Ph})$ (30 mg, 0.037 mmol, 84%) as a dark green waxy solid. Oxidations performed with nitrosonium tetrafluoroborate or silver tetrafluoroborate gave the same product; ferrocenium was found to give the best yield. Crystalline solids suitable for single crystal X-ray diffraction were obtained by slow diffusion of pentane into a saturated toluene solution at –20 ºC. MALDI–MS (m/z): 809 [M]+. UV–vis (C_6H_6) λmax, nm (ε, M^{-1} cm^{-1}): 294 (16000), 410 (8500), 596 (6000), 846 (2000). FTIR (ATR, cm^{-1}): 2949 (m, b), 1487 (w), 1360 (w), 1251(m), 1148 (m), 1102 (m), 10227 (m), 911 (vs), 876 (vs), 773 (m), 739 (m), 703 (s), 651 (m), 582 (m), 493 (m).

Anal. Calcd. for $C_{40}H_{50}N_2O_4Re$: C, 59.38; H, 6.23; N, 3.46. Found: C, 59.31; H, 6.15; N, 3.52.

2.6.5 Synthesis of [$Re_2(\mu$-O)(O)$_2$(ap)$_2$(isq•)$_2$]

Method 1. A 20 mL scintillation vial was charged with (Et_4N)[Re^{VII}(O)$_2$(apPh)$_2$] (0.227 g, 0.242 mmol) and $AgBF_4$ (47 mg, 0.24 mmol). Addition of acetone (10 mL) afforded a dark purple solution. The reaction mixture was stirred for 15 h and the solvent was removed in vacuo to give a dark residue, which was extracted into ether and filtered to remove a white precipitate. The purple filtrate was dried in vacuo to give Re^{VI}_2(μ-O)(O)$_2$(ap^{Ph})$_2$(isq•)$_2$ (0.165 g, 0.103 mmol, 43%) as a purple powder. Single crystals for X-ray diffraction were obtained by slow evaporation of a CH_3CN solution at –20 ºC. Method 2. A 10 mL scintillation vial was charged with (Et_4N)[Re^{VII}(O)$_2$(ap^{Ph})$_2$] (100 mg, 0.106 mmol) and THF (2 mL) to afford a clear, dark blue solution. Addition of PPh_3 (14 mg, 0.053 mmol) in THF (1 mL) followed by dropwise addition of $AgBF_4$ (21 mg, 0.11 mmol) in THF (1 mL) and stirring for 15 h at ambient temperature yielded a turbid, darker purple solution. Filtration through a fritted funnel to remove Ag^0 and removal of the solvent gave a dark residue, which was taken up in pentane and passed through a 0.2 μm PTFE syringe filter to remove $OPPh_3$ solids. The filtrate was dried in vacuo to give a purple powder of Re^{VI}_2(μ-O)(O)$_2$(ap^{Ph})$_2$(isq•)$_2$ (80.1 mg, 0.0571 mmol, 94%). MALDI-MS (m/z): 1602 [M]+. UV–vis (C_6H_6) λmax, nm (ε, M–1 cm–1): 292 (25000), 430 (19000), 522 (19000), 792 (10000). FTIR (ATR, cm–1): 2951 (m, b), 1589 (v), 1483 (v), 1361 (v), 1239 (m), 1166 (m), 1119 (m), 996 (v), 910 (m), 753 (s), 721 (vs), 704 (vs), 623 (s), 540 (vs), 404 (m). Samples for combustion analysis were prepared by method 2, which produces $OPPh_3$ as a byproduct that can be carried through the purification steps. The reported analysis is for Re^{VI}_2(μ-

O)(O)$_2$(ap^{Ph})$_2$(isq•)$_2$•0.9OPPh$_3$. The presence of the OPPh$_3$ in the sample was confirmed by its diagnostic resonances in the ^{1}H NMR spectrum. Anal. Calcd for C96.2H113.5N4O7.9P0.9Re2: C, 62.37; H, 6.18; N, 3.02; Found: C, 62.10; H, 6.45; N, 2.66.

2.6.6 Reactions with triphenylmethyl radical

In a representative procedure, a C_6H_6 solution of 0.0247 M Re^{VII}(O)$_2$(ap^{Ph})(isq•) (2.00 mL, 0.0494 mmol) was mixed with 0.0933 M triphenylmethyl radical dimer in C_6H_6 (267 μL, 0.0247 mmol Ph_3C•) in a thick-walled flask equipped with a Kontes brand high-vacuum PTFE valve. The flask was sealed and stirred vigorously for 1 day. A 0.2 mL aliquot of the reaction solution was transferred to a 2 mL GC–MS glass vial under nitrogen, and 0.00513 M n-decane in benzene (5 μL, 2.6×10–5 mmol) was added as an internal standard. A 1 μL aliquot of this solution was then sampled by GC–FID and the Ph_3COH yield (0.0170 mmol, 69%) was determined by a comparison of the FID responses against calibration curves derived from the pure materials, as well as by comparison to the detector response for a control solution of Gomberg's dimer.

2.6.7 Computational studies

The initial coordinates for all structures were obtained from the crystallographic data. Density functional theory (DFT), geometry optimizations, and energy calculations were performed on unconstrained structures using the ORCA 4.0 software package.[26,27] Geometry optimizations and subsequent time-dependent DFT calculations were performed using Becke's three-parameter hybrid functional along with the Lee−Yang−Parr functional for correlation (B3LYP).[28,29] Ahlrich's polarized triple-ζ-valence def2-TZVP basis set with the def2/J auxiliary basis set[30] was used for H, C, N, O, P and Re atoms, and an effective core potential (ECP) was applied to Re atoms.[31] The RIJCOSX approximation, tight optimization, tight SCF, and slow field convergence were employed. The IboView program[32] was used for molecular graphics and analyses. Geometry optimizations were also performed with Becke's functional for exchange along with Perdew's functional for correlation (BP86);[33] however, these models displayed larger deviations from the experimental structures.

2.7 X-ray crystallography

2.7.1 [Re(O)(ap)(isq)]

Single crystals of $C_{40}H_{50}N_2O_4Re$ were recrystallized from slow diffusion of pentane into a concentrated toluene solution. A suitable crystal was selected and placed on a 'Bruker APEX-II CCD' diffractometer. The crystal was kept at 99.98 K during data collection. Using Olex2[34], the structure was solved with the XT[35] structure solution program using Intrinsic Phasing and refined with the XL[36] refinement package using Least Squares minimisation.

Crystal Data for $C_{40}H_{50}N_2O_4Re$ (M =759.12 g/mol): triclinic, space group P-1 (no. 2), a = 8.7919(9) Å, b = 11.2509(12) Å, c = 20.006(2) Å, α = 87.708(4)°, β = 82.298(4)°, γ = 71.599(4)°, V = 1860.8(3) Å3, Z = 2, T = 99.98 K, μ(MoKα) = 3.303 mm-1, Dcalc = 1.355 g/cm3, 14716 reflections measured (4.924° ≤ 2Θ ≤ 56.564°), 14716 unique (Rint = ?, Rsigma = 0.0748) which were used in all calculations. The final R1 was 0.0510 (I > 2σ(I)) and wR2 was 0.1025 (all data).

2.8 References

1. Yang, X.; Baik, M.-H., Electronic Structure of the Water-Oxidation Catalyst [(bpy)2(OHx)RuORu(OHy)(bpy)2]z+: Weak Coupling between the Metal Centers Is Preferred over Strong Coupling. *Journal of the American Chemical Society* **2004,** *126* (41), 13222-13223.

2. Yang, X.; Baik, M.-H., cis,cis-[(bpy)2RuVO]2O4+ Catalyzes Water Oxidation Formally via in Situ Generation of Radicaloid RuIV−O•. *Journal of the American Chemical Society* **2006,** *128* (23), 7476-7485.

3. Siegbahn, P. E. M.; Crabtree, R. H., Manganese Oxyl Radical Intermediates and O−O Bond Formation in Photosynthetic Oxygen Evolution and a Proposed Role for the Calcium Cofactor in Photosystem II. *Journal of the American Chemical Society* **1999,** *121* (1), 117-127.

4. Betley, T. A.; Wu, Q.; Van Voorhis, T.; Nocera, D. G., Electronic Design Criteria for O−O Bond Formation via Metal−Oxo Complexes. *Inorganic Chemistry* **2008,** *47* (6), 1849-1861.

5. Surendranath, Y.; Kanan, M. W.; Nocera, D. G., Mechanistic Studies of the Oxygen Evolution Reaction by a Cobalt-Phosphate Catalyst at Neutral pH. *Journal of the American Chemical Society* **2010,** *132* (46), 16501-16509.

6. Sameera, W. M. C.; McGrady, J. E., The role of substrate in unmasking oxyl character in oxomanganese complexes: the key to selectivity? *Dalton Transactions* **2008,** (44), 6141-6149.

7. Balcells, D.; Raynaud, C.; Crabtree, R. H.; Eisenstein, O., A Rational Basis for the Axial Ligand Effect in C−H Oxidation by [MnO(porphyrin)(X)]+ (X = H2O, OH−, O2−) from a DFT Study. *Inorganic Chemistry* **2008,** *47* (21), 10090-10099.

8. Herlihy, D. M.; Waegele, M. M.; Chen, X.; Pemmaraju, C. D.; Prendergast, D.; Cuk, T., Detecting the oxyl radical of photocatalytic water oxidation at an n-SrTiO3/aqueous interface through its subsurface vibration. *Nat Chem* **2016,** *8* (6), 549-555.

9. Ryan, M. F.; Fiedler, A.; Schroeder, D.; Schwarz, H., Radical-like Behavior of Manganese Oxide Cation in Its Gas-Phase Reactions with Dihydrogen and Alkanes. *Journal of the American Chemical Society* **1995,** *117* (7), 2033-2040.

10. Shiota, Y.; Yoshizawa, K., Methane-to-Methanol Conversion by First-Row Transition-Metal Oxide Ions: ScO^+, TiO^+ , VO^+ , CrO^+, MnO^+, FeO^+, CoO^+, NiO^+, and CuO^+. *Journal of the American Chemical Society* **2000,** *122* (49), 12317-12326.

11. Schröder, D.; Roithová, J., Low-Temperature Activation of Methane: It also Works Without a Transition Metal. *Angewandte Chemie International Edition* **2006,** *45* (34), 5705-5708.

12. Schroder, D.; Schwarz, H., Gas-phase activation of methane by ligated transition-metal cations. *Proceedings of the National Academy of Sciences* **2008,** *105* (47), 18114-18119.

13. Schwarz, H.; González-Navarrete, P.; Li, J.; Schlangen, M.; Sun, X.; Weiske, T.; Zhou, S., Unexpected Mechanistic Variants in the Thermal Gas-Phase Activation of Methane. *Organometallics* **2017,** *36* (1), 8-17.

14. Mayer, J. M., Understanding Hydrogen Atom Transfer: From Bond Strengths to Marcus Theory. *Accounts of Chemical Research* **2011,** *44* (1), 36-46.

15. Mayer, J. M., Hydrogen Atom Abstraction by Metal−Oxo Complexes: Understanding the Analogy with Organic Radical Reactions. *Accounts of Chemical Research* **1998,** *31* (8), 441-450.

16. Kobayashi, K.; Ohtsu, H.; Wada, T.; Kato, T.; Tanaka, K., Characterization of a Stable Ruthenium Complex with an Oxyl Radical. *Journal of the American Chemical Society* **2003,** *125* (22), 6729-6739.

17. Ballhausen, C. J.; Gray, H. B., The Electronic Structure of the Vanadyl Ion. *Inorganic Chemistry* **1962,** *1* (1), 111-122.

18. Brown, S. N., Metrical Oxidation States of 2-Amidophenoxide and Catecholate Ligands: Structural Signatures of Metal–Ligand π Bonding in Potentially Noninnocent Ligands. *Inorganic Chemistry* **2012,** *51* (3), 1251-1260.

19. Jeżowska-Trzebiatowska, B.; Hanuza, J.; Bałuka, M., Force constants and vibration frequencies of the rhenium-oxygen bonds in the infrared region (200–4000 cm−1). *Spectrochimica Acta Part A: Molecular Spectroscopy* **1971,** *27* (9), 1753-1772.

20. McBride, J. M., The hexaphenylethane riddle. *Tetrahedron* **1974,** *30* (14), 2009-2022.

21. Fulmer, G. R.; Miller, A. J. M.; Sherden, N. H.; Gottlieb, H. E.; Nudelman, A.; Stoltz, B. M.; Bercaw, J. E.; Goldberg, K. I., NMR Chemical Shifts of Trace Impurities: Common Laboratory Solvents, Organics, and Gases in Deuterated Solvents Relevant to the Organometallic Chemist. *Organometallics* **2010,** *29* (9), 2176-2179.

22. Piguet, C., Paramagnetic Susceptibility by NMR: The "Solvent Correction" Removed for Large Paramagnetic Molecules. *Journal of Chemical Education* **1997,** *74* (7), 815.

23. Evans, D. F., The Determination of the Paramagnetic Susceptibility of Substances in Solution by Nuclear Magnetic Resonance. *J Chem Soc* **1959,** (Jun), 2003-2005.

24. Lippert, C. A.; Hardcastle, K. I.; Soper, J. D., Harnessing Redox-Active Ligands for Low-Barrier Radical Addition at Oxorhenium Complexes. *Inorganic Chemistry* **2011,** *50* (20), 9864-9878.

25. Gomberg, M., AN INSTANCE OF TRIVALENT CARBON: TRIPHENYLMETHYL. *Journal of the American Chemical Society* **1900,** *22* (11), 757-771.

26. Neese, F. The ORCA Program System. *WIREs Comput. Mol. Sci.* **2012**, *2* (1), 73–78.

27. Neese, F.; Wennmohs, F.; Becker, U.; Riplinger, C. The ORCA Quantum Chemistry Program Package. *ET J.* **2020**, 19.

28. Becke, A. D. Density-functional Thermochemistry. III. The Role of Exact Exchange. **1993**, *98*, 6.

29. Lee, C.; Yang, W.; Parr, R. G. Development of the Colle-Salvetti Correlation-Energy Formula into a Functional of the Electron Density. *Phys Rev B* **1988**, *37* (2), 785–789.

30. Weigend, F. Accurate Coulomb-Fitting Basis Sets for H to Rn. *Phys Chem Chem Phys* **2006**, *8* (9), 1057–1065.

31. Andrae, D.; Häußermann, U.; Dolg, M.; Stoll, H.; Preuß, H. Energy-Adjustedab Initio Pseudopotentials for the Second and Third Row Transition Elements. *Theor. Chim. Acta* **1990**, *77* (2), 123–141.

32. Knizia, G.; Klein, J. E. M. N. Electron Flow in Reaction Mechanisms—Revealed from First Principles. *Angew. Chem. Int. Ed.* **2015**, *54* (18), 5518–5522.

33. Becke, A. D. Density-Functional Exchange-Energy Approximation with Correct Asymptotic Behavior. *Phys Rev A* **1988**, *38* (6), 3098–3100.

34. Dolomanov, O.V., Bourhis, L.J., Gildea, R.J, Howard, J.A.K. & Puschmann, H. (2009), J. Appl. Cryst. 42, 339-341.

35. Sheldrick, G.M. (2015). Acta Cryst. A71, 3-8.

36. Sheldrick, G.M. (2008). Acta Cryst. A64, 112-122.

CHAPTER 3. OXOVANADIUM COMPLEXES FOR AEROBIC ALCOHOL OXIDATION

3.1 Introduction

Schemes for conversion of lignin into fuels are all predicated on efficient methods for selective breaking of C–O, and C–C bonds and oxovanadium complexes have received increased attention over the past 10 years for their reactivity in this regard.[1-4] Salen-type ligands are ubiquitous in current oxovanadium chemistry and while they have the potential to be redox-active, this is not always taken advantage of. Interestingly, the complexes utilized by Toste[5] and Hanson[6] have shown divergent reactivity with lignin model compounds. In these reactions the Toste complex, shown in Figure 3-1, produced C–O bond breaking products while the Hanson one gave C–C bond cleavage products.[6,7] The Hanson structure shown in Figure 3-1 is active for aerobic alcohol oxidation.[8] The third structure in Figure 3-1 is active for the oxidative-reductive coupling of alcohols, the first reported for a vanadium-oxo. This reaction produces the aldehyde and C–C coupling of the reduced alkane.[9] This reactivity has particular relevance to that proposed for our oxovanadium complexes' reaction with alkoxides.

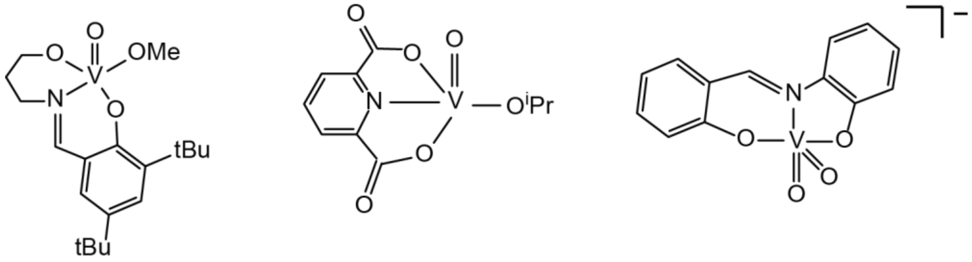

Toste Hanson Steffensmeier

Figure 3-1. Structure of oxovanadium(V) complexes

Aerobic alcohol oxidation is useful for the formation of aldehydes, ketones, and carboxylic acids and using oxygen as the oxidant is beneficial for economic and environmental reasons. Oxygen is more environmentally friendly than other oxidants like permanganate- and chromium-based ones. Hanson and coworkers have studied the mechanism of aerobic alcohol oxidation for a dipicolinate oxovanadium(V) complex (Figure 3-1) and sought to better understand the role of base in the reaction.[8] They also tried to determine whether a one- or two-electron pathway was operative in the oxidation. Vanadium complexes have been shown to undergo both types of reactivity. Understanding how structure and electronics play a role in this varying reactivity will allow us to tune our catalysts for the desired pathway and oxidation products.

We postulated that the use of a redox-active NHC ligand will let us tune the redox properties of the complex and modulate reactivity at the terminal oxo ligand thereby engendering differing reactivity based on ligand oxidation state. This would mirror the divergent reactivity seen with $[Re(O)_2(ap)_2]^-$ and $[Re(O)_2(ap)(isq\bullet)]$ in Chapter 2 of this work. Aside from changes to the NHC ligand, the lability of the ligand trans to the NHC will be important for substitution of the substrate and interaction with the terminal oxo ligand. And while aerobic alcohol oxidation is well studied for vanadium oxos, less is known about their capacity for DODH–like reactivity with both mono- and polyols.[10,11] Understanding this reactivity would allow us to develop better catalysts for the degradation of biomass and limit our need to rely on fossil fuels.

3.2 Results

3.2.1 Synthesis

Initial targets were vanadium analogs of the oxorhenium(V) complex, $[ReO(Ap^{Ph})_2]^{-}$, a precursor to the dioxo complexes discussed in the previous chapter.

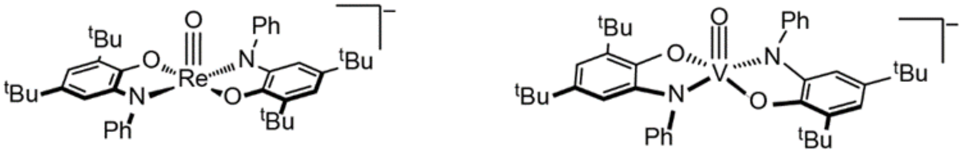

Figure 3-2. Oxorhenium(V) and its vanadium analog

The proposed synthetic route took advantage of the vanadium starting compound, $VO(OiPr)_3$, which acts as an internal base and the aminophenol ligand H_2Ap^{Ph}. Upon addition of the ligand to an MeCN solution of $VO(OiPr)_3$ a color change from colorless to dark blue was observed. This observed color change as well as the ^1H NMR matched that reported for $V(Ap^{Ph})_2(HAp^{Ph})$ by Chun and co-workers from the oxovanadium species, $VO(SO_4)\bullet 5H_2O$.[12] Formation of the tris homoleptic amidophenolate species was observed with limiting H_2Ap ligand, suggesting $V(Ap^{Ph})_2(HAp^{Ph})$ is the thermodynamic sink. The fate of the oxo ligand was not determined but is likely H_2O given the overall reaction stoichiometry.

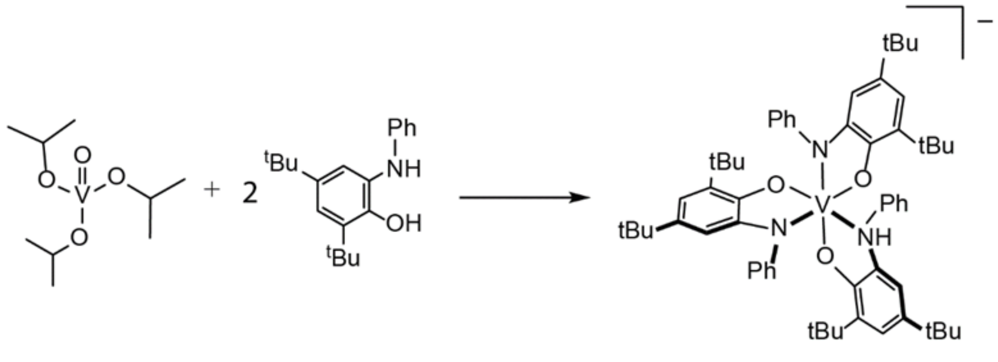

Figure 3-3. Synthesis of tris-homoleptic amidophenolate vanadium(V)

To prevent ligand redistribution, our focus shifted to a pincer-type bis(phenoxide) NHC, N,N′-bis(2-hydroxy-3,5-di-tert-butylphenyl)-4,5-dihydroimidazolinium chloride, (OCO), shown in Figure 3-4, ligand that had been shown to support low-coordinate complexes and recently demonstrated by our lab to undergo two ligand-centered oxidations. Its modular design also affords significant steric and electronic tunability. A previously reported VO(NHC) complex served as a convenient starting point for our studies.[13] This complex had the benefit of being easily accessible and opened the possibility to explore new applications of oxidations mediated by high-valent metal-oxos.

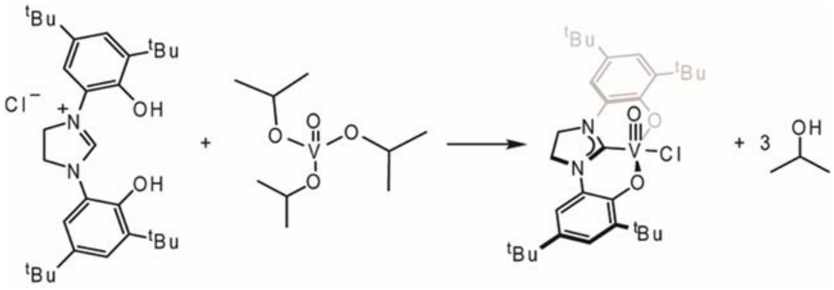

Figure 3-4. Synthesis of [V(O)(OCO)Cl]

3.2.2 Synthesis of [V(O)(OCO)OMe]

Dissolution of VO(OCO)Cl in methanol affords a slow color change from red to green and precipitation of a green powder over ca. 12 hours at 25°C. The ^{1}H NMR spectrum of the green powder in benzene shows small shifts relative to VO(OCO)Cl in the aryl region (7.84 and 6.42 ppm to 7.47 and 6.48 ppm) and in the t-butyl region (1.85 and 1.38ppm to 1.80 and 1.43 ppm) with a new peak at 5.05 ppm corresponding to bound methoxide. The resonance for the four hydrogens of the NHC backbone similarly shifts from 2.77 to 2.81 ppm, Figure 3-5 (green and red). It should also be noted that NMR solvent plays a significant role in the position of the NHC backbone resonances and their resolution. Figure 3-5 demonstrates this for $CDCl_3$ and C_6D_6.

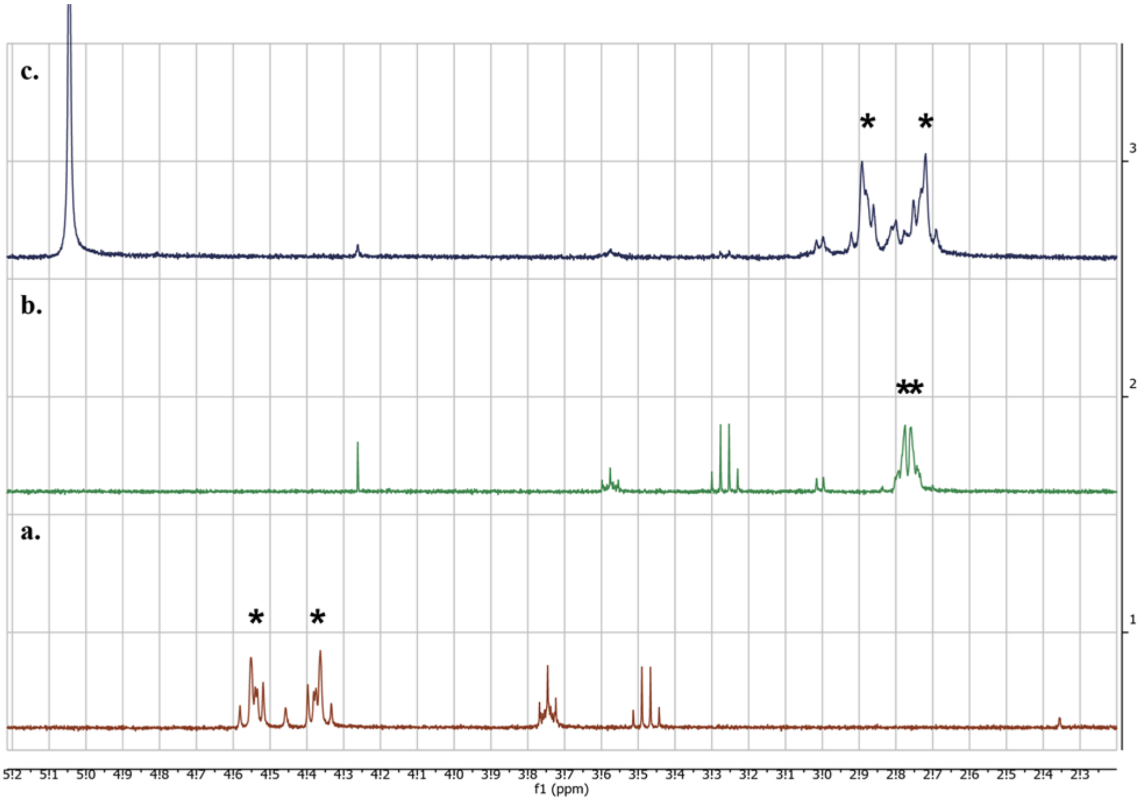

Figure 3-5. ^{1}H NMR of a) [V(O)(OCO)Cl] in $CDCl_3$, b) [V(O)(OCO)Cl] in C_6D_6, c) [V(O)(OCO)OMe] in C_6D_6. * denotes NHC backbone resonances.

Crystals suitable for x-ray diffraction were grown from the slow evaporation of a concentrated methanol solution.

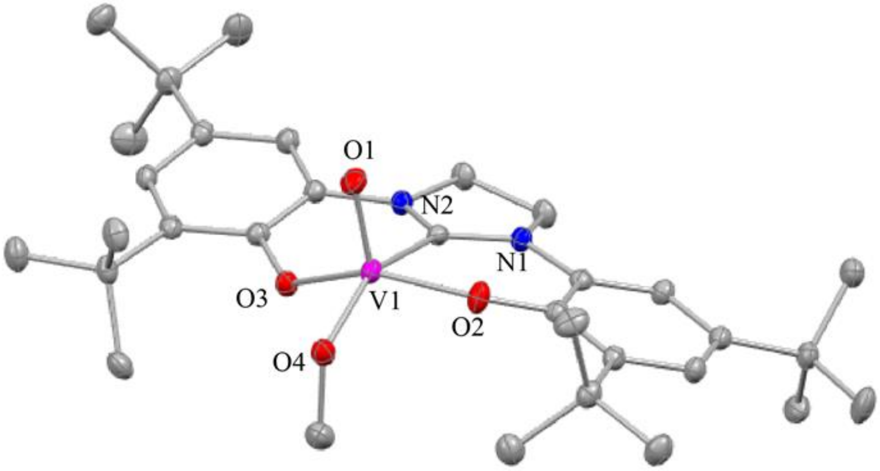

Figure 3-6. Crystal structure of [V(O)(OCO)OMe]. ORTEP ellipsoids at 50% probability with hydrogens omitted for clarity.

The putative methoxide complex is described as pseudo-square pyramidal, analogous to the previously reported chloride structure. The respective tau values being equal to 0.052 and 0.022 for the chloride and methoxide respectively. The average bond length around the aminophenol rings is close to 1.40Å showing no evidence of oxidation of either phenoxide arm to the iminosemiquinone form, therefore the OCO ligand in the methoxide complex is in the fully reduced, dianionic, state similar to what is seen in the chloride complex. This leads to an assignment of the vanadium center as d^0 vanadium(V).

Comparison of the methoxide structure to the previously reported chloride structure showed interesting structural differences with implications for reactivity. The length of the terminal vanadium oxygen bonds were not significantly different but the V–O in the chloride complex was slightly shorter than that in the methoxide. The bond metrics are shown in Table 3-1. Conversely, the bonds between the vanadium and the ancillary ligands, the carbon of the NHC and the oxygens of the phenoxide, do show small yet significant differences. These bonds follow the same pattern as the terminal oxygen bonds described above with the V–C bond being shortest in the chloride complex and longest in the methoxide complex.

Table 3-1. Selected bond lengths comparing [V(O)(OCO)Cl] and [V(O)(OCO)OMe]

Selected Bond Lengths(Å)		
Bonds	**VO(OCO)Cl**	**VO(OCO)OMe (this work)**
V=O (terminal)	1.588(3)	1.6003(18)
V–C (NHC)	2.095(3)	2.143(3)
V–O (phenoxide)	1.817(2)	1.8514(17)
V–O (phenoxide)	1.810(2)	1.8631(18)
V–X (X= Cl, OMe)	2.308(1)	1.8224(18)

Given the ^{1}H NMR and crystal structure data, we formulate this new complex as VO(OCO)OMe. Conversion of (OCO)V(O)Cl to (OCO)V(O)OMe is balanced by loss of HCl, as shown in Scheme X and dealt with in a later section.

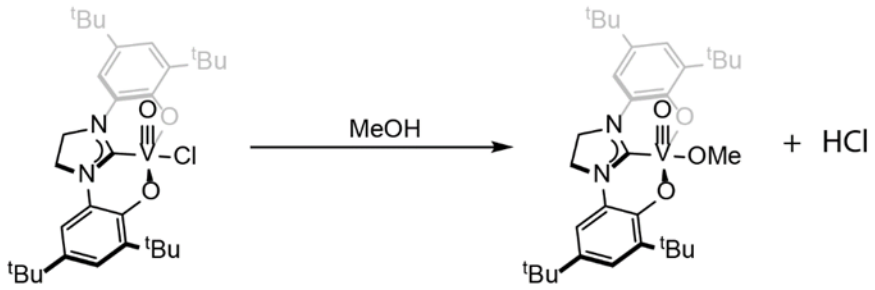

Scheme 3-1. Synthesis of [V(O)(OCO)OMe] from [V(O)(OCO)Cl].

3.2.3 Electrochemistry of [V(O)(OCO)X] complexes

The cyclic voltammogram (CV) of [V(O)(OCO)Cl] in MeCN solutions containing 0.1 M tetra-n-butylammonium hexfluorophosphate ([nBu_4N][PF_6]) using a platinum disk working electrode, platinum wire auxiliary electrode, and silver quasi-reference electrode showed a single reversible 1e– oxidation at E_{pa} = 0.71 V vs $Fc^{+/0}$ and a reduction at E_{pc} = -0.50 V vs $Fc^{+/0}$ (Figure 3-7). Exchanging methoxide for the chloride, [V(O)(OCO)OMe] causes a shift in these potentials to E_{pa} = 0.55 V vs $Fc^{+/0}$ and E_{pc} = -1.12 V vs $Fc^{+/0}$ respectively (Figure 3-7). The oxidations are thought to be ligand-centered as this is a d^0 vanadium and the reductions are metal centered vanadium(V) to vanadium(IV). Differences in potentials can be attributed to difference of X-type donor ligand in the complex, methoxide being a better sigma donor and able to stabilize the oxidized variant.

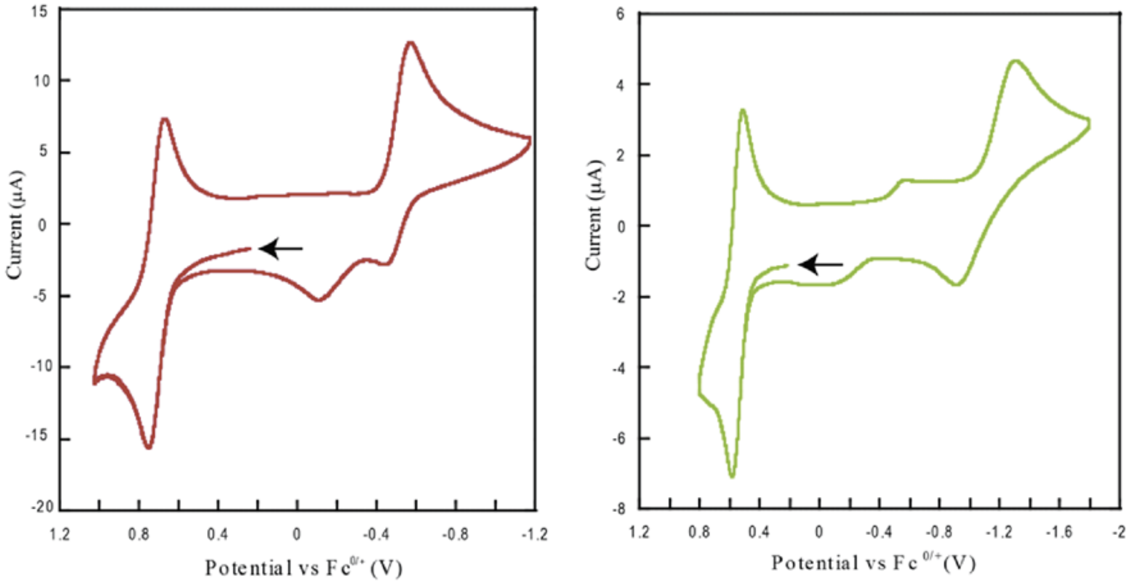

Figure 3-7. Cyclic voltammogram of [V(O)(OCO)Cl] (red) and [V(O)(OCO)OMe] (green) in MeCN solutions containing 0.1 M tetra-n-butylammonium hexfluorophosphate ($[nBu_4N][PF_6]$) using a platinum disk working electrode, platinum wire auxiliary electrode, and silver quasi-reference electrode with ferrocene as internal reference.

3.2.4 Preparation of [V2(O)2(OCO)2(m-O)]

The by-product of hydrochloric acid, HCl, in the above synthesis of VO(OCO)OMe prompted us to attempt the synthesis with sodium methoxide as an added base. When NaOMe is added to a methanol solution of VO(OCO)Cl the reaction is much more rapid, with the color change from red to green occurring in minutes versus hours. The reaction was exposed to air, filtered, concentrated in vacuo, and washed with ether. Surprisingly, the ^{1}H NMR spectrum of the green powder produced in this reaction showed new resonances that did not match those from [V(O)(OCO)Cl] or [V(O)(OCO)OMe]. Instead, four major peaks were observed in the aryl region and four in the region expected for the t-butyl resonances prompting us to conclude we had a mixture of vanadium products. The resonances shown in blue in Figure 3-8 represent the new material. Small amounts of unreacted [V(O)(OCO)Cl] remain as evidenced by diagnostic peaks at 7.48 and 6.42 ppm (red, top for comparison) and a very small amount of [V(O)(OCO)OMe] as evidenced by the peak at 5.05 ppm (green, middle).

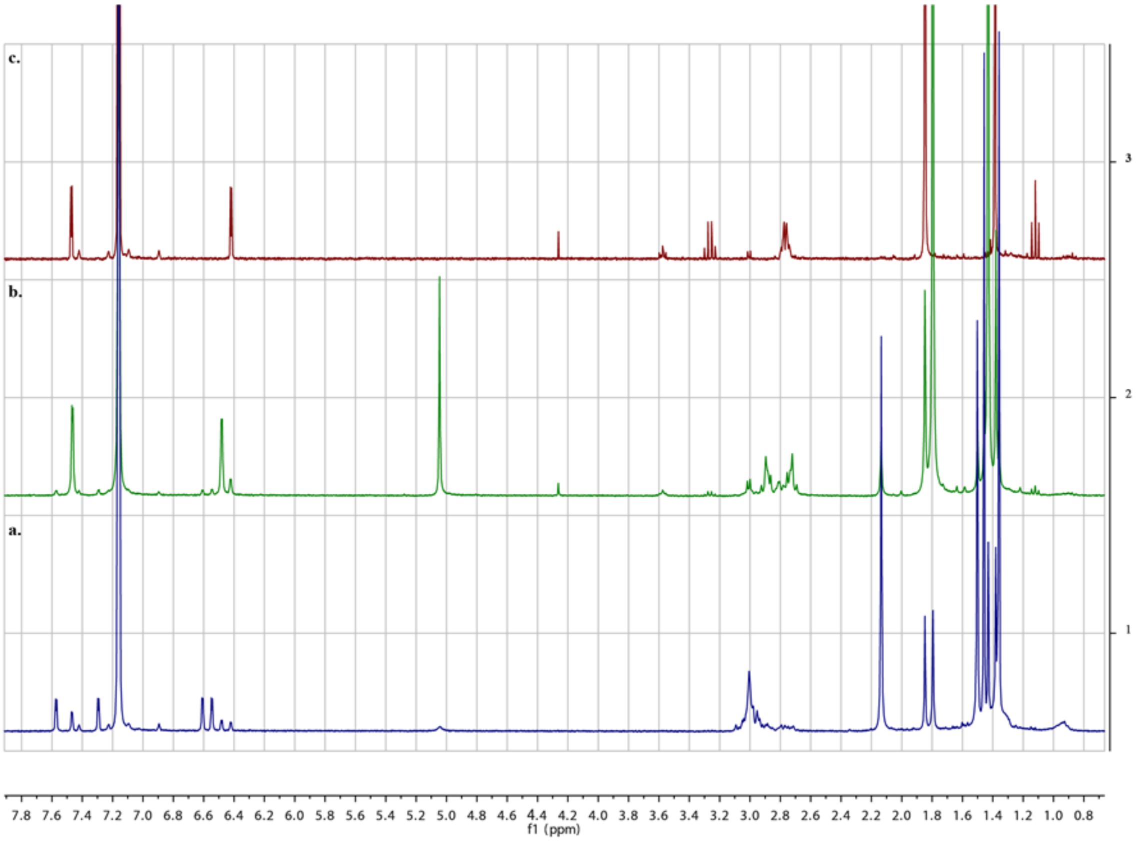

Figure 3-8. ^{1}H NMR, 300 MHz, C_6D_6 of a) dimer b) methoxide c) chloride

Crystals suitable for x-ray diffraction were grown from slow evaporation of a benzene solution of the green powder, which revealed a dimer of the vanadium fragment [V(O)(OCO)] with a μ–oxido. The NMR of the isolated crystals matched that of the powder permitting assignment of the ^{1}H NMR spectrum. Accordingly, the four ^{t}Bu resonances represent four chemically inequivalent ^{t}Bu in the symmetry-inequivalent (OCO) ligands.

The dimer complex, V-O-V, includes four molecules of benzene in the unit cell. An ORTEP plot of the V dimer is shown in Figure X. The two terminal oxo-vanadium bonds are nearly orthogonal. The planes defined by O1V1O7 and O1V2O4 of the dimer are at an angle of 73.3° to each other. The OCO ligands are in their fully reduced, dianionic, state as evidenced by the bond lengths around the phenoxide ring all being close to 1.40Å. The V–O distances for each half are identical at 1.592(2)Å and are shorter than the V–O distances of [V(O)(OCO)OMe] described above but longer than [V(O)(OCO)Cl], and consistent with a V–O triple bond expected for a vanadium center in the +5 oxidation state. Accordingly, formation of the dimer occurs without a formal change in the metal

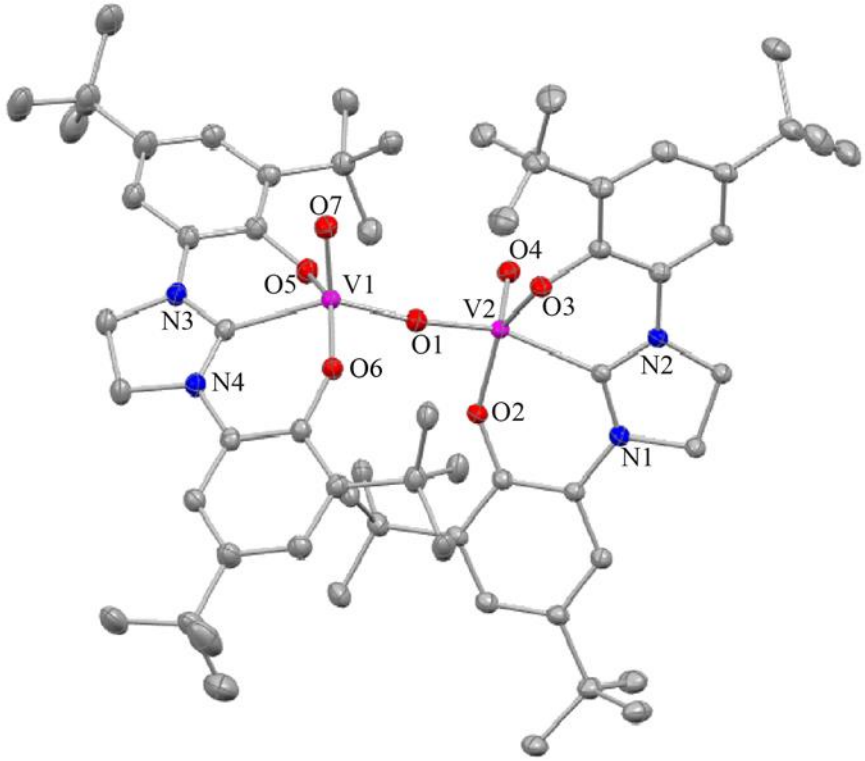

Figure 3-9. Crystal structure of [$V_2(O)_2(OCO)_2(\mu\text{-}O)$], ORTEP ellipsoids at 50% probability, hydrogens and 4 benzene solvent molecules omitted for clarity.

oxidation state, implying the net conversion of two [V(O)(OCO)X] monomers is balanced by the net addition of an oxide, O^{2-}, dianion.

3.2.5 Synthesis of Alkoxide complexes

With the chloride and methoxide variants in hand, attempts were made to synthesize the analogous isopropoxide and benzyloxide complexes as proposed in Scheme 3-2. Synthesis of [V(O)(OCO)OR] complexes. The sodium salts of benzyl alcohol and isopropanol were obtained by adding sodium metal to the neat alcohol. The excess alcohol was removed and white solid collected. The resulting solid was washed with ether to remove residual alcohol until free moving white powder was observed. The solids were then collected and dried in vacuo.

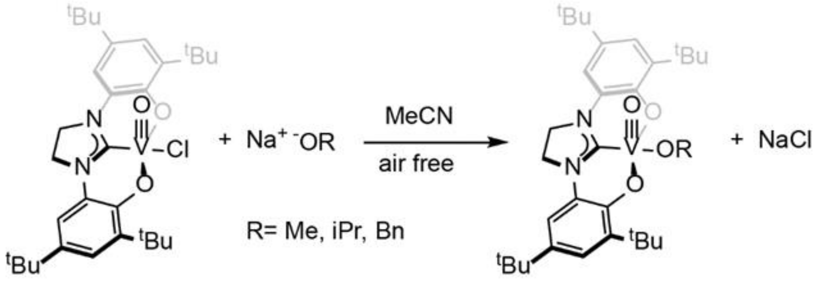

Scheme 3-2. Synthesis of [V(O)(OCO)OR] complexes

The solid sodium alkoxide was then added to a solution of VO(OCO)Cl in acetonitrile. Again, a color changed was observed from red to green. The resulting green solution was concentrated and washed with ether. Surprisingly, the ^{1}H NMR showed no evidence of the coordinated alkoxide, instead the μ-oxo vanadium(V) dimer was the major inorganic product with some unreacted starting material, as evidenced in the ^{1}H NMR spectrum in Figure 3-10. The only organic products seen in the ^{1}H NMR were benzaldehyde and benzoic acid, presumably deriving from oxidation with sodium benzyloxide. The benzoic acid was only detected after exposure of the NMR tube to air. This was confirmed by adding a small amount of the known compound to the NMR tube and watching the peaks at 11.03 and 9.62 ppm grow for benzoic acid and benzaldehyde, respectively. As these reactions were carried out under rigorously air-free conditions, the bridging oxide in the dimer product could not originate from air. Scheme 3-3. Proposed route to dimer from reaction of [V(O)(OCO)Cl] with alkoxide salt shows a balanced equation with the oxide coming from the isopropoxide as an example. Two more reactions were performed to confirm this observation. Under an inert atmosphere, sodium methoxide was added to a solution of VO(OCO)Cl and the resulting green solution was worked up as reported above but without exposure to air.

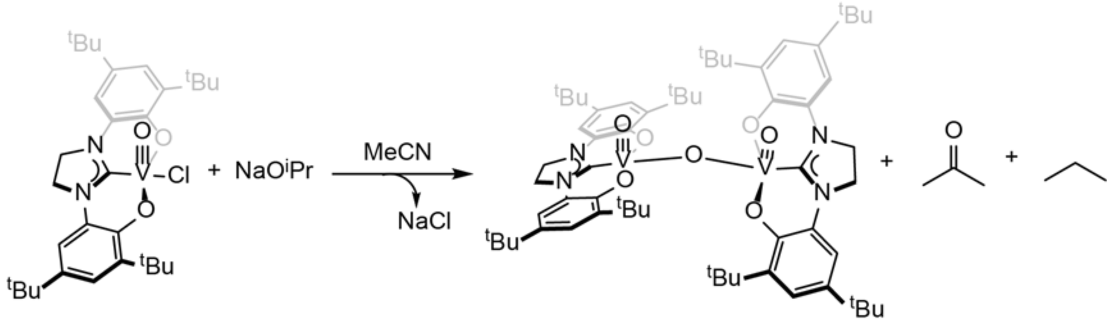

Scheme 3-3. Proposed route to dimer from reaction of [V(O)(OCO)Cl] with alkoxide salt

The ^{1}H NMR of the green solid collected clearly showed dimer formation (b of Figure 3-10). As a control, a tert-butyloxide complex was also attempted as β-hydrogen elimination would not be possible. Addition of potassium tert-butoxide to a THF solution of VO(OCO)Cl gave the same color change from red to green from which a green solid was isolated with a ^{1}H NMR spectrum that matched exactly the [$V_2(O)_2(OCO)_2(\mu\text{-}O)$]

dimer as the major inorganic product. Some unreacted starting material remained as a minor species in the ^{1}H NMR spectrum. GC-MS detected 3-butenal and signals for the aldehyde were seen in the ^{1}H NMR. The C4 product apparently derives from ring-opening and oxidation of THF. Figure 3-10 summarizes the ^{1}H NMR results of the reactions with alkoxides. This reactivity is reminiscent of deoxydehydration of the alkoxide as both C–H and C–O bonds are broken. Possible mechanistic pathways and experiments to delineate the route to these products are discussed below. But aside from the OMe complex, all attempts to prepare alkoxide [V(O)(OCO)OR] complexes have instead afforded only the dimer.

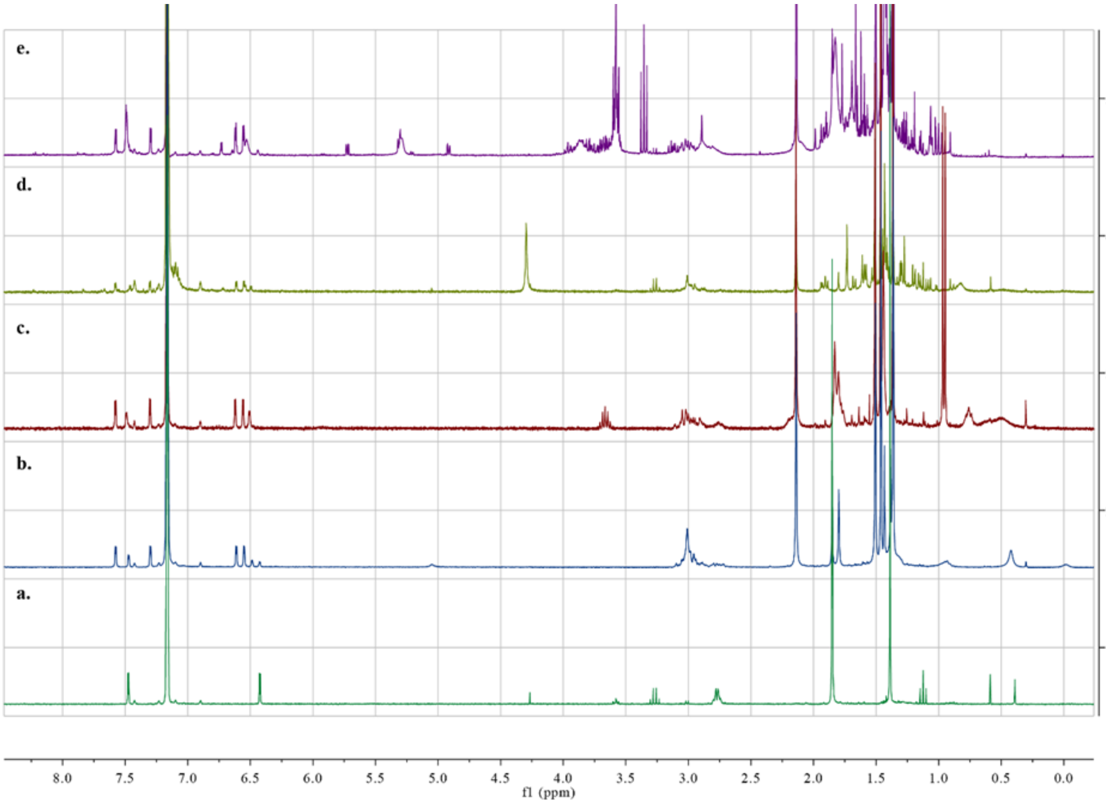

Figure 3-10. ^{1}H NMR, 300MHz, C_6D_6, product from reaction of [V(O)(OCO)Cl] and NaOR. a) [V(O)(OCO)Cl], b) R=OMe, c) R=OiPr, d) R=OBn, e) R=OtBu

3.2.6 Reactivity with alcohols

When neat benzyl alcohol was added to a vial of VO(OCO)Cl there was an immediate color change from red to blue (Figure 3-11). In the absence of air this blue color persists for days. When exposed to air there is a slow color change back to red over hours with formation of a UV-vis spectrum that approximates but does not match the original (Figure X). Which might reflect by-products that absorb in the same range. Benzaldehyde was detected by both GC-MS and ^{1}H NMR. Similarly, if neat HO^{i}Pr was added to a vial of VO(OCO)Cl there was a rapid initial color change from red to green in seconds followed by a slightly slower color change from green to blue in minutes that mirrors that observed for BnOH. However, the product of oxidation of isopropanol, acetone, was not seen by ^{1}H NMR, perhaps because of evaporation when removing the excess alcohol.

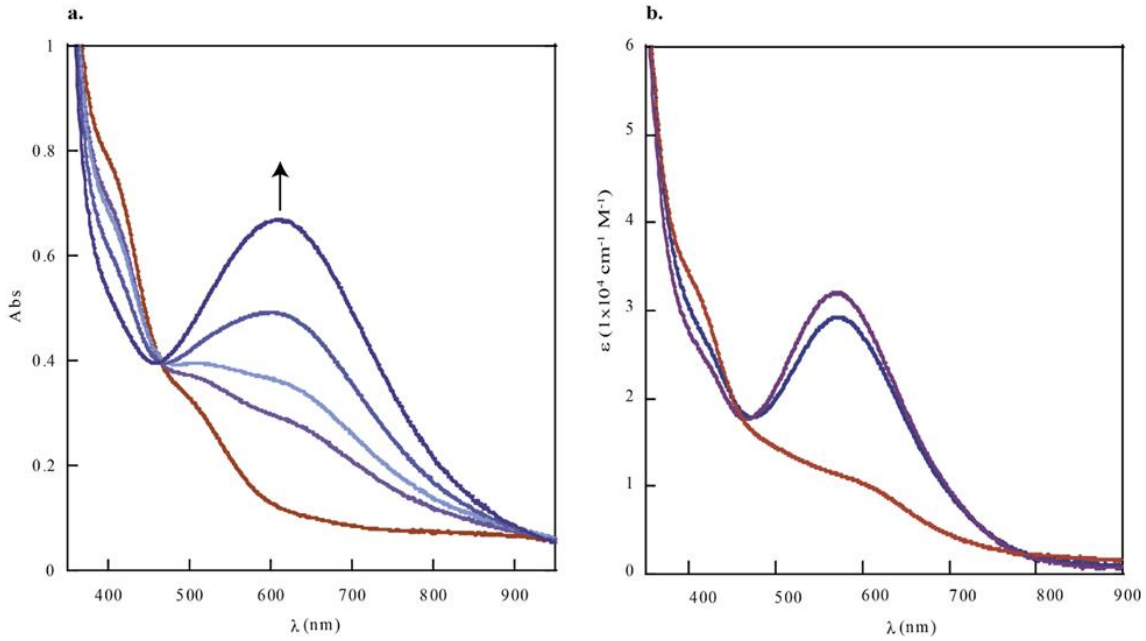

Figure 3-11. a) red trace: VO(OCO)Cl in MeCN purple to blue traces: increasing BnOH concentration, b) red trace: VO(OCO)Cl in benzene with BnOH 24 hr after exposure to air. Blue and purple traces: VO(OCO)Cl in benzene with BnOH 24 and 48 hr air-free.

3.2.7 Reactivity with O_2

With the initial assumption that oxygen was required for dimer formation we attempted to clarify the role of oxygen. The chloride complex shows no reaction with air in either the solid state or solution (MeCN, benzene, or DCM) over five days at 40 °C. Conversely, exposure of the methoxide complex to air generates a paramagnetic species. Three J. Young tubes were charged with VO(OCO)OMe in d_6-benzene under a nitrogen atmosphere. One tube was kept under nitrogen while the other two were subsequently exchanged for dry air or oxygen.

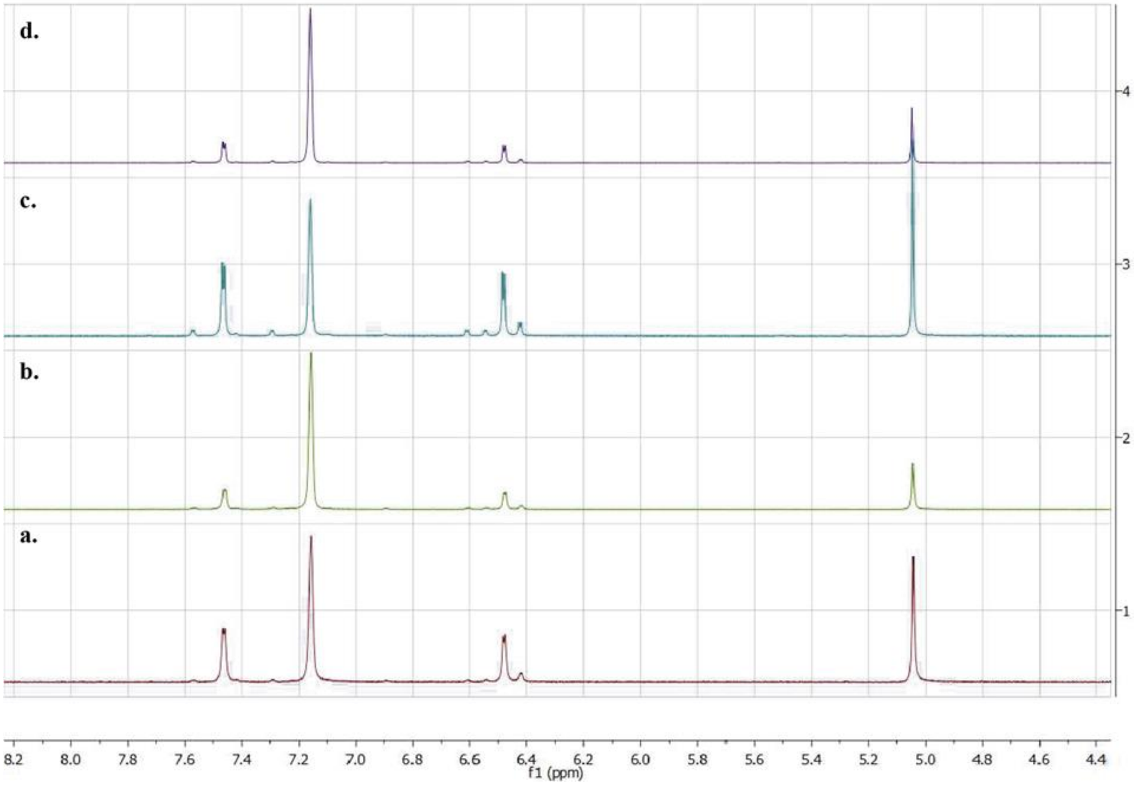

Figure 3-12. ^{1}H NMR of [V(O)(OCO)OMe] a) initially under N_2, b) after introduction of O_2, c) after O_2 replaced with N_2, d) after reintroduction of O_2.

Unexpectedly, no dimer formation was seen but rather only the disappearance of starting material signal was observed in the tubes under air or O_2 as evidenced by the reduction of peaks at 7.47, 6.48, 5.05, 2.81, 1.80 and 1.43ppm. No other ^{1}H NMR active species were formed and the mass balance (by integration against the solvent peak) suggested 40% remained after 2 h for the tube under air and 34% for the tube under O_2, Table 3-2. Surprisingly, the disappearance of the starting material signal was reversible. When O_2 was removed by freeze-pump-thaw cycles and the tube was placed back under N_2, the diagnostic signals at 7.47, 6.48, and 5.05 ppm reappeared. Introduction of O_2 a second time caused the signals to disappear again, as seen in Figure 3-12, suggesting O_2 was reversibly binding. The absence of observable resonances for the putative O_2 adduct suggested the O_2

complex was paramagnetic. A proposed superoxo structure is shown in Scheme 3-4. The relevance of this complex and the role of the redox-active ligand in its formation are discussed below.

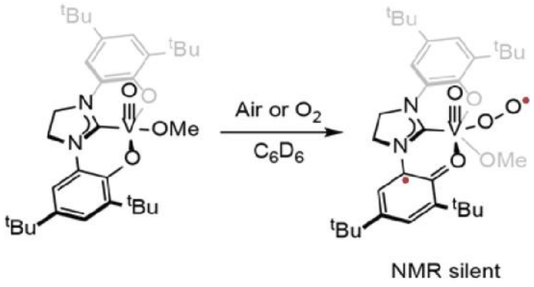

Scheme 3-4. Proposed superoxo formation

Table 3-2. Total ^{1}H signals of [V(O)(OCO)OMe] by integration against solvent over time

Total ^{1}H signal (vs internal standard)				
Atmosphere	**Initial**	**1hr**	**2hr**	**90hr**
Nitrogen	77	77	73	78
Dry air	77	35	31	33
Oxygen	77	27	26	26

3.2.8 Oxidation of [V(O)(OCO)Cl]

The observation of a reversible oxidation of [V(O)(OCO)Cl] at +0.71 V vs $Fc^{+/0}$ prompted efforts to prepare and isolate the 1e– oxidized complex. Initial attempts used tris(2,4-dibromophenyl)aminium hexachloroantimonate, also known as “magic green.” The oxidation potential of magic green in MeCN is 1.14V vs $Fc^{0/+}$. Two different approaches were attempted. First, in a cuvette at UV-vis concentrations, magic green was titrated in starting at 0.25 equivalents and incrementally adding oxidant until 2 equivalents had been added. In a second attempt one equivalent of magic green was slowly added to an acetonitrile solution of VO(OCO)Cl. In both, the emerald green color of the magic green disappeared with a very slight change in color to the characteristic red solution of VO(OCO)Cl immediately upon mixing. After 5 minutes of stirring an off-white precipitate formed. The resulting solution was then filtered and concentrated in vacuo before being taken back up in MeCN for CV and UV-vis characterization.

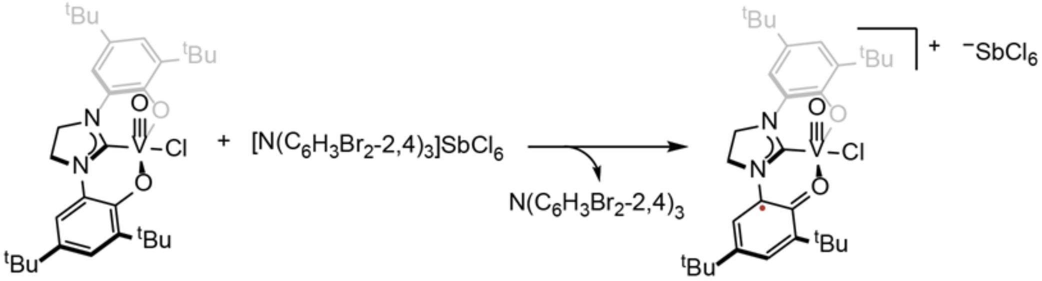

Scheme 3-5. Oxidation of [V(O)(OCO)Cl] by "magic green'

The CV of the solid collected included additional peaks aside from the oxidation and reduction previously seen, indicating an impure sample. The open circuit potential of the solid collected was expected to be above that of the oxidation event observed for VO(OCO)Cl at 0.71V but the measured open circuit potential at 0.24 V was below that oxidation event. This could be due to incomplete oxidation or degradation of the oxidized compound due to its highly oxidizing nature. The triarylaminium radical cation is an innocent 1e– oxidant but the counterion used, $SbCl_6^-$, can be a source of nucleophilic Cl^- equivalents which may also play a role in the instability of the oxidized complex.[14] To this point, an oxidized product has not been successfully isolated. It is possible that due to the high oxidizing power of this complex it is unstable and complicates the ability to isolate it.

3.2.9 Attempted OAT and HAT with [V(O)(OCO)Cl]

Attempted reductions of [V(O)(OCO)Cl] by oxygen atom transfer to triphenylphosphine in a DCM solution gave no detectable reactions by UV-vis or ^1H NMR spectroscopy over two day at ambient temperature under an inert atmosphere. Similarly, hydrogen atom transfer to VO(OCO)Cl from the H-atom donor, 9,10-dihydroanthracene, was attempted by adding half an equivalent of DHA to an MeCN solution of VO(OCO)Cl. Again, there was no detectable color change and the NMR was unchanged, showing the signature peak for DHA at 3.92 ppm.

3.3 Discussion

3.3.1 Solid state structures and electrochemistry

Trends in the solid-state structures and cyclic voltammograms can both be rationalized considerations of the relative by the sigma donor abilities of the X-type ligand. Methoxide is a better base and better sigma-donor than chloride ligand therefore better stabilizes the electron deficient metal center. This allows the OCO ligand of the methoxide complex to be oxidized at a lower potential than that of the chloride. One half of the [$V_2(O)_2(OCO)_2(\mu$-O)] dimer is isostructural with [V(O)(OCO)OR] where the (μ-O)V(O)(OCO) fragment replaces OR. And while the bridging oxide would be the best base out of the -X type ligands trans to the NHC, two vanadium centers are competing for the same orbitals of that oxygen which accounts for its metrics being between those of the methoxide and chloride complexes. The sigma donor capacity of the -X ligand also rationalizes the V–C bond distances to the NHC. The carbon of the NHC is a strong sigma donor and competes for the same orbitals as the ligand in trans to it.[15] Accordingly, the stronger the sigma donor trans to the NHC the weaker and therefore longer the bond between vanadium and the carbon. The effects of π-donation to these bonds distances is less clear. Chloride and methoxide are both π donors while NHCs are both π donors and acceptors. It is uncertain how much this plays a role in the bond lengths seen in these complexes.

3.3.2 Reactivity with alkoxides

Generation of aldehydes from VO(OCO)OR complexes requires the formal removal of hydride from a C–H bond. We initially suspected O_2 supplied the oxide that forms the μ–O bridge of the dimer, data suggests that the added oxygen equivalent comes from the alkoxide ligand. In sum, the reaction products are consistent with described oxidative-reductive coupling which has precedence with other oxovanadium complexes. A balanced reaction for production of the dimer as well as the organic products is shown in Scheme 3-6 and shows the proposed steps in this process for the alkoxide complexes. Slow β-

hydride transfer to the oxo ligand produces a vanadium(III)hydroxo and the aldehyde (step 1 of Scheme 3-6). As we see no evidence for the buildup of an intermediate, this first step must necessarily be the slow step of the overall reaction. This could occur via base-assisted proton transfer or hydrogen atom transfer (HAT). There is literature precedent to support both one- and two-electron processes.2 As this reactivity is seen only when base is present and not in reactions with alcohols it is reasonable to assume the base plays a role. In the second step of Scheme 3-6, the vanadium(III)hydroxo and the starting vanadium(V)oxo comproportionate to form a vanadium(IV,IV) dimer, which is poised to eliminate alkane, generating the observed vanadium (V,V) dimer. Similar to step 1, this process could also proceed through a series of one- or two-electron transfers with either a carbon hydrogen radical coupling or hydride transfer. As there is electronic communication through the oxo-bridge and both vanadium centers would prefer to be the +5 oxidation state, this possibility is not unreasonable. More experiments are required to fully distinguish a mechanism and are discussed later.

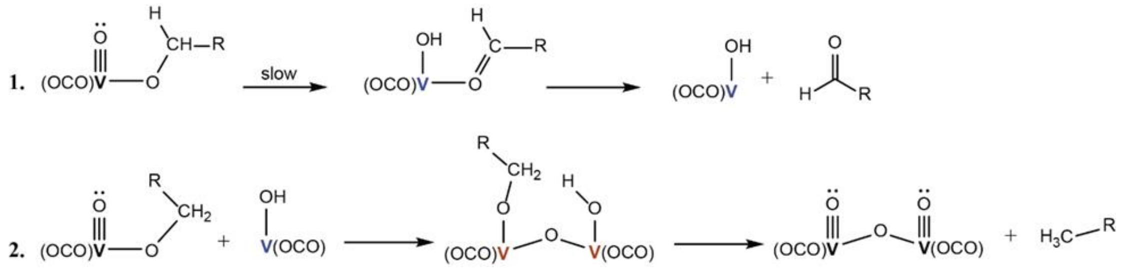

Scheme 3-6. Proposed steps for the reaction with alkoxides. Black V(V), red V(IV), blue V(III)

As drawn, the bridging oxo originates as the terminal oxo of the alkoxide complex. The oxo of the alkoxide cannot be ruled out as the bridging oxo. This proposal would likewise situate the carbon and hydrogen for elimination to form the alkane and vanadium dimer.

As yet, there is no evidence of catalytic reactivity. To make this reaction catalytic, two equivalents of alcohol would be necessary to break up the dimer and produce the starting alkoxide and an equivalent of water. It is unclear how addition of alcohol may affect the reactivity. As discussed above, the exact mechanism for the C–H and C–O bond breaking is still unclear, although the necessity of base lends itself to a two-electron mechanism as it is unclear what role base would play a role in radical processes. The other possibility that cannot be ruled out is whether the first step is mono- or bi-metallic. If this is indeed the rate determining step, kinetics could be used to probe the effect of metal concentration on dimer formation.

Additional experiments should permit a more detailed understanding of the mechanism of dimer formation. For instance, O^{18} labeling studies using labeled OR would allow determination of the source of the μ–O bridge by mass spectrometry and FT-IR. Independently synthesizing a vanadium(III) hydroxo to see if that reacts with the vanadium(V) alkoxide to produce the dimer and a hydrocarbon would help confirm a mechanism. H/D experiments to determine the kinetic isotope effect (K.I.E.) would be an effective way to determine if C–H bond breaking is the slow step. Kinetic experiments varying the concentration of metal would clarify a mono- or bi-metallic first step. So far, only the aldehyde products have been observed in NMR or GC-MS. Using GC-MS or GC-FID to identify the other organic products in these reactions would give solid evidence for DODH products. If this can be made catalytic, quantifying the organics would help determine the catalytic efficiency.

Interestingly, the reaction of the chloride complex with alcohol not only has no base present, but also an equivalent of acid is produced. While both reactions produce an oxidized aldehyde, the intermediate hydroxide species is in different environments (Scheme 3-6 vs Scheme 3-7) and that can be the origin of the divergence in reactivity. The reactivity with alcohols is discussed in the following section.

3.3.3 Reactivity with alcohols

As noted above, the reactions of alcohol with VO(OCO)Cl proceeded without a base present and do not require O_2. Analysis of the products from the reactions with alcohol suggests a different mechanism is operative than those discussed above for the reactions with alkoxides. Schemes 3-7 and 3-8 outline possible two- and one-electron pathways for this oxidation to occur.

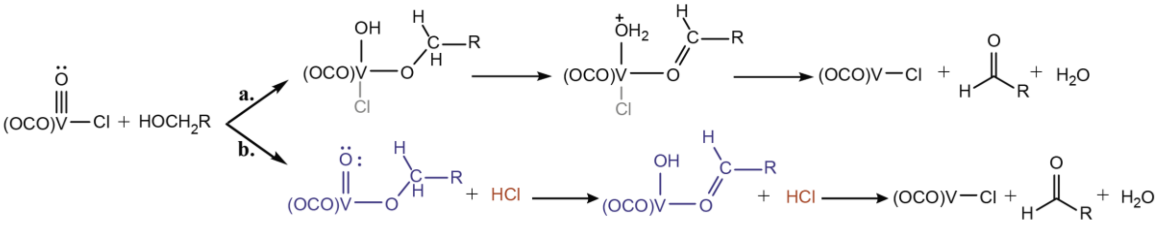

Scheme 3-7. Possible two-electron pathways for alcohol oxidation by [V(O)(OCO)Cl]

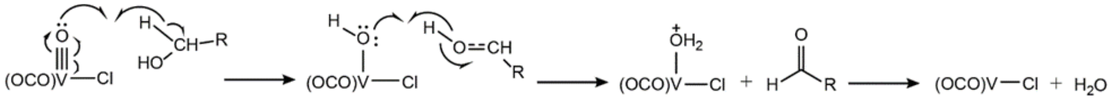

Scheme 3-8. Possible one-electron pathway for alcohol oxidation by [V(O)(OCO)Cl]

From the reactions with isopropanol, it appears that formation of the alkoxide product is an intermediate as a color change to green was observed before going on to blue. That leads to pathway b of scheme X. The two intermediates shown in blue for pathway b are the same as those proposed for the DODH of alkoxides. The difference being the presence of

HCl in the reaction mixture. After β-hydrogen transfer, the acid protonates the resulting hydroxo to produce water as a leaving group while chloride binds to the vanadium giving the vanadium(III) chloride complex. The stability of the alkoxide intermediate, and therefore the ability to observe it, follows the C–H bond strength of the β -hydrogen: HOBn < HO*ⁱ*Pr < HOMe, with the methoxide adduct able to be isolated and characterized. The other possible two-electron mechanism utilizes the terminal oxo as the acceptor of both hydrogens from the alcohol and the chloride stays bound. There is evidence in the literature that for mono-oxo vanadium complexes, the first hydrogen is transferred to a leaving group as opposed to the oxo while di-oxo vanadium complexes accept both hydrogens to form two hydroxo ligands. The one-electron pathway is a series of H-atom transfers starting with a hydrogen on carbon as that is a weaker bond than that of hydrogen and the oxygen. This mechanism contains no alkoxide intermediate and as the VO(OCO)Cl showed no HAT reactivity with DHA, a one-electron mechanism seems unlikely. Products of C–O bond breakage are not observed and UV-vis results suggest a vanadium species other than the dimer as the inorganic product. The reactions in alcohol and air have the ability to be catalytic. After the aldehyde is formed from the alcohol, half an equivalent of O_2 can then oxidize the vanadium(III)Cl complex to the starting vanadium(V), closing the catalytic cycle shown in Figure 3-13.

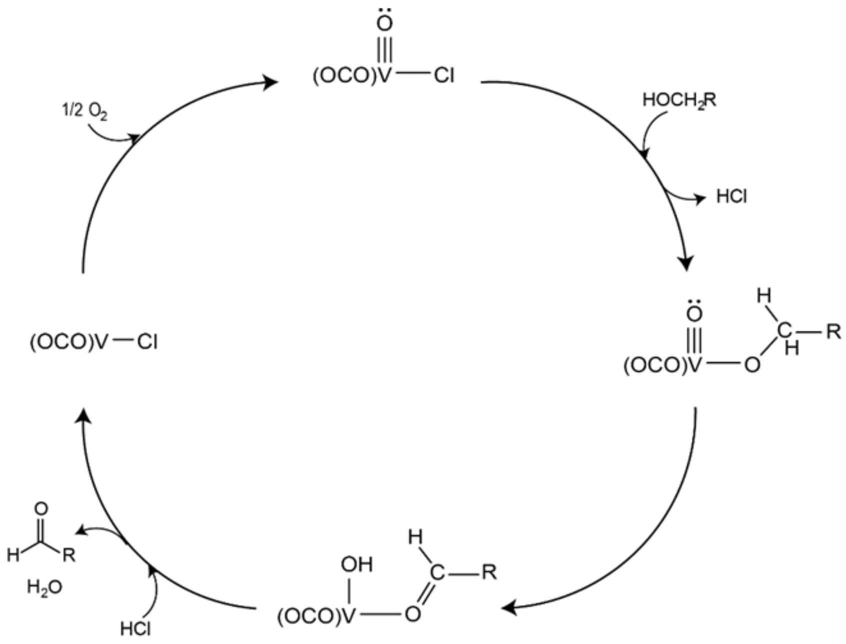

Figure 3-13. Proposed catalytic cycle for aerobic alcohol oxidation by [V(O)(OCO)Cl]

3.3.4 Reactivity with O_2

Results from the NMR tube experiments with O_2 led to surprising conclusions. We expected to see ROH oxidations, with a 5x difference in rate if there was a first order dependence on oxygen using pure O_2 versus dry air and no dimer formation in the tube under nitrogen. Instead we discovered that without a base present there is effectively no dimer formation. Instead, the starting ^{1}H NMR signals disappear. We concluded this is most likely the result of a paramagnetic species being formed. As there is a possibility for ligand oxidation, we believe this paramagnetic species is a superoxo adduct. Formulation as (OCO•)V(O)(O_2•) implies two unpaired electrons, as reduction of the O_2 oxidizes the (OCO)V(O) complex. The redox-active (OCO) ligand is the only available source of reducing equivalents in the d^0 metal complex. The lack of observable ^{1}H NMR signals suggests the complex is paramagnetic, which would require the two spins to be antiferromagnetically coupled. This has been observed in a closely related oxorhenium system. Further NMR experiments showed this process is fully reversible with starting material peaks reappearing upon replacement of O_2 with N_2. The lower oxidation potential of the methoxide complex, described earlier by the differences in electron donating ability of methoxide versus chloride, explains this reactivity with O_2. The methoxide complex is oxidized 160mV below the chloride complex and the similarity in structures suggests a kinetic effect is unlikely. Reactivity-wise the chloride complex is completely stable in air whereas when synthesizing the methoxide complex any exposure to O_2 will lead to formation of the μ-oxo dimer if base is present or a disappearance of NMR signals.

3.4 Conclusion

This study did not answer the question regarding reaction selectivity based on ligand oxidation state and how this could affect reactivity at the oxo that we initially posed. This was complicated, in part, by the inability to isolate the one-electron oxidized product of [V(O)(OCO)Cl]. Importantly, we did demonstrate that the chloride complex is capable of aerobic alcohol oxidation. We also supplied strong evidence to support both C–H and C–O bond cleavage of simple alkoxides. Both modes of reactivity have the potential to be catalytic. Going forward, more focus must be paid to the reactivity and oxidation of [V(O)(OCO)OMe]. The lower oxidation potential of the methoxide relative to the chloride would make isolating the oxidized version easier as a different more benign oxidant can be used. The apparent reactivity of the methoxide with O_2 deserves follow-up. These results have implications for the larger problem of conversion of lignin biomass into commodity chemicals.

3.5 Experimental

3.5.1 General considerations

Unless otherwise specified, all manipulations were performed under anaerobic conditions using standard vacuum line techniques, or in an inert atmosphere glove box under purified nitrogen. Routine NMR spectra were acquired on a Varian Mercury 300 spectrometer (300.323 MHz for 1H; 75.5 MHz for 13C). All chemical shifts are reported in parts per million (ppm) relative to TMS, with the residual solvent peak serving as an internal reference. Solution magnetic moments were obtained by Evan's NMR method, and are reported as the average of three independent measurements, unless otherwise specified. UV–visible absorption spectra were acquired using a Varian Cary 50 spectrophotometer. Unless otherwise noted, all electronic absorption spectra were recorded at ambient temperatures in 1 cm quartz cells. IR absorption spectra were obtained via attenuated total reflection (ATR) with a diamond plate using a Bruker ALPHA Fourier-transform infrared spectrophotometer. All mass spectra were recorded in the Georgia Institute of Technology Bioanalytical Mass Spectrometry Facility. Electrospray ionization mass spectrometry (ESI–MS) was carried out with acetonitrile solutions using a Micromass Quattro LC spectrometer. Electron impact mass spectra (EI–MS) were obtained using a VG instruments model 70-SE spectrometer. Cyclic voltammetry experiments were performed inside an N_2-filled glove box in MeCN with 0.1 M ($[nBu_4N][PF_6]$) as the supporting electrolyte, unless otherwise noted. The voltammograms were recorded with a CH Instruments 620C potentiostat, using a 2.5 mm (O.D) 1.0 mm (I.D.) Pt disk working electrode, Ag wire quasi-reference electrode, and a Pt wire auxiliary electrode, at a scan rate of 0.1 V s^{-1}, unless reported otherwise. Reported potentials are referenced to the ferrocenium/ferrocene (Fc^+/Fc) redox couple, added as an internal standard at the conclusion of each experiment. Elemental analyses were performed by Atlantic Microlab, Inc., Norcross, GA. All analyses were performed in duplicate, and the reported compositions are the average of the two runs.

3.5.2 Materials and methods

Anhydrous acetonitrile (MeCN), dichloromethane, pentane, tetrahydrofuran (THF) and toluene solvents for air- and moisture-sensitive manipulations were purchased from Sigma-Aldrich and further dried by passage through columns of activated alumina, degassed by at least three freeze-pump-thaw cycles, and stored under N_2 prior to use. Anhydrous diethyl ether (Drisolv), methanol (Drisolv), and benzene (Drisolv) were purchased from EMD Millapore and used as received. Dichloromethane-d2 and acetonitrile-d3 (Cambridge Isotope Labs) were dried over excess calcium hydride and vacuum distilled to an oven-dried sealable flask, and degassed by successive freeze-pump-thaw cycles. Tetrahydrofuran-d8, chloroform-d1, benzene-d6, and methanol-d4 (Cambridge Isotope Labs) were used as received. The materials (N,N'-bis(2-hydroxy-3,5-di-tertbutylphenyl) ethylenediamine, the ligand H_3[(OCO)]Cl, VO(OCO)Cl, tris(2,4-dibromophenyl)amine, and tris(2,4-dibromophenyl)aminium hexachloroantimonate (magic green) were prepared according to published procedures and all characterization data matched those reported.[13, 16-17] Triethyl orthoformate (Alfa Aesar) and triisopropoxyvanadium(V) oxide (Stem) were used as received.

3.5.3 Synthesis of [V(O)(OCO)OMe]

The methoxide derivative was synthesized by dissolving 1 (100 mg, 0.17 mmol) in excess methanol (10 mL) with stirring overnight. The resulting light green solid was collected by filtration, washed with methanol and dried in vacuo (63 mg, 63% yield). NMR (1H, 300MHz, C6D6): 7.46 (d, J=2.2 Hz, ArH, 2H), 6.49 (d, J=2.2 Hz, ArH, 2H), 5.04 (s, OCH3, 3H), 2.81 (m, NHC, 4H), 1.80 (s, tBu, 18H), 1.43 (s, tBu, 18H) UV–vis (solvent) λmax, nm (ε, M–1 cm–1): Anal. Calc. for C32H47N2O4V: C, 66.88; H, 8.24; N, 4.87. Found: C H N

3.5.4 Synthesis of [$V_2O_2(OCO)_2(\mu$-O]

The oxo-bridged dimer was synthesized by stirring a solution of [V(O)(OCO)Cl] (137 mg, 0.24 mmol) in methanol overnight. The resulting solution was concentrated in vacuo, washed with methanol, dried, and recrystallized from benzene (yield). NMR (1H, 300MHz, C6D6): 7.57 (d, J=2.2 Hz, ArH, 2H) 7.30 (d, J=2.2 Hz, ArH, 2H), 6.61 (d, J=2.2 Hz, ArH, 2H), 6.54 (d, J=2.2 Hz, ArH, 2H), 3.01 (m, NHC, 8H), 2.14 (s, tBu,18H), 1.50 (s, tBu, 18H), 1.46 (s, tBu, 18H), 1.36 (s, tBu, 18H). UV–vis (solvent) λmax, nm (ε, M–1 cm–1): Anal. Calc. for C62H88N4O7V2: C, 67.5; H, 8.04; N, 5.08. Found: C H N

3.5.5 General procedure for attempted alkoxide formation

The appropriate alkoxide salt (1.1eq) was added to a MeCN solution of [V(O)(OCO)Cl] and allowed to stir for 2h. The reaction mixture was then concentrated in vacuo and washed with diethyl ether.

3.6 X-ray Crystallography

3.6.1 [V(O)(OCO)OMe]

Single crystals of $C_{32}H_{47}N_2O_4V$ were recrystallised from a methanol solution. A suitable crystal was selected and the crystal was mounted on a loop in paratone oil on a 'Bruker APEX-II CCD' diffractometer. The crystal was kept at 100(2) K during data collection. Using Olex2[18], the structure was solved with the ShelXT[19] structure solution program using Intrinsic Phasing and refined with the ShelXL[20] refinement package using Least Squares minimisation.

Crystal Data for $C_{32}H_{47}N_2O_4V$ (M =574.65 g/mol): monoclinic, space group P21/c (no. 14), a = 15.686(2) Å, b = 11.4909(16) Å, c = 18.732(3) Å, β = 114.186(5)°, V = 3080.1(7) Å3, Z = 4, T = 100(2) K, μ(MoKα) = 0.359 mm-1, Dcalc = 1.239 g/cm^3, 33469 reflections measured (4.272° ≤ 2Θ ≤ 54.968°), 7063 unique (Rint = 0.0637, Rsigma = 0.0484) which were used in all calculations. The final R1 was 0.0621 (I > 2σ(I)) and wR2 was 0.1226 (all data).

3.6.2 *$[V_2(O)_2(OCO)_2(\mu\text{-}O)]$*

Single crystals of $C_{86}H_{112}N_4O_7V_2$ Were recrystallised from benzene. A suitable crystal was selected and the crystal was mounted on a loop with paratone oil on a 'Bruker APEX-II CCD' diffractometer. The crystal was kept at 100(2) K during data collection. Using Olex2[18], the structure was solved with the ShelXT[19] structure solution program using Intrinsic Phasing and refined with the ShelXL[20] refinement package using Least Squares minimisation

Crystal Data for $C_{86}H_{112}N_4O_7V_2$ (M =1415.67 g/mol): monoclinic, space group P21/n (no. 14), a = 16.416(3) Å, b = 26.128(6) Å, c = 19.953(5) Å, β = 111.572(9)°, V = 7959(3) Å3, Z = 4, T = 100(2) K, μ(MoKα) = 0.290 mm-1, Dcalc = 1.181 g/cm3, 119347 reflections

measured ($4.496° \leq 2\Theta \leq 51.362°$), 15105 unique ($R_{int} = 0.0726$, $R_{sigma} = 0.0393$) which were used in all calculations. The final R1 was 0.0650 ($I > 2\sigma(I)$) and wR2 was 0.1447 (all data).

3.7 References

1. Gazi, S., Valorization of wood biomass-lignin via selective bond scission: A minireview. *Applied Catalysis B: Environmental* **2019,** *257*, 117936.

2. Mukherjee, A.; Mandal, T.; Ganguly, A.; Chatterjee, P. K., Lignin Degradation in the Production of Bioethanol – A Review. *ChemBioEng Reviews* **2016,** *3* (2), 86-96.

3. Zakzeski, J.; Bruijnincx, P. C. A.; Jongerius, A. L.; Weckhuysen, B. M., The Catalytic Valorization of Lignin for the Production of Renewable Chemicals. *Chemical Reviews* **2010,** *110* (6), 3552-3599.

4. Ventura, M.; Domine, M. E.; Chávez-Sifontes, M., Catalytic Processes For Lignin Valorization into Fuels and Chemicals (Aromatics). *CCAT* **2019,** *8* (1), 20-40.

5. Son, S.; Toste, F. D., Non-Oxidative Vanadium-Catalyzed C□O Bond Cleavage: Application to Degradation of Lignin Model Compounds. *Angewandte Chemie International Edition* **2010,** *49* (22), 3791-3794.

6. Hanson, S. K.; Baker, R. T., Knocking on Wood: Base Metal Complexes as Catalysts for Selective Oxidation of Lignin Models and Extracts. *Accounts of Chemical Research* **2015,** *48* (7), 2037-2048.

7. Hanson, S. K.; Wu, R.; Silks, L. A. P., C□C or C□O Bond Cleavage in a Phenolic Lignin Model Compound: Selectivity Depends on Vanadium Catalyst. *Angewandte Chemie International Edition* **2012,** *51* (14), 3410-3413.

8. Hanson, S. K.; Baker, R. T.; Gordon, J. C.; Scott, B. L.; Silks, L. A. P.; Thorn, D. L., Mechanism of Alcohol Oxidation by Dipicolinate Vanadium(V): Unexpected Role of Pyridine. *Journal of the American Chemical Society* **2010,** *132* (50), 17804-17816.

9. Steffensmeier, E.; Swann, M. T.; Nicholas, K. M., Mechanistic Features of the Oxidation–Reductive Coupling of Alcohols Catalyzed by Oxo-Vanadium Complexes. *Inorganic Chemistry* **2019,** *58* (1), 844-854.

10. Shiramizu, M.; Toste, F. D., Deoxygenation of Biomass-Derived Feedstocks: Oxorhenium-Catalyzed Deoxydehydration of Sugars and Sugar Alcohols. *Angewandte Chemie International Edition* **2012,** *51* (32), 8082-8086.

11. Shiramizu, M.; Toste, F. D., Expanding the Scope of Biomass-Derived Chemicals through Tandem Reactions Based on Oxorhenium-Catalyzed Deoxydehydration. *Angewandte Chemie International Edition* **2013,** *52* (49), 12905-12909.

12. Chun, H.; Verani, C. N.; Chaudhuri, P.; Bothe, E.; Bill, E.; Weyhermüller, T.; Wieghardt, K., Molecular and Electronic Structure of Octahedral <i>o</i> -Aminophenolato and <i>o</i> -Iminobenzosemiquinonato Complexes of V(V), Cr(III), Fe(III), and Co(III). Experimental Determination of Oxidation Levels of Ligands and Metal Ions. *Inorganic Chemistry* **2001,** *40* (17), 4157-4166.

13. Bellemin-Laponnaz, S.; Welter, R.; Brelot, L.; Dagorne, S., Synthesis and structure of V(V) and Mn(III) NHC complexes supported by a tridentate bis-aryloxide-N-heterocyclic carbene ligand. *Journal of Organometallic Chemistry* **2009,** *694* (5), 604-606.

14. Connelly, N. G.; Geiger, W. E., Chemical Redox Agents for Organometallic Chemistry. *Chemical Reviews* **1996,** *96* (2), 877-910.

15. Waltman, A. W.; Grubbs, R. H., A New Class of Chelating N-Heterocyclic Carbene Ligands and Their Complexes with Palladium. *Organometallics* **2004,** *23* (13), 3105-3107.

16. Odom, S. A.; Ergun, S.; Poudel, P. P.; Parkin, S. R., A fast, inexpensive method for predicting overcharge performance in lithium-ion batteries. *Energy Environ. Sci.* **2014,** *7* (2), 760-767.

17. Yueh, W.; Bauld, N. L., Mechanistic Criteria for Cation Radical Reactions: Aminium Salt-Catalyzed Cyclopropanation. *Journal of the American Chemical Society* **1995,** *117* (21), 5671-5676.

18. Dolomanov, O.V., Bourhis, L.J., Gildea, R.J, Howard, J.A.K. & Puschmann, H. (2009), J. Appl. Cryst. 42, 339-341.

19. Sheldrick, G.M. (2015). Acta Cryst. A71, 3-8.

20. Sheldrick, G.M. (2008). Acta Cryst. A64, 112-122.

CHAPTER 4. CONCLUSIONS AND FUTURE DIRECTIONS

4.1 Conclusions

This thesis set out to answer questions about the impact redox-active ligands have on the reactivity of high-valent oxorhenium and oxovanadium complexes. Cyclic voltammetry experiments, solid state data, and computational work confirms the formulation of $[Re(O)_2(ap)(isq)]$, which is one oxidation state above Re(VII), as a true S=1/2 species. The work presented on $[Re(O)_2(ap)(isq)]$ in Chapter 2, successfully demonstrated that the kinetic impact of unpaired spin on ancillary ligands changes reactivity at a terminal oxo ligand. Though oxidation of $[Re(O)_2(ap)_2]^-$ to $[Re(O)_2(ap)(isq)]$ was shown to impart no thermodynamic advantage based on solid-state data suggesting a strengthening of the Re–O bond, only $[Re(O)_2(ap)(isq)]$ was capable of transferring an O atom to trityl radical. The non-zero spin density on the terminal oxo ligands suggests that symmetry allowed mixing does occur and this offers an advantage to bond-making reactivity at the oxo. This has implications for the use of redox-active ligands to allow both 1e– and 2e– bond-making reactivity. It showed that ligand oxidation state can be used to selectively control the type of reactivity that occurs at the terminal oxo ligand. This has specific relevance for mimics of biologic systems, like the OEC of PSII, that are thought to undergo a radical process for O–O bond making. Redox-active ligands allowed us to successfully create a “masked” oxyl that was both stable enough for characterization and showed reactivity unique from its closed-shell counterpart.

Our attempts to transfer this “masked” oxyl design to vanadium offered mixed results but did open up opportunities for other reactivity. The redox-active NHC ligand allowed for the facile synthesis of a vanadium(V) oxo complex that has the ability to be oxidized further, which mimics the rhenium chemistry. The effect of the redox-active NHC ligand on reactivity at the terminal oxo of VO(OCO)Cl is somewhat less clear, though. Ligand oxidation does appear to play a role in the reaction of VO(OCO)OMe with oxygen as a superoxo complex can only be formed with concomitant ligand oxidation. The evidence of dimer formation in the absence of air from the various alkoxide complexes suggests both C–H and C–O bond breaking activity similar to other oxovanadium complexes and reminiscent of DODH reactions. This reactivity could occur via 1e– or 2e– pathways and it is currently unclear which is operative in this system. The need for base suggests a 2e– mechanism for the reactivity with alkoxide and literature precedence suggests a V(V/III) cycle for aerobic alcohol oxidation but if this occurs via step-wise electron transfer in our complex is unknown. These remaining questions open the possibility for study of 1e– versus 2e– control by ligand oxidation states.

4.2 Future directions

4.2.1 Continuing vanadium studies

In addition to the mechanistic studies proposed in Chapter 3, the oxovanadium chemistry offers multiple areas of additional study. We proposed that the redox-active NHC ligand could mediate reactivity at the terminal oxo of VO(OCO)X, but it is still unclear if this occurs and how it affects reactivity. We expect upon ligand oxidation that a “masked” oxyl complex would form mirroring reactivity seen in Chapter 2 with rhenium. It is suggested that VO(OCO)OMe should be used for follow-up reactivity with regards to OAT to both PPh_3 and trityl radical as well as HAT reactivity with either DHA or CHD, like that for the rhenium. The cyclic voltammograms also indicated a reduced V(IV) complex is achievable. How this reduced species reacts, particularly with regards to HAT or other single electron processes might be an interesting area of study. Along with these fundamental studies, the reactivity of VO(OCO)OMe with model lignin substrates needs to be considered.

The reactivity with O_2 to from the putative superoxo complex still warrants investigation and the redox-active ligand is important for that. Confirmation of an S=1 complex through Evans method NMR or EPR would be a good first step. Creation of a superoxo complex using air opens the possibility for catalytic O-atom transfer reactions. A vanadium superoxo complex could also be studied for biomimetic vanadium dependent haloperoxidase activity(V-HPO). V-HPOs are a class of metalloenzyme that contain an oxo-peroxo-vanadium active site and convert halide ions (X-) into hypohalites (-OX) with the aid of hydrogen peroxide. A hypohalite is the chemical equivalent to an electrophilic (X+) that can then be used as an oxidizing agent for organic substrates.[1,2]

4.2.2 MOFs for catalyst solid support

A clear drawback of both the rhenium and vanadium systems is the propensity towards dimerization. It has been shown previously the mono-oxo Re(V) analogue of $[Re(O)_2(ap)(isq)]$ cannot be isolated due to rapid dimerization upon oxidation from $[Re(O)(ap)_2]^-$ to $[Re(O)(ap)(isq)]$ to form the bis-μ-oxo dimer $[Re_2(\mu\text{-}O)_2(ap)_2(isq)_2]$.

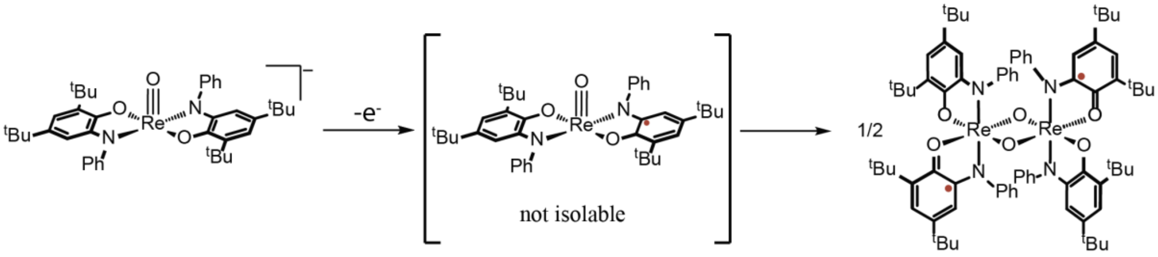

Scheme 4-4. Dimerization of [Re^{V}O(ap)(isq)]

One possible solution to the problem of dimerization is to anchor the complexes on a solid support. Over the past 10 years metal organic frameworks (MOF) have become attractive scaffolds for supported single site catalysts. This is due partly to the development of post-synthetic modifications which allow either the organic linkers or the metal of the nodes to be exchanged while retaining crystallinity.[3,4] The UiO family of MOFs are particularly useful in this regard as they are well studied and robust. These MOFs contain nodes of $Zr_6O_4(OH)_4$ and organic linkers generally containing 1,4-benzenedicarboxylates with either phenyl, biphenyl, or terphenyl links for UiO-66, UiO-67, and UiO-68 respectively.[5,6] Due to varying pore sizes among these MOFs, UiO-68 would be the best choice for modification and eventual incorporation of a metal catalyst. Figure 1 represents post synthetic exchange of UiO-68 to incorporate a catechol moiety into the organic linker.

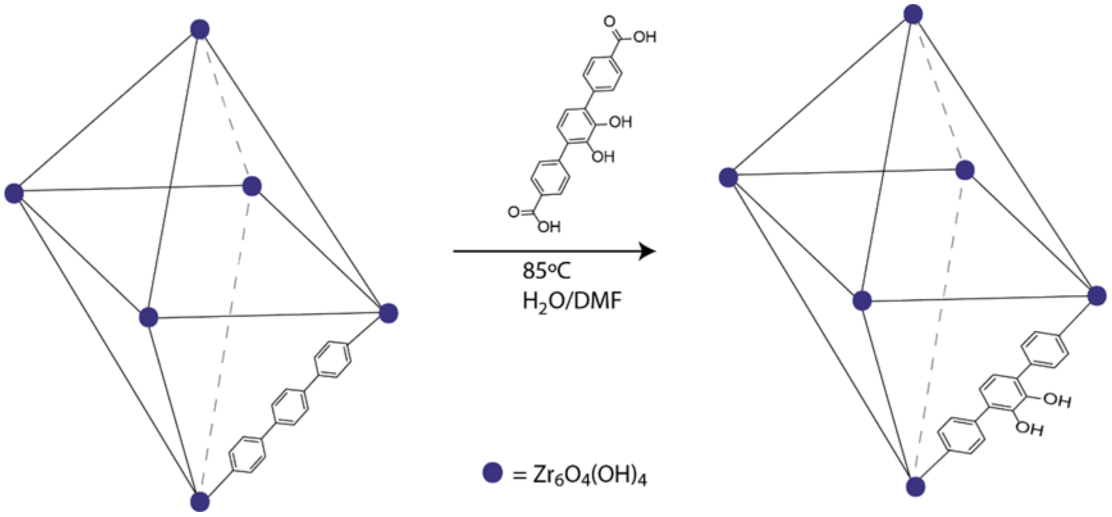

Figure 4-1. Post-synthetic exchange of catechol linker

Incorporation of a rhenium(V) metal center into the modified MOF and possible oxidation is shown in Figure 3. This modification would make either 1e– oxidation to the semiquinone (a, Figure 3) or 2e– oxidation to the dioxo complex (b, Figure 3) possible. These modifications can then be studied for C–O bond forming reactions or other oxidations with the hope we avoid dimer formation and allow for reoxidation of the complex using air thereby making it catalytic and environmentally friendly. The single electron oxidation potential can be used for PCET in MOFs which has applications for energy conversion and storage via processes like artificial photosynthesis. Similar work has been done from the Morris lab, including electrochemical water oxidation by taking advantage of the proton acceptor abilities of the metal nodes and electron transfer through modified organic linkers.[7-9]

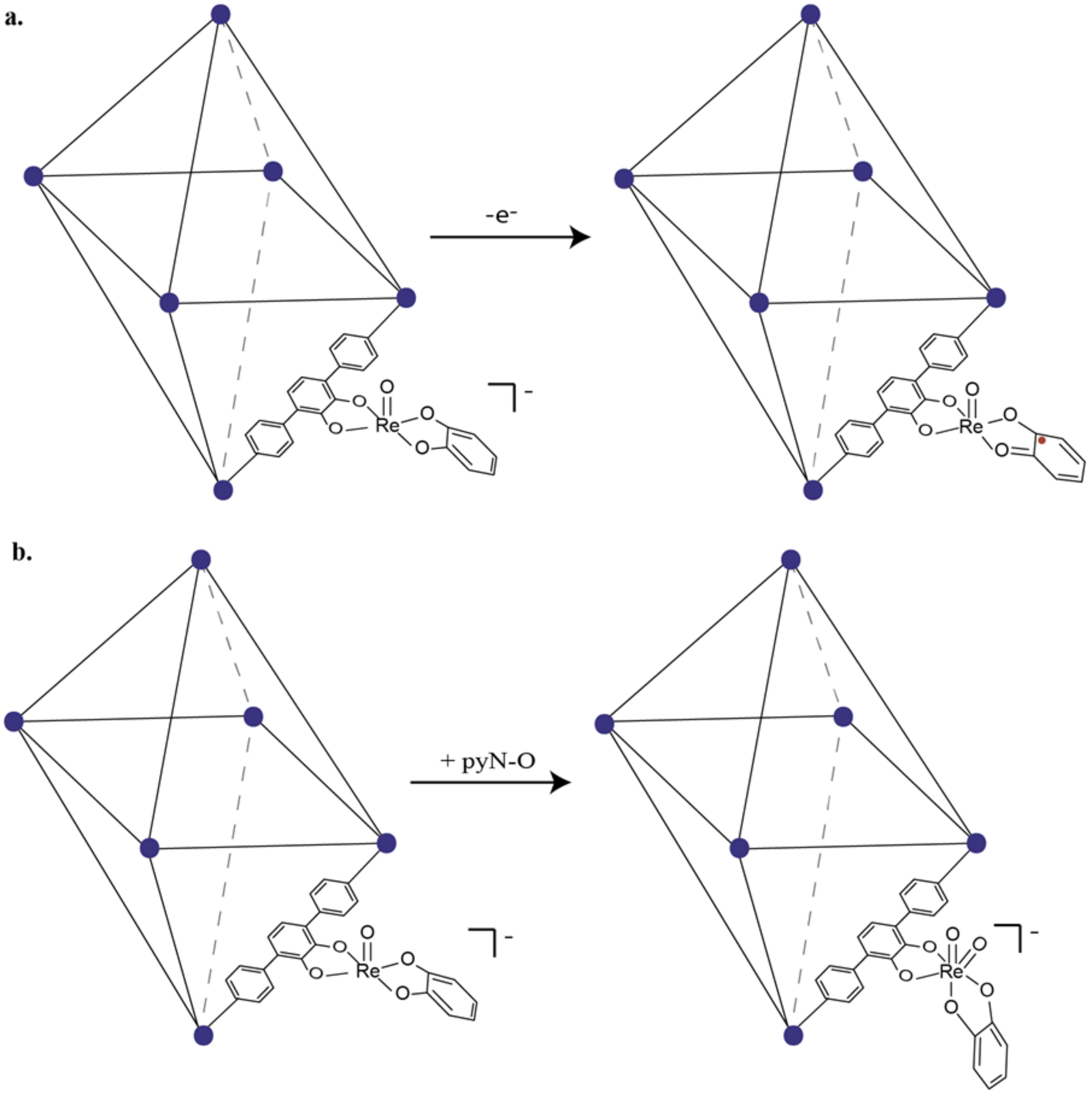

Figure 4-2. Options for oxidation of [Re^{V}(cat)] incorporated into MOF

Overall, the possibilities with the rhenium and vanadium chemistry have the opportunity to provide insight into solutions for modern day chemical challenges.

4.3 References

1. Waidmann, C. R.; DiPasquale, A. G.; Mayer, J. M., Synthesis and Reactivity of Oxo-Peroxo-Vanadium(V) Bipyridine Compounds. Inorganic Chemistry 2010, 49 (5), 2383-2391.

2. Winter, J. M.; Moore, B. S., Exploring the Chemistry and Biology of Vanadium-dependent Haloperoxidases. J Biol Chem 2009, 284 (28), 18577-18581.

3. Kalaj, M.; Cohen, S. M., Postsynthetic Modification: An Enabling Technology for the Advancement of Metal–Organic Frameworks. ACS Cent. Sci. 2020, 6 (7), 1046-1057.

4. Tanabe, K. K.; Cohen, S. M., Postsynthetic modification of metal–organic frameworks—a progress report. Chem. Soc. Rev. 2011, 40 (2), 498-519.

5. Kandiah, M.; Usseglio, S.; Svelle, S.; Olsbye, U.; Lillerud, K. P.; Tilset, M., Post-synthetic modification of the metal–organic framework compound UiO-66. J. Mater. Chem. 2010, 20 (44), 9848.

6. Cavka, J. H.; Jakobsen, S.; Olsbye, U.; Guillou, N.; Lamberti, C.; Bordiga, S.; Lillerud, K. P., A New Zirconium Inorganic Building Brick Forming Metal Organic Frameworks with Exceptional Stability. Journal of the American Chemical Society 2008, 130 (42), 13850-13851.

7. Celis-Salazar, P. J.; Epley, C. C.; Ahrenholtz, S. R.; Maza, W. A.; Usov, P. M.; Morris, A. J., Proton-Coupled Electron Transport in Anthraquinone-Based Zirconium Metal–Organic Frameworks. Inorganic Chemistry 2017, 56 (22), 13741-13747.

8. Lin, S.; Usov, P. M.; Morris, A. J., The role of redox hopping in metal–organic framework electrocatalysis. Chemical Communications 2018, 54 (51), 6965-6974.

9. Usov, P. M.; Ahrenholtz, S. R.; Maza, W. A.; Stratakes, B.; Epley, C. C.; Kessinger, M. C.; Zhu, J.; Morris, A. J., Cooperative electrochemical water oxidation by Zr nodes and Ni–porphyrin linkers of a PCN-224 MOF thin film. Journal of Materials Chemistry A 2016, 4 (43), 16818-16823.